

RADIATION DAMAGE STUDIES OF BULK METALLIC GLASS MATERIALS
UNDER PROTON IRRADIATION AND RADIOPROTECTION STUDIES FOR
METU-DBL

A THESIS SUBMITTED TO
THE GRADUATE SCHOOL OF NATURAL AND APPLIED SCIENCES
OF
MIDDLE EAST TECHNICAL UNIVERSITY

BY

PELİN USLU

IN PARTIAL FULFILLMENT OF THE REQUIREMENTS
FOR
THE DEGREE OF MASTER OF SCIENCE
IN
METALLURGICAL AND MATERIALS ENGINEERING

JUNE 2019

Approval of the thesis:

**RADIATION DAMAGE STUDIES OF BULK METALLIC GLASS
MATERIALS UNDER PROTON IRRADIATION AND RADIOPROTECTION
STUDIES FOR METU-DBL**

submitted by **PELİN USLU** in partial fulfillment of the requirements for the degree
of **Master of Science in Metallurgical and Materials Engineering Department,**
Middle East Technical University by,

Prof. Dr. Halil Kalıpçılar
Dean, Graduate School of Natural and Applied Sciences _____

Prof. Dr. C. Hakan Gür
Head of Department, **Metallurgical and Materials Engineering** _____

Prof. Dr. M. Vedat Akdeniz
Supervisor, **Metallurgical and Materials Engineering, METU** _____

Prof. Dr. M. Bilge Demirköz
Co-supervisor, **Physics Department, METU** _____

Examining Committee Members:

Prof. Dr. M. Tevfik Zeyrek
Physics Department, METU _____

Prof. Dr. M. Vedat Akdeniz
Metallurgical and Materials Eng. Dept., METU _____

Prof. Dr. M. Bilge Demirköz
Physics Department, METU _____

Prof. Dr. Amdulla O. Mekhrabov
Metallurgical and Materials Eng. Dept., METU _____

Prof. Dr. Şükrü Talaş
Metallurgical and Materials Eng. Dept., AKU _____

Date:

I hereby declare that all information in this document has been obtained and presented in accordance with academic rules and ethical conduct. I also declare that, as required by these rules and conduct, I have fully cited and referenced all material and results that are not original to this work.

Name, Surname: Pelin Uslu

Signature :

ABSTRACT

RADIATION DAMAGE STUDIES OF BULK METALLIC GLASS MATERIALS UNDER PROTON IRRADIATION AND RADIOPROTECTION STUDIES FOR METU-DBL

Uslu, Pelin

M.S., Department of Metallurgical and Materials Engineering

Supervisor : Prof. Dr. M. Vedat Akdeniz

Co-Supervisor : Prof. Dr. M. Bilge Demirköz

June 2019, 151 pages

Suitable material selection is critical for the sustainability of missions in radiation environments. Radiation tests are required for candidate materials before being used in these environments. While neutron and heavy ion tests are often performed on materials intended for the nuclear reactors, proton tests are necessary for space applications due to them being the dominant radiation. Generally, crystalline materials are used in radiation environments but, new material search is ongoing. One of such new generation is bulk metallic glasses (BMGs). They have received much attention due to their superior physical, chemical, mechanical and magnetic properties compared to their crystalline counterparts. Especially, new generations of Fe-based BMGs have great potential for these environments due to high strength and hardness as well as good corrosion resistance. Mostly neutron and heavy ions tests exist in literature. Here, proton tests for these materials were performed and the effects of proton irradiation on Fe-based BMGs for space radiation were studied. Fe-based BMG was produced by arc melting and then suction casting into copper mold in the form of a 10 cm long cylindrical rod with a diameter of 3 mm. In addition, com-

mercially available 304 and 316 SS were tested with 30 MeV protons. Structural, thermal, mechanical and magnetic characterization techniques were employed to examine the effects of proton radiation on these materials. These tests which are the first time such a study has been performed in Turkey, were conducted at the new METU-Defocusing BeamLine (DBL) facility located inside the Turkish Atomic Energy Authority (TAEA) SANAEM Proton Accelerator Facility (PAF). This facility uses 15-30 MeV protons with a flux between $10^5 - 10^{11}$ p/cm²/s to test electronics. Also, studies for radioisotope production and radiation protection of sensitive electronic devices of METU-DBL are also presented here. Characterization studies of irradiated materials showed that the point defects were formed on the both BMGs and stainless steels after the irradiation. Any surface damage or new phase occurrence were not observed on these samples. After the irradiation, point defects were observed on the samples.

Keywords: Bulk metallic glasses, effects of radiation, 30 MeV protons, space radiation

ÖZ

İRİ HACİMLİ METALİK CAM MALZEMELERİN PROTON IŞINLAMASI ALTINDAKİ RADYASYON HASARLARI VE ODTÜ-SDH İÇİN RADYASYONDAN KORUNMA ÇALIŞMALARI

Uslu, Pelin

Yüksek Lisans, Metalurji ve Malzeme Mühendisliği Bölümü

Tez Yöneticisi : Prof. Dr. M. Vedat Akdeniz

Ortak Tez Yöneticisi : Prof. Dr. M. Bilge Demirköz

Haziran 2019 , 151 sayfa

Radyasyon çevreleri için uygun malzeme seçimi görevlerin sürdürülebilirliği için kritiktir. Aday malzemeler için radyasyon testlerinin bu çevrelerde kullanılmadan önce yapılması gereklidir. Nükleer reaktörler için sıklıkla nötron ve ağır iyon testleri yapılırken, uzay uygulamalarında baskın radyasyon türü olduğu için proton testleri gereklidir. Radyasyon çevrelerinde genellikle kristal malzemeler kullanılmakta ancak yeni malzeme arayışı sürmektedir. Yeni jenerasyon malzemelerden biri de iri hacimli metalik camlardır. Bu malzemeler üstün fiziksel, kimyasal, mekanik ve manyetik özelliklerinden dolayı kristal benzerlerine göre oldukça ilgi çekmiştir. Özellikle demir bazlı metalik camlar, yüksek dayanım, sertlik ve iyi korozyon dayanımlarından dolayı bu çevreler için yüksek potansiyele sahiptirler. Literatürde çoğunlukla bu malzemeler için nötron ve ağır iyon testleri bulunmaktadır. Bu çalışmada demir bazlı iri hacimli metalik camlar için proton testleri yapıldı ve proton radyasyonunun bu malzemeler üzerindeki etkileri çalışıldı. Bu malzemeler ark eritme ve bakır kalıp dökmede silindir formunda üretilmiştir ve 3 mm çapında yaklaşık 10 mm uzunluğundadırlar. Ek

olarak, paslanmaz elik 304 ve 316'da ticari olarak saėlanmıř ve 30 MeV protonlarla test edilmiřtir. Radyasyonun malzemeler zerindeki etkilerini inceleyebilmek iin, yapısal, termal, mekanik ve manyetik karakterizasyon teknikleri uygulanmıřtır. Trkiye'de ilk kez yapılan bu testler, Trkiye Atom Enerjisi Kurumu (TAEK) SANAEM Proton Hızlandırıcı Tesisi'nde (PHT) kurulan ODT- Saılmalı Demet Hattı'nda (SDH) yrtlmřtir. Bu tesis, 15-30 MeV enerjiye sahip ve $10^5 - 10^{11}$ p/cm²/s akı aralıėındaki protonları kullanarak elektronikleri test etmektedir. Ayrıca, radyoizotop retimi ve ODT-SDH'nin hassas elektronik bileřenleri iin radyasyondan koruma alıřmaları burada sunulmuřtur. Iřınlanan malzemeler iin yapılan karakterizasyon alıřmalarında, hem iri hacimli metalik camlarda hem de paslanmaz eliklerde noktasal kusurların oluřtuėu grlmektedir. Numunelerde herhangi bir yzey hasarı veya yeni bir faz oluřumu gzlenmedi. Iřınlamadan sonra numunelerde noktasal kusurlar gzlemlendi.

Anahtar Kelimeler: İri hacimli metalik camlar, radyasyonun etkileri, 30 MeV protonlar,uzay radyasyonu

To my lovely family ...

ACKNOWLEDGMENTS

I would like to express my gratitude to my supervisor Prof. Dr. M. Vedat Akdeniz and my co-supervisor Prof. Dr. M. Bilge Demirköz for their support, guidance and encouragement during this independent research.

I would like to thank Dr. Selcen Uzun Duran, Selen Akçelik, Besna Bülbül and colleagues working for METU-DBL project for their help and support in my studies.

I am thankful to Iraz Begüm Demir, Orkun Elçin and Muammer Demiralp for their support and friendship.

My deep gratitude to my beloved family; my mother Semra Uslu, my father Kenan Uslu and my brother Mert Uslu for their support, patience, guidance and unconditional love and for shedding light on my way. Their support and encouragement were worth more than I can express on paper.

I am very grateful to my love, Eren Can Kışeci, for his support, understanding, patience and unconditional love.

I am thankful to Presidency of Defence Industries for financial support and also Turkish Atomic Energy Authority (TAEA) Proton Accelerator Facility (PAF) and CERN for their collaboration.

I would like to express my thanks Prof. Dr. Uğur Yahşi from Marmara University for his support in PALS analysis.

I would also like to thank Scientific and Technological Research Council of Turkey for financial support (2210-C) during my thesis studies.

Finally, I would like to thank ROKETSAN for providing material support to produce bulk metallic glass.

TABLE OF CONTENTS

ABSTRACT	v
ÖZ	vii
ACKNOWLEDGMENTS	x
TABLE OF CONTENTS	xi
LIST OF TABLES	xv
LIST OF FIGURES	xix
LIST OF ABBREVIATIONS	xxvii

CHAPTERS

1	INTRODUCTION	1
2	SPACE RADIATION, RADIATION EFFECTS ON MATERIALS AND BULK METALLIC GLASSES	5
2.1	Space Radiation Environment	5
2.1.1	Earth Orbit	5
2.1.2	Effects of Space Radiation on Electronic Components in Earth Orbit	7
2.1.3	Types of Space Radiation Environment	8
2.1.3.1	Trapped radiation	8
2.1.3.2	Galactic cosmic rays	9
2.1.3.3	Solar particle events	10

2.2	Radiation Effects on Materials	10
2.2.1	Particle Types and Their Ranges in Materials	12
2.2.2	Radiation Damage Mechanisms	16
2.2.2.1	Total Ionizing Dose (TID)	17
2.2.2.2	Displacement Damage (DD)	17
2.2.2.3	Single Event Effects (SEE)	19
2.3	METU-DBL Project	21
2.4	Materials Under Irradiation	27
2.5	Bulk Metallic Glasses	28
2.5.1	Mechanical Properties of BMGs	29
2.5.2	Magnetic Properties of BMGs	32
2.6	Fe-based BMGs	32
2.7	Bulk Metallic Glasses Under Irradiation	33
3	RADIATION TESTS OF STAINLESS STEEL AND BULK METAL- LIC GLASS SAMPLES WITH PROTONS AND CHARACTERI- ZATION RESULTS	43
3.1	Raw Materials	43
3.2	Production of BMGs	44
3.3	Radiation Testing of Materials	46
3.4	Characterization Techniques	47
3.4.1	X-ray Diffractometer	48
3.4.2	Optic Microscope	48
3.4.3	Scanning Electron Microscope	48
3.4.4	Differential Scanning Calorimetry	48

3.4.5	Vibrating Sample Magnetometry	49
3.4.6	Microhardness Test	50
3.4.7	Positron Annihilation Lifetime Spectroscopy	51
3.4.8	Stopping and Range of Ions In Matter (SRIM) Simulations	51
3.5	SRIM Simulations of Irradiated Materials	52
3.6	Effects of irradiation on the microstructure and properties of the materials	57
3.6.1	Effects of irradiation on 304 and 316 Stainless Steels	57
3.6.2	Effects of irradiation on $M_{60}Cr_{13}Mo_{10}B_8Y_2Mn_7$	68
3.6.3	Effects of irradiation on $Fe_{36}Co_{36}B_{19.2}Si_{4.8}Nb_4$ Bulk Metallic Glass	74
4	SHIELDING DESIGNS FOR METU-DBL AND RADIATION PROTECTION	87
4.1	Shielding Studies for Electronic Components and Beam Elements of METU-DBL	88
4.1.1	Shielding Studies for METU-DBL Collimators	92
4.1.2	Shielding Studies for Electronic Components in the METU-DBL Subsystems	96
4.1.2.1	Shielding Studies for Electronic Components of Test and Measurement System	96
4.2	Radioprotection Studies	112
4.2.1	Radioisotope Studies	113
4.2.2	Cooling Time Studies for Activated Elements of METU-DBL	125
4.2.2.1	Cooling Time For the First Protective Collimator	125

4.2.2.2	Dose in the TAEA PHT R&D room . . .	127
4.2.2.3	Cooling Time Studies for the Beam Dump	129
5	CONCLUSION	131
	REFERENCES	133
APPENDICES		
A	143
A.1	SEM MICROGRAPHS	143
A.2	LINE MAPPING	144
A.3	EDS RESULTS	146

LIST OF TABLES

TABLES

Table 2.1	Earth orbit altitude ranges and approximate received doses for different Earth orbit types [6].	6
Table 2.2	Types of Single Event Effects and the resulting errors [39].	20
Table 2.3	The historical development of the Fe-based bulk metallic glasses [69].	33
Table 2.4	Positron lifetime of ZrCuAl bulk metallic glass before and after irradiation using 15 keV positrons for positron annihilation spectroscopy [87].	41
Table 3.1	The chemical composition of scrap cast iron with weight percentages.	44
Table 3.2	The alloying elements with their purity grades.	44
Table 3.3	Samples and their fluences in accordance with their different exposures.	47
Table 3.4	Chemical compositions of 304 and 316 SS 304 [94] [95].	52
Table 3.5	Nuclear and electronic energy losses of 30 MeV protons in different materials.	53
Table 3.6	Threshold displacement energies of elements contained in alloys [98].	56
Table 3.7	The analysis of positron annihilation lifetime spectroscopy.	61
Table 3.8	Average hardness for 304 and 316 SS using recorded points from the as-received and as-irradiated samples.	66

Table 3.9 Average hardness using ten points from the as-cast and as-irradiated samples.	73
Table 3.10 The analysis of positron annihilation lifetime spectroscopy.	78
Table 3.11 Phase transformation temperatures of as-cast and after receiving a fluence of 1.3×10^{13} p/cm ² samples.	81
Table 3.12 Phase transformation temperatures for as-cast and after receiving a fluence of 1.3×10^{13} p/cm ² samples.	82
Table 3.13 Saturation magnetization and coercivity of Fe ₃₆ Co ₃₆ B _{19.2} Si _{4.8} Nb ₄ samples.	83
Table 3.14 Average hardness values of the samples before and after irradiation.	85
Table 4.1 The chemical composition of Aluminum alloy 6082 [104].	89
Table 4.2 The possible radiation scenarios of METU-DBL.	91
Table 4.3 Comparative results of shielding studies for different shielding options of the adjustable conic collimator.	95
Table 4.4 Comparative results of shielding studies for the readout electronics of the pixel and diamond detectors.	98
Table 4.5 Shielding studies for the electronic readout components of fiber scintillators.	100
Table 4.6 Shielding studies for the step motor.	102
Table 4.7 Shielding studies for the mobile radiation robot monitor.	103
Table 4.8 Shielding studies for the electronic components of the cooling sub-system.	105
Table 4.9 Shielding studies for the electronic components in the vacuum sub-system.	108

Table 4.10 Shielding studies for the electronic components in the control sub-system.	111
Table 4.11 Radioisotope studies for the lead layer behind the aluminum with a thickness of 0.25 cm.	114
Table 4.12 Radioisotope studies for the lead layer behind the aluminum with a thickness of 0.50 cm.	114
Table 4.13 Radioisotope studies of Al6082, Al6061, Al7075 and Al7050 considered for the first protective collimator.	115
Table 4.14 Radioisotope studies of 304, 316 SS and iron considered for the first protective collimator.	117
Table 4.15 Radioisotope studies of marble considered for the first protective collimator.	119
Table 4.16 Radioisotope studies of bismuth considered for the first protective collimator.	121
Table 4.17 Radioisotope studies of titanium considered for the first protective collimators.	122
Table 4.18 Radioisotope studies of tungsten considered for the first protective collimators.	123
Table 4.19 Radioisotope studies of borosilicate considered for the window of the movable beam screen.	124
Table 4.20 Radioisotope studies of sapphire considered for the window of the movable beam screen.	124
Table 4.21 Cooling time and respective dose rates 1 cm away from the first protective collimator after a 1 hour irradiation with 0.1 μ A are seen.	126
Table 4.22 List of all irradiations performed at METU-DBL during the commissioning and the pretests of METU-DBL are listed.	127

Table 4.23 Time that dose rate drops below $2.5 \mu\text{SV/h}$ in the room when the beam is on according to Scenario A-B-C-D.	128
Table 4.24 Cooling time after an irradiation of 1 hour at $0.1 \mu\text{A}$ for the beam dump.	129
Table 4.25 Radioisotopes that remain on the graphite surface 1 second after one hour irradiation.	130

LIST OF FIGURES

FIGURES

Figure 2.1	Van Allen Radiation Belts around the Earth [16].	9
Figure 2.2	A coronal mass ejection from the Sun dated April 16, 2012 as observed by the SOHO satellite [21].	10
Figure 2.3	The electromagnetic spectrum [25].	11
Figure 2.4	The range of protons, electrons and alphas in aluminum with re- spect to kinetic energy [19].	13
Figure 2.5	Bragg Curve for an alpha particle stopping in air [30].	14
Figure 2.6	The Bethe-Bloch plot shows the interaction of the protons in ma- terial [32].	16
Figure 2.7	Displacement damage in a lattice occurs when an incoming particle displaces a lattice atom in a collision [34].	18
Figure 2.8	Displacement damage in silicon due to proton irradiation [35]. . . .	18
Figure 2.9	Direct and indirect ionization [40].	21
Figure 2.10	Drawing of TAEA's Proton Accelerator Facility [43].	22
Figure 2.11	The images of third magnet and its certificate from CERN.	24
Figure 2.12	A drawing of the METU-DBL [51].	25
Figure 2.13	A bird eye view of METU-DBL [52].	26
Figure 2.14	Comparison of structure of crystalline and amorphous metal [58]. .	28

Figure 2.15 Comparison of amorphous and crystalline materials in terms of strength and elastic limit [59].	29
Figure 2.16 Elastic limit plotted against Young's modulus for 1507 metals, alloys, metal matrix composites and metallic glasses [63].	30
Figure 2.17 Relationship between fracture strength or Vickers hardness and Young modulus for various BMGs [64].	31
Figure 2.18 Schematic illustration of a defect created in a metallic crystal (left) and a metallic glass (right) under MeV electron irradiation [72].	34
Figure 2.19 XRD patterns of FeSiB metallic glass before and after 250 keV H^+ ion irradiation [81].	35
Figure 2.20 SEM images of FeSiB metallic glass before and after the 250 keV H^+ ion irradiation [81].	36
Figure 2.21 XRD patterns of ZrCuFeAl metallic glass before and after 300 keV Ar^+ ion irradiation [82].	37
Figure 2.22 DSC curves of ZrCuFeAl metallic glass before and after the 300 keV Ar^+ ion irradiation [82].	37
Figure 2.23 XRD patterns of $Ni_{62}Ta_{38}$ metallic glass before and after 300 keV He^{+2} ion irradiation [83].	38
Figure 2.24 SEM images of $Ni_{62}Ta_{38}$ metallic glass before and after 300 keV He^{+2} ion irradiation [83].	39
Figure 2.25 XRD patterns of Fe and Ni based metallic glasses before and after H^+ ion irradiation with 40 keV [73].	40
Figure 2.26 Hysterises loops of Fe-based metallic glass before and after H^+ ion irradiation with 40 keV [73].	40
Figure 3.1 Edmund Buhler arc melting apparatus.	45
Figure 3.2 Some examples of the produced and cut samples.	46

Figure 3.3 a) The designed holder for the samples during irradiation. Stainless steels (on left) and bulk metallic glasses (on right) were placed in holder.	
b) The direction of the beam.	46
Figure 3.4 Schematic illustrations of the examined surfaces from the top and side view of all samples.	47
Figure 3.5 Setaram Setsys 16/18 branded differential scanning calorimetry apparatus.	49
Figure 3.6 ADE Magnetics EV/9 vibrating sample magnetometer apparatus.	50
Figure 3.7 The direction of the microhardness analyses is given.	50
Figure 3.8 The positron annihilation lifetime spectroscopy apparatus [92].	51
Figure 3.9 Energy losses of protons in a) 304 stainless steel, b) 316 stainless steel, c) $\text{Fe}_{36}\text{Co}_{36}\text{B}_{19.2}\text{Si}_{4.8}\text{Nb}_4$, d) $\text{M}_{60}\text{Cr}_{13}\text{Mo}_{10}\text{B}_8\text{Y}_2\text{Mn}_7$ versus target depth.	54
Figure 3.10 The vacancy formation of atoms in a) 304 stainless steel, b) 316 stainless steel, c) $\text{Fe}_{36}\text{Co}_{36}\text{B}_{19.2}\text{Si}_{4.8}\text{Nb}_4$, d) $\text{M}_{60}\text{Cr}_{13}\text{Mo}_{10}\text{B}_8\text{Y}_2\text{Mn}_7$ versus target depth.	55
Figure 3.11 SEM images of 304 SS samples from the top view (central part).	57
Figure 3.12 SEM images of 316 SS samples from the top view (central part).	58
Figure 3.13 The regions at which SEM images were taken for the 304 SS (left) and 316 SS (right) samples.	59
Figure 3.14 SEM images of the 304 SS sample from the side view.	59
Figure 3.15 SEM images of the 316 SS sample from the side view.	60
Figure 3.16 Positron annihilation lifetime spectroscopy for the 316 SS sample.	61
Figure 3.17 XRD patterns of 304 SS samples before and after irradiation.	62
Figure 3.18 XRD patterns of 316 SS samples before and after irradiation.	62

Figure 3.19 DSC curves of 304 SS for the as-received sample and a sample which received a fluence of 1.0×10^{13} p/cm ²	64
Figure 3.20 DSC curves of 316 SS for the as-received sample and a sample which received a fluence of 1.0×10^{13} p/cm ²	64
Figure 3.21 Microhardness analysis of the 304 SS samples before and after irradiation (top view).	65
Figure 3.22 Microhardness analysis of the 316 SS samples before and after irradiation (top view).	65
Figure 3.23 Microhardness analysis of 304 SS from the side view.	67
Figure 3.24 Microhardness analysis of 316 SS sample from the side view.	67
Figure 3.25 Optical microscope images of $M_{60}Cr_{13}Mo_{10}B_8Y_2Mn_7$ before the irradiation.	68
Figure 3.26 SEM images of unmelted molybdenum parts of $M_{60}Cr_{13}Mo_{10}B_8Y_2Mn_7$ samples before and after irradiation (top view).	69
Figure 3.27 SEM images of crystalline parts of $M_{60}Cr_{13}Mo_{10}B_8Y_2Mn_7$ samples before and after irradiation (top view).	69
Figure 3.28 SEM images of unmelted molybdenum parts of $M_{60}Cr_{13}Mo_{10}B_8Y_2Mn_7$ sample from side view.	70
Figure 3.29 SEM images of the crystalline part of $M_{60}Cr_{13}Mo_{10}B_8Y_2Mn_7$ sample from side view.	71
Figure 3.30 XRD patterns of the $M_{60}Cr_{13}Mo_{10}B_8Y_2Mn_7$ samples before and after irradiation.	72
Figure 3.31 Microhardness analysis of the $M_{60}Cr_{13}Mo_{10}B_8Y_2Mn_7$ samples before and after the irradiation (top view).	72
Figure 3.32 Microhardness analysis of the $M_{60}Cr_{13}Mo_{10}B_8Y_2Mn_7$ sample from the side view.	73

Figure 3.33 Optical microscope image of $\text{Fe}_{36}\text{Co}_{36}\text{B}_{19.2}\text{Si}_{4.8}\text{Nb}_4$ before the irradiation.	74
Figure 3.34 SEM images of amorphous part of the $\text{Fe}_{36}\text{Co}_{36}\text{B}_{19.2}\text{Si}_{4.8}\text{Nb}_4$ samples before and after the irradiation (top view).	75
Figure 3.35 SEM images of dendrite part in the $\text{Fe}_{36}\text{Co}_{36}\text{B}_{19.2}\text{Si}_{4.8}\text{Nb}_4$ samples before and after the irradiation (top view).	76
Figure 3.36 SEM images of the dendrite part in the $\text{Fe}_{36}\text{Co}_{36}\text{B}_{19.2}\text{Si}_{4.8}\text{Nb}_4$ samples before and after the irradiation (top view).	76
Figure 3.37 The SEM images of the highest fluence $\text{Fe}_{36}\text{Co}_{36}\text{B}_{19.2}\text{Si}_{4.8}\text{Nb}_4$ sample from side view.	77
Figure 3.38 Positron annihilation lifetime spectroscopy for $\text{Fe}_{36}\text{Co}_{36}\text{B}_{19.2}\text{Si}_{4.8}\text{Nb}_4$ samples.	78
Figure 3.39 XRD patterns of $\text{Fe}_{36}\text{Co}_{36}\text{B}_{19.2}\text{Si}_{4.8}\text{Nb}_4$ samples before and after the irradiation.	79
Figure 3.40 DSC curves of the $\text{Fe}_{36}\text{Co}_{36}\text{B}_{19.2}\text{Si}_{4.8}\text{Nb}_4$ for as-cast and the sample which received a highest fluence which is 1.3×10^{13} p/cm ² (First Heating Paths).	80
Figure 3.41 DSC curves of the $\text{Fe}_{36}\text{Co}_{36}\text{B}_{19.2}\text{Si}_{4.8}\text{Nb}_4$ for as-cast and the sample which received a highest fluence which is 1.3×10^{13} p/cm ² (Second Heating Paths).	80
Figure 3.42 DSC curves of the $\text{Fe}_{36}\text{Co}_{36}\text{B}_{19.2}\text{Si}_{4.8}\text{Nb}_4$ for as-cast and the sample which received a highest fluence which is 1.3×10^{13} p/cm ² (First Cooling Paths).	81
Figure 3.43 DSC curves of the $\text{Fe}_{36}\text{Co}_{36}\text{B}_{19.2}\text{Si}_{4.8}\text{Nb}_4$ for as-cast and the sample which received a highest fluence which is 1.3×10^{13} p/cm ² (Second Cooling Paths).	82

Figure 3.44 VSM analysis of $\text{Fe}_{36}\text{Co}_{36}\text{B}_{19.2}\text{Si}_{4.8}\text{Nb}_4$ samples before and after irradiation.	83
Figure 3.45 EDS mapping analysis for the $\text{Fe}_{36}\text{Co}_{36}\text{B}_{19.2}\text{Si}_{4.8}\text{Nb}_4$ sample at a received fluence of 1.3×10^{13} p/cm ²	84
Figure 3.46 Microhardness analysis of the $\text{Fe}_{36}\text{Co}_{36}\text{B}_{19.2}\text{Si}_{4.8}\text{Nb}_4$ samples before and after the irradiation (top view).	85
Figure 3.47 Microhardness analysis of the $\text{Fe}_{36}\text{Co}_{36}\text{B}_{19.2}\text{Si}_{4.8}\text{Nb}_4$ sample (side view).	86
Figure 4.1 A model of the R&D room in the FLAIR, the visual interface of FLUKA includes TAEA PAF beamline elements as well as the 5 port magnet and METU-DBL.	90
Figure 4.2 The first protective collimator of METU-DBL without shielding.	93
Figure 4.3 The shielding of the first collimator from two different angles.	93
Figure 4.4 The first protective collimator assembled into the METU-DBL pretest beam line.	94
Figure 4.5 The technical drawing of the adjustable conical collimator.	96
Figure 4.6 Technical Design of the test table in target area for the pretests.	97
Figure 4.7 Unshielded (left) and shielded (right) pixel detector electronics.	99
Figure 4.8 Unshielded (left) and shielded (right) diamond detector.	99
Figure 4.9 Unshielded (left) and shielded (right) lower fiber scintillator readout.	101
Figure 4.10 Unshielded (left) and shielded (right) readout of the pixel detector.	102
Figure 4.11 The unshielded (left) and shielded (right) step motor.	103
Figure 4.12 The position of the cooling subsystem is shown in FLAIR, the visual interface of FLUKA.	104

Figure 4.13 Unshielded (above) and shielded (below) cooling subsystem.	106
Figure 4.14 Unshielded (left) and shielded (right) Programmable Logical Controller.	107
Figure 4.15 The position of the turbomolecular pump in the vacuum subsystem is shown in FLAIR, the visual interface of FLUKA.	108
Figure 4.16 The turbomolecular pump (upper panel), connected to the beam pipe with a 1.5 m long and 100 mm wide flex pipe during pretests, and with its shield during the final assembly of METU-DBL (lower panel). . .	109
Figure 4.17 The shielding of the second turbomolecular pump from two different angles.	110
Figure 4.18 Position of the electronic components of the control subsystem in FLAIR, the visual interface of FLUKA is shown.	111
Figure 4.19 Two images from the front (upper panel) and one image from the back (lower panel) of the electronics box of control subsystem are shown [108].	112
Figure 4.20 The place of ICRU sphere in FLUKA.	126
Figure 4.21 The location of an ICRU sphere in FLUKA.	128
Figure A.1 Penetration depth of 30 MeV protons inside the $\text{Fe}_{36}\text{Co}_{36}\text{B}_{19.2}\text{Si}_{4.8}\text{Nb}_4$ sample.	143
Figure A.2 Line mapping of horizontally embedded 304 SS sample.	144
Figure A.3 Line mapping of horizontally embedded 316 SS sample.	144
Figure A.4 Line mapping of horizontally embedded $\text{Fe}_{36}\text{Co}_{36}\text{B}_{19.2}\text{Si}_{4.8}\text{Nb}_4$ sample.	145
Figure A.5 Line mapping of horizontally embedded $\text{M}_{60}\text{Cr}_{13}\text{Mo}_{10}\text{B}_8\text{Y}_2\text{Mn}_7$ sample.	145

Figure A.6 EDS results of the highest fluence 304 SS sample from point 3 which is unirradiated part.	146
Figure A.7 EDS results of the highest fluence 304 SS sample from point 1 which is irradiated part.	147
Figure A.8 EDS results of the highest fluence 304 SS sample from point 2 which is irradiated part.	148
Figure A.9 EDS results of the highest fluence 316 SS sample from point 3 which is unirradiated part.	149
Figure A.10 EDS results of the highest fluence 316 SS sample from point 1 which is irradiated part.	150
Figure A.11 EDS results of the highest fluence 316 SS sample from point 2 which is irradiated part.	151

LIST OF ABBREVIATIONS

METU-DBL	Middle East Technical University - Defocusing Beam Line
TAEA	Turkish Atomic Energy Authority
PAF	Proton Accelerator Facility
BMG	Bulk Metallic Glass
SS	Stainless Steel
LEO	Low Earth Orbit
MEO	Medium Earth Orbit
GEO	Geostationary Earth Orbit
ISS	International Space Station
GNSS	Global Navigation Satellite Systems
SAA	South Atlantic Anomaly
SEE	Single Event Effect
TID	Total Ionizing Dose
DD	Displacement Damage
NIEL	Non-Ionizing Energy Loss
LET	Linear Energy Transfer
SEM	Scanning Electron Microscope
DSC	Differential Scanning Calorimetry
XRD	X-Ray Diffractometer
VSM	Vibrating Sample Magnetometer
PALS	Positron Annihilation Lifetime Spectrometer
GFA	Glass Forming Ability
PLC	Programmable Logical Controller
E_R	Earth Radii

CHAPTER 1

INTRODUCTION

The radiation damage on materials and electronic components is an essential research area to choose proper materials and components for radiation environments. These materials and components should maintain their desired properties during their envisioned mission time and so radiation damage tests are required before use in radiation environments.

In this thesis, the effects of radiation on some materials for space radiation environment were studied. 30 MeV protons were used as a radiation source supplied by the newly constructed METU Defocusing Beam Line. METU-DBL project started off in August 2015 at the Middle East Technical University (METU) Department of Physics. This project, funded by Strategy and Budget Presidency of Turkey, is a part of a larger project, the Earth Observation Satellites Development Project, called IMECE [1]. As it is understood from the Turkish meaning of the word, different institutions and organizations such as Scientific and Technological Research Council of Turkey (TUBITAK), Space Technologies Research Institute as well as Marmara Research Center (MAM), Gazi University and METU are working together for the development of IMECE subsystems. The goal of the IMECE satellite is to develop home-grown subsystems for our national satellites by domestic human resources with the experience gained from BILSAT, RASAT and GÖKTÜRK-2 already in space [2]. In the scope of the IMECE satellite project, METU-DBL will perform radiation tests of sensitive electronic components and materials. A dedicated beam line is being assembled to carry out radiation tests of these electronic components and also materials intended for use in the space environment. METU-DBL has five subsystems; test and

measurement, control, robotic, cooling and vacuum, all of which have many electronic components. These components were shielded by using FLUKA simulation program to protect them against radiation damage and for the long-term durability of the METU-DBL. METU-DBL project will be detailed in Section 2.3.

New and interesting materials that find use in high radiation environments are also studied in this facility. Bulk metallic glasses (BMGs) are a new generation of materials which are used in many applications such as medical, defense and sporting goods due to their superior properties such as high strength and excellent corrosion resistance. Furthermore, they are a group of promising materials for high radiation environments like nuclear reactors and space environment due to their amorphous structure. BMGs do not have grain boundaries and therefore, they do not possess crystal defects like dislocation [3]. Therefore, they are good candidates for use in radiation environments. While ion and neutron irradiation tests are essential for use in nuclear reactors, proton tests are required for demonstrating usability in the space environment. In literature, radiation tests of BMGs were studied mostly for nuclear reactors and there is only limited research with proton irradiations. Therefore, radiation damage studies of BMGs under proton irradiation were performed to study its possible adoption in space.

In this study, Fe-based BMGs were produced in the METU Department of Metallurgical and Materials Engineering using arc melting and copper mold suction casting. The radiation tests of BMGs were carried out with METU-DBL and tests were conducted with a selection of these samples while control samples were left to be examined without irradiation. Furthermore, commercial samples of 304 and 316 SS were also irradiated to compare the effects of radiation on BMGs and crystalline steels. All irradiations were performed up to three different fluences. In another study, the behavior of irradiated materials was examined using scanning electron microscope (SEM), X-ray diffractometer (XRD), differential scanning calorimetry (DSC) analyses, vibrating sample magnetometer (VSM), positron annihilation lifetime spectroscopy (PALS) and microhardness analysis.

In this thesis, space radiation environment and radiation effects on materials are presented in Section 2.1 and Section 2.2. In Section 2.3, METU-DBL is described in detail. Materials under irradiation are given in Section 2.4. The properties of the BMGs and Fe-based BMGs are provided in Section 2.5 and Section 2.6 respectively. In Section 2.7, BMGs under irradiation are presented. In Chapter 3, radiation tests of SSs and BMGs with protons and their characterization results are given. In Chapter 4, FLUKA simulations of radiation protection and shielding designs as well as radioisotope activation studies for METU-DBL are presented. The thesis is concluded in the Chapter 5.

CHAPTER 2

SPACE RADIATION, RADIATION EFFECTS ON MATERIALS AND BULK METALLIC GLASSES

In this section, fundamental concepts and a literature review necessary for the theoretical background of the experimental work presented in this thesis will be given. First, space radiation environment and radiation effects on materials will be presented. Afterwards, an introduction to the properties of bulk metallic glasses (BMGs) which were studied experimentally under radiation will be given.

2.1 Space Radiation Environment

Space radiation environment has a critical impact on electronics that are used in spacecraft. Therefore, the understanding of this environment is important for successful missions. First, Earth orbits and types of space radiation environment will be discussed to understand the space environment better. The effects of this environment on electronic components in various Earth orbits also will be given.

2.1.1 Earth Orbit

Space radiation environment around the Earth will be studied here in three categories of Earth orbits: low Earth orbit (LEO), medium Earth orbit (MEO) and geostationary Earth orbit (GEO), each of which serves a different purpose. In Table 2.1, orbit altitude ranges and approximate annual received doses for components inside a shielded satellite in LEO, MEO and GEO are shown. As seen, received average annual dose changes with the altitude of the orbit because each Earth orbit has a different domi-

nant space radiation component [4]. Satellites are used for Earth observation, communication, weather predictions and navigation. Access to LEO is easier and most Earth observation satellites and manned missions are in LEO such as the International Space Station (ISS). MEO satellites have a higher altitude, which allows for a larger communication range as well as a better estimate on the position of the satellite due to less drag. GNSS (Global Navigation Satellite Systems) satellites are in MEO. GEO holds satellites fixed on one longitude at the Equator. Therefore, satellites look motionless from a fixed position on Earth. In this orbit, there are many communication and meteorological satellites [5].

Table 2.1: Earth orbit altitude ranges and approximate received doses for different Earth orbit types. Each orbit type, has a different dominant space radiation environment, which results in a different average dose assuming the outer shielding aluminum thickness of the satellites is 2.5 mm [6].

Orbit Type	Altitude Ranges	Dose
Low Earth Orbit (LEO)	160 km - 2000 km	0.1 krad/year
Medium Earth Orbit (MEO)	2000 km - 35786 km	100 krad/year
Geostationary Earth Orbit (GEO)	About 35786 km	10 krad/year

Many developed countries like USA, Russia, China and the EU have series of satellites that serve all these purposes and they are launching new ones every year to improve their existing capabilities in space. Moreover, many developing countries are looking to improve and advance their space assets. Therefore, the number of satellites in space are increasing steadily [7]. However, several satellites in each year do not complete their operational designed mission durations due to the design inefficiencies, quality control issues and space environment effects. An important consideration is the space radiation environment which may grievously damage spacecraft electronics. According to statistics, the reason of the incomplete missions are due to space radiation (9 to 21%), electronic problems (6 to 16%), design problems (11 to 25%), quality problems (1 to 8%), other problems (11 to 33%) and problems that are still unknown (19 to 53%) [8].

Accumulated damage or a Single Event Effect (SEE) that is a result of electrons and protons in space, may cause reduction of the lifetime of electronics or a complete disruption. Radiation environment in space needs to be understood first to mitigate the effects of this significant problem. This environment composes of three main components: trapped particles in the radiation belts, galactic cosmic rays and solar particle events. It consists of energetic particles in the range from keV to GeV and above [9]. The degradation of electronic components and materials of satellites depend on particle type such as protons and electrons and flux encountered in Earth orbit. Energetic particles are trapped by the Earth's magnetic field and accumulated energetic particles in certain regions form the radiation belts. Therefore, the areas near these belts have higher radiation due to the higher number of energetic particles.

2.1.2 Effects of Space Radiation on Electronic Components in Earth Orbit

Satellites are placed in Earth orbit according to their operational requirements and mission purposes. When selecting the appropriate orbit, space environment should also be considered rigorously. The altitude of Low Earth Orbit is from 160 km to 2000 km therefore, it is used for Earth observation and remote sensing such as observation and spy satellites. Also the International Space Station is in that orbit due to easy access and lower radiation environment for astronauts [7]. However LEO suffers from the South Atlantic Anomaly and the pole regions where the radiation is higher due to Earth's complicated magnetic field. MEO is almost at the center of the outer radiation belts which results in more radiation and is eminently variable because of the solar cycle. Therefore, MEO is often not preferred unless necessary, such as for GNSS satellites. In MEO, atmospheric drag is less than in LEO which makes the orbit consistent and more predictable. It is closer to Earth than GEO and it completes an orbit in 12 hours [10]. GEO's altitude is about 37586 km, hence outer radiation belts, solar flares and cosmic rays play important role in this orbit. Communication and weather satellites are placed in GEO [11]. In order to avoid the detrimental effects of space radiation, convenient precautions should be taken such as shielding, radiation-hard components and realistic mission times [6, 12]. Two main kinds of deterioration mechanisms exist for components and materials. The first one is cumulative effects like deterioration of the electronics and corrosion of materials. The second one is the

intermittent and sudden effects like noise in electronics and Single Event Effects [13]. These will be discussed in Section 2.2.2.

2.1.3 Types of Space Radiation Environment

Trapped radiation, galactic cosmic rays and solar particle events, contribute to the space radiation environment in Earth orbit. These are all effected by the solar cycle. Understanding of the solar cycle is critical to model the space radiation because the Sun is both a source and a modulator of space radiation. The duration of the solar cycle is roughly 11 years. During this cycle, there are 7 years when the solar activity is high. In this period, a huge number of sunspots can emerge. This is followed by 4 years of solar minimum when the solar activity is low. In this period, the intensity and number of solar flares and sunspot activities decreases. The fluxes of the solar particles depend on the solar cycle which is variable and also sporadic. Now each kind of space radiation will be discussed in more detail.

2.1.3.1 Trapped radiation

Trapped radiation consists mainly of protons, electrons and a smaller amount of heavy ions which come with solar winds and cosmic rays and are later trapped in Van Allen radiation belts owing to Earth's magnetic field. The atmosphere is preserved from destruction from heavy radiation due to this trapping effect [14]. In Figure 2.1, the flux of particles in Van Allen radiation belts around the Earth are shown on a color scale. The inner Van Allen Belts placed between 6000 and 12 000 km (1 - 2 Earth radii, R_E) above Earth's surface and the outer belt is located from 25 000 to 45 000 km (4 to 7 R_E) [15].

The high concentration of the electrons that have hundreds of keV energy and energetic protons with energies exceeding 100 MeV are trapped in the inner radiation belt which is shown with a red arrow. The outer belt is indicated with a blue arrow and contains electrons in the range of 0.1–10 MeV that are trapped by the Earth's magnetosphere [12]. The color scale represents the intensity of radiation in arbitrary units. Belts are significant hazards for satellites and spacecraft if they spend considerable

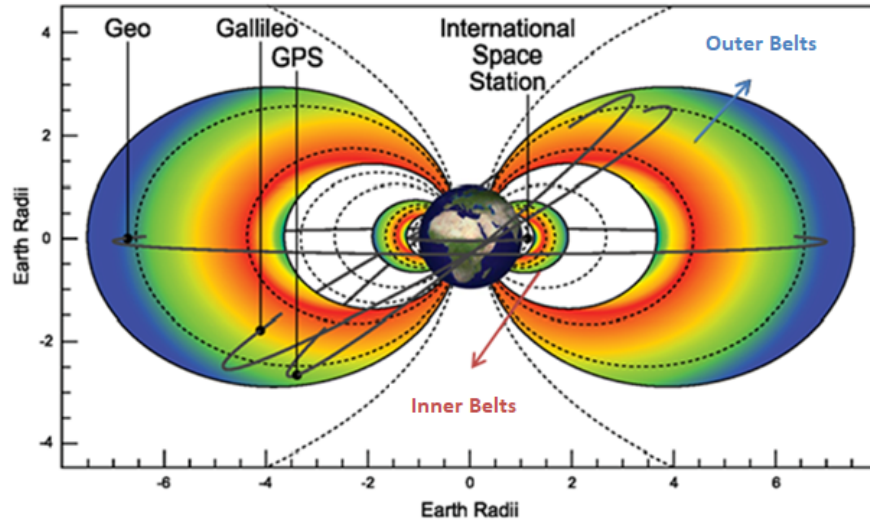


Figure 2.1: Van Allen Radiation Belts around the Earth. Outer radiation belt which extends from 4 to 7 Earth Radii (R_E) is shown with a blue arrow where mainly electrons are trapped and, inner radiation belt around 1 - 2 R_E is indicated with a red arrow where protons are trapped [16].

time in these areas. South Atlantic Anomaly (SAA) is an area in which the Earth's inner Van Allen Belts is nearest to the Earth's surface [17]. Hence, SAA is most critical part for low altitude orbits when deciding the radiation levels for spacecrafts. The increased flux of energetic particles in this zone in LEO often result in increased radiation damage. Therefore, satellites should avoid critical operations and consider shutting down some sensitive components when passing through this region as well as have properly designed shielding [8, 13].

2.1.3.2 Galactic cosmic rays

Galactic cosmic rays come from the outside of our solar system but from our galaxy. Their main source is thought to be supernova explosions [18]. Galactic cosmic rays consist of about 87% protons, 12% alpha particles and 1% heavier nuclei [8] and their energies can reach up to 10^{11} GeV. Their fluxes range from 10^{-2} to 1 particle/ s^{-1} and their spectrum up 30 GeV can also be affected by the solar cycle. They are hazardous for electronics inside the satellites and lead to Single Event Effects (SEE) in electronic components [19].

2.1.3.3 Solar particle events

Solar particles are composed mostly of protons and also a small amount of electrons and alphas. These are emanated from the Sun during solar storms. Solar flares are the consequence of enormous energy storage in the coronal magnetic field and its discharge. Contrarily, coronal mass ejection (CME) leads to the eruption of a huge plasma and therefore particles are accelerated by a shock wave [8]. In Figure 2.2, coronal mass ejection from the sun is seen. Such a CME, if directed towards the Earth, can cause major geomagnetic disturbances on Earth. It is proton rich and has a poor ^3He content compared to ^4He . CMEs are one type of solar particle events and they are composed of 96.4% protons, 3.5% alphas and 0.1% heavier ions. Satellites can be exposed to a significant level of total fluence during their mission due to these events. Solar particle events include predominantly electrons, protons and alphas [13] [20].

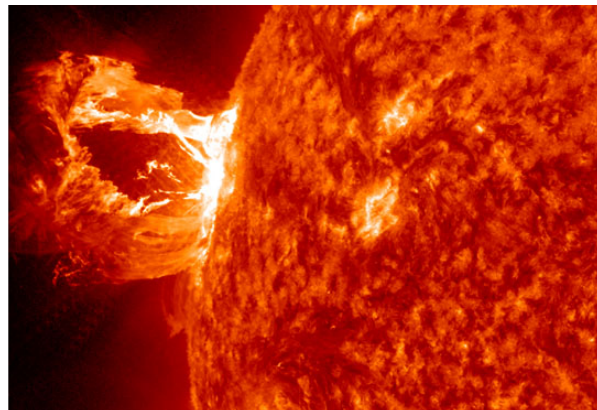


Figure 2.2: A coronal mass ejection from the Sun dated April 16, 2012 as observed by the SOHO satellite. This type of solar particle event consists of 96.4% protons, 3.5% alphas and 0.1% heavier ions [21].

2.2 Radiation Effects on Materials

Radiation is an electromagnetic wave or a particle that is emitted or transmitted through space or inside a material [22]. While electromagnetic radiation comprises of radio waves, microwaves, infrared, visible light, ultraviolet, X-rays and gamma rays,

particle radiation consists of alphas, betas, protons, neutrons and heavy elements. Radiation is also divided into two types, called non-ionizing and ionizing radiation. The first one does not have sufficient energy to ionize atoms and molecules. It can only cause excitation that carries electrons to a higher energy state while passing through the material. Electromagnetic non-ionizing radiation has a longer wavelength, a lower frequency and hence a lower energy [23]. On the other hand, the electromagnetic ionizing radiation has enough energy to ionize atoms and molecules when penetrating the material and it has a short wavelength, a high frequency and therefore a higher energy. This type of radiation can cause biological damage in living organisms such as skin burns, cataract or even death in short but sudden exposure and cancer or genetic disorders in long but slow exposure [24]. In Figure 2.3, the electromagnetic spectrum is seen. From the visible to lower frequency, non-ionizing radiation range is indicated with a blue band. A yellow band marks the visible to higher frequency range which is ionizing radiation.

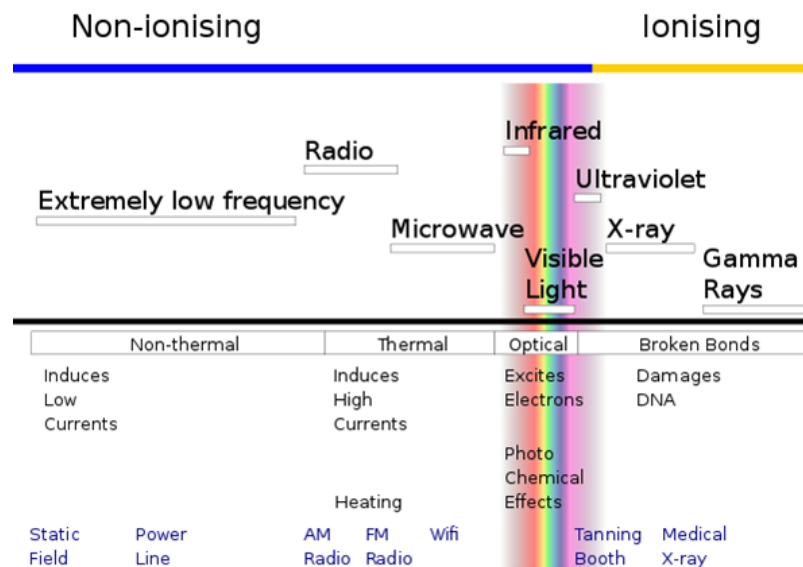


Figure 2.3: The electromagnetic spectrum. From the visible to lower frequency, non-ionizing radiation range is indicated with a blue band. A yellow band marks the visible to higher frequency range which is ionizing radiation. [25].

2.2.1 Particle Types and Their Ranges in Materials

A harmful result of radiation is called radiation damage. Dangerous radiation comes in the form of charged particles such as protons, betas (electrons), alphas and ions as well as neutral radiation such as neutrons, X-rays and gammas.

Charged particles penetrate materials depending on their kinetic energy. The penetration depth of a charged particle inside a material before it loses all its energy is called a "range". Alphas have higher mass and double the charge of proton therefore, their penetration depths are lower than protons with the same kinetic energy [26]. Heavier ions with a similar energy can be stopped easily inside a material, since they deposit their entire energy in a shorter distance. Alphas, that typically have a 5 MeV energy, can be stopped in a thin sheet of paper, while electrons and protons of a similar energy can be stopped in aluminum. Electrons multiple-scatter in the materials, which result in deviations from their initial trajectory [27]. This occurs because of a high density of same-mass electrons in the matter, where a high momentum-transfer in the scattering process is allowed. In Figure 2.4, the range of protons, electrons and alphas in aluminum is shown. For instance, the range of a 2 MeV electron, proton and alpha in aluminum are approximately 3.5 mm, 50 μm and 8 μm respectively.

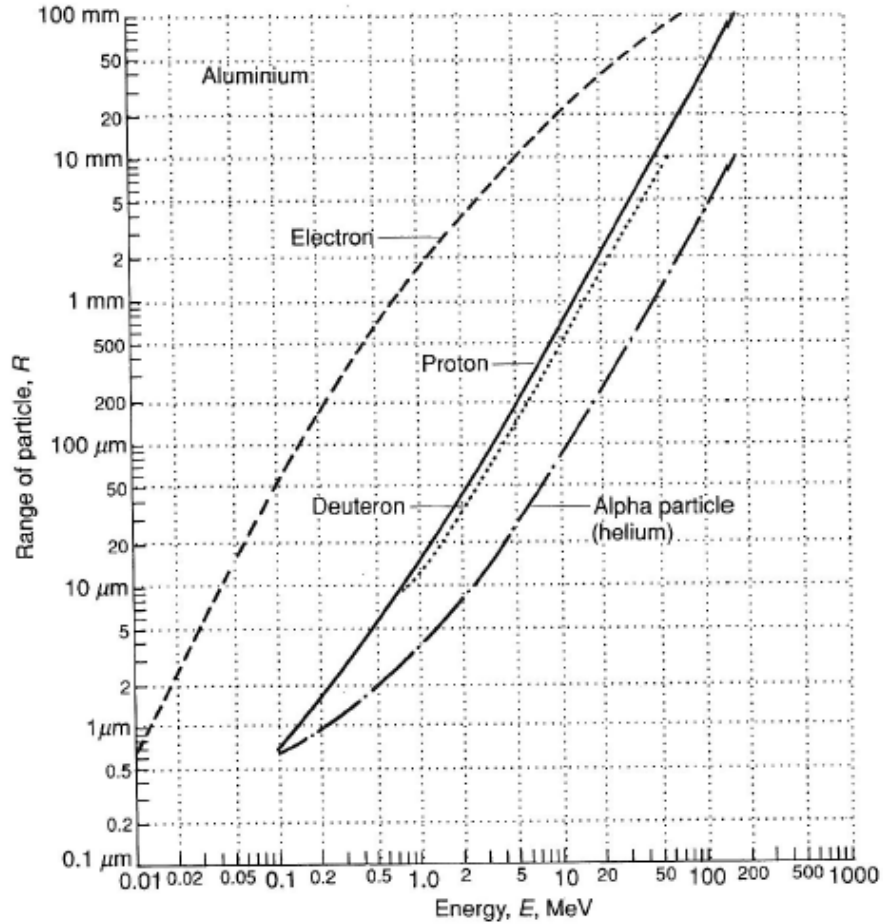


Figure 2.4: The range of protons, electrons and alphas in aluminum with respect to kinetic energy. For instance, the range of a 2 MeV electron, proton and alpha in aluminum are approximately 3.5 mm, 50 μm and 8 μm respectively [19].

Hard X-rays (typically with energies greater than 10 keV), gammas which have an energy higher than 1 MeV and neutrons have a high penetration depth therefore, heavy metals like lead, bismuth and tungsten are used to stop X-rays and gammas [28]. On the other hand, neutrons can only be slowed down using high hydrogen content materials such as polyethylene, paraffin, concrete and water because they have a high neutron scattering cross-section [29]. The energy loss per unit path length is expressed as "stopping power"; often plotted as in Figure 2.5, and is called as a Bragg curve. This curve shows the energy loss and the path length of an alpha particle in air. The total path length is equal to 4.15 cm. This curve can be drawn for any charged particle and various materials.

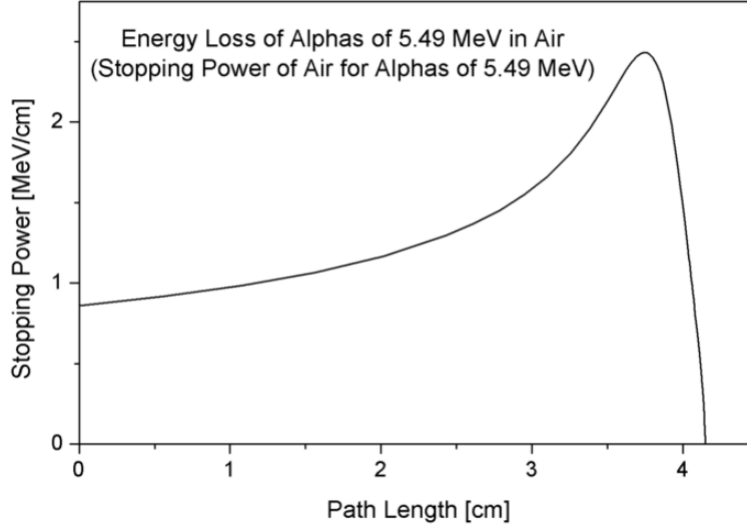


Figure 2.5: Bragg Curve for an alpha particle stopping in air. The alpha particle suffers a catastrophic loss of energy towards the end of its path, called a Bragg peak [30].

The interaction between charged particles and matter can occur in two ways. First is the energy loss of a charged particle as a result of collisions with electrons in the material. The second is the deviation of a particle from its initial direction due to hard scattering from nuclei. Energy loss of a charged particle or alternatively the stopping power of a material is expressed by the Bethe Bloch formula and it is indicated as $-\frac{dE}{dx}$. This formula is shown in Equation 2.1 [31].

$$-\frac{dE}{dx} = 2\pi N_a r_e^2 m_e c^2 \rho \frac{Z z^2}{A \beta^2} \left[\ln \left(\frac{2m_e \gamma^2 v^2 W_{max}}{I^2} \right) - 2\beta^2 - \delta - 2\frac{C}{Z} \right] \quad (2.1)$$

where the following variables are employed:

r_e : classical electron radius

m_e : electron mass

N_a : Avogadro's number

I : mean excitation potential

Z : atomic number of absorbing material

A : atomic weight of absorbing material

ρ : density of absorbing material

z : charge of incident particle in units of e

$\beta = v/c$ of the incident particle

$\gamma = \frac{1}{\sqrt{1-\beta^2}}$, Lorentz factor

δ : density correction

C : shell correction

W_{max} : maximum energy transfer in a single collision

so that $2\pi N_a r_e^2 m_e c^2 = 0.1535 \frac{MeV.cm^2}{gr}$

In this formula, Density (δ) and Shell (C) corrections also are added because they are important for high and low energies respectively. Bethe-Bloch formula expresses the energy loss of charged particles in matter and it is alternatively the stopping power of the material because the energy loss of particles is equal to stopping power of material numerically. Stopping power is expressed as;

$$S = \left(\frac{dE}{dx} \right)_{nuclear} + \left(\frac{dE}{dx} \right)_{electronic} \quad (2.2)$$

Electronic energy loss results from collisions between electrons in the material and the incoming particle. On the other hand, nuclear loss is due to collisions between the nuclei in the material and the particle. While the nuclear stopping is higher at low energies, it decreases when the energy increases. At low energies, nuclear stopping is greater than the electronic and the nuclear stopping power is inversely proportional to energy. Electronic stopping is higher than nuclear stopping at high energies.

The Bethe-Bloch formula is very useful for the understanding of interaction of a charged particle in a material. Particles travel through a material with regard to their energy and also the density of the material. As seen from Bethe-Bloch formula, the energy loss is directly proportional with the density of the absorbing material and square of the charge of the incoming particle. For instance, the energy loss of a 30 MeV proton in tungsten is higher than in aluminum due to the density of tungsten. Also, a helium nuclei leaves ≈ 4 more times energy in the material than a proton because the helium is doubly charged. Interaction of the protons in various material is shown in Figure 2.6 with respect to $\beta\gamma$ which is velocity times the Lorentz fac-

tor of the particle. The minimum of each curve for different materials indicate the minimum ionization loss a particle can suffer in that material. This point is called a minimum-ionizing particle (MIP) and occurs at $\beta\gamma \approx 3$ and for aluminum this minimum energy loss is $\approx 2 \text{ MeV/gr/cm}^2$. The stopping power roughly decreases like $1/v^2$ with increasing particle velocity up to the MIP energy. However, it rises slowly with energies higher than the MIP energy. Since this rise is very slow, most relativistic particles can be considered as MIPs.

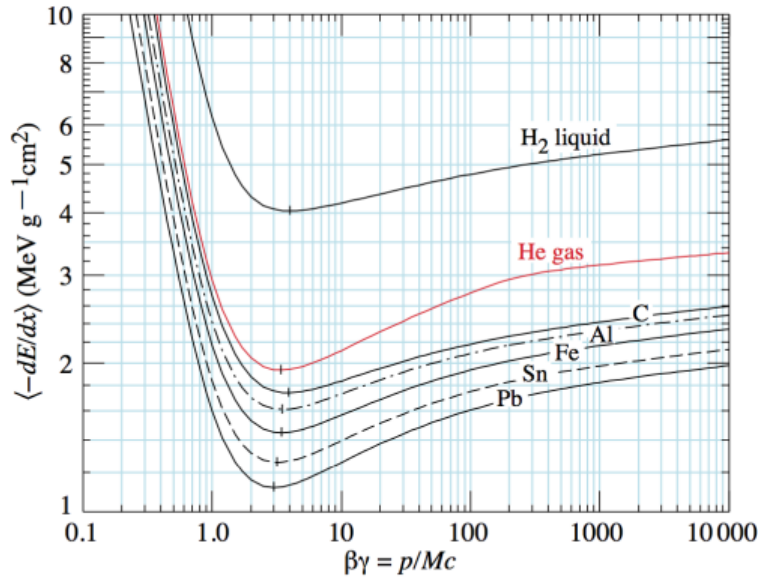


Figure 2.6: The Bethe-Bloch plot shows the interaction of the protons in material. Energy losses of protons in different materials are shown with respect to $\beta\gamma$ which is velocity times the Lorentz factor of the particle [32].

The energy deposition of a particle inside a material is called as "Absorbed Dose". Rad and gray(Gy) units are both used, but gray is the SI unit while most literature in space radiation still uses rad. 1 Gray is an absorption of one joule of particle energy per one kilogram of absorbing material. 1 rad is equal to 0.01 gray(J/kg).

2.2.2 Radiation Damage Mechanisms

Radiation damage mechanism are classified into two as long term and short term effects. While single event effects (SEEs) are short term effects, total ionizing dose

(TID) and displacement damage (DD) are long term effects. Long-term effects are the cumulative deterioration of a device during its mission time. Now, these mechanisms will be discussed.

2.2.2.1 Total Ionizing Dose (TID)

Total ionizing dose is caused by the cumulative ionizing effect of protons and electrons that are trapped in radiation belts and also from solar flares. It can lead to device failure in spacecraft. The unit of TID is the total absorbed dose that is the absorbed energy by a material. While, in LEO, the main contribution to total ionizing dose is from trapped electrons and protons, in GEO, it is from electrons and solar protons. Even small changes in altitude, inclination and mission time can cause severe changes in the total ionizing dose deposited in the spacecraft [33].

2.2.2.2 Displacement Damage (DD)

Displacement damage (DD) is the accumulative non-ionizing radiation damage in the long term. In Figure 2.7, an illustration of displacement damage is seen where the incoming particle loses its energy by colliding with the nuclei of the material. As a result of the collision, the lattice atom leaves its original position. Such an atom is called a primary knock-on. Replaced atom forms an interstitial and its old empty position is called a vacancy. Sometimes a replaced atom can cause another collision and displace yet another atom in the crystal. An interstitial and a vacancy together form a Frenkel pair. DD can be calculated by using non-ionizing energy loss (NIEL). The unit of NIEL is MeV/cm or $MeV.cm^2/g$. Heavy ions, protons and alphas, which cause DD, can either lead to transient or permanent single event effects because of broken bonds.

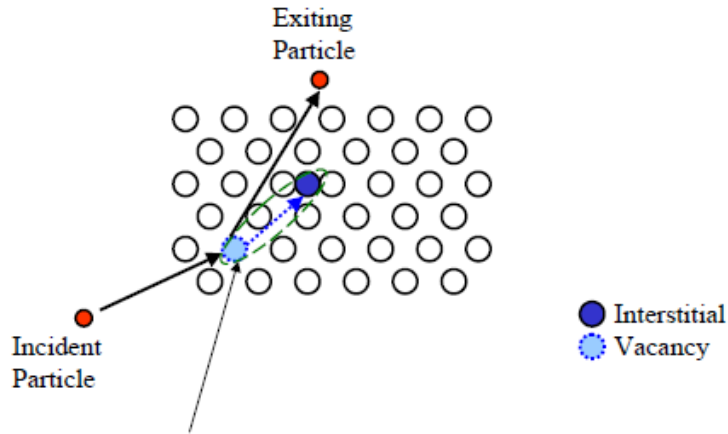


Figure 2.7: Displacement damage in a lattice occurs when an incoming particle displaces a lattice atom in a collision. An interstitial and a vacancy are created and are shown in dark blue and light blue respectively [34].

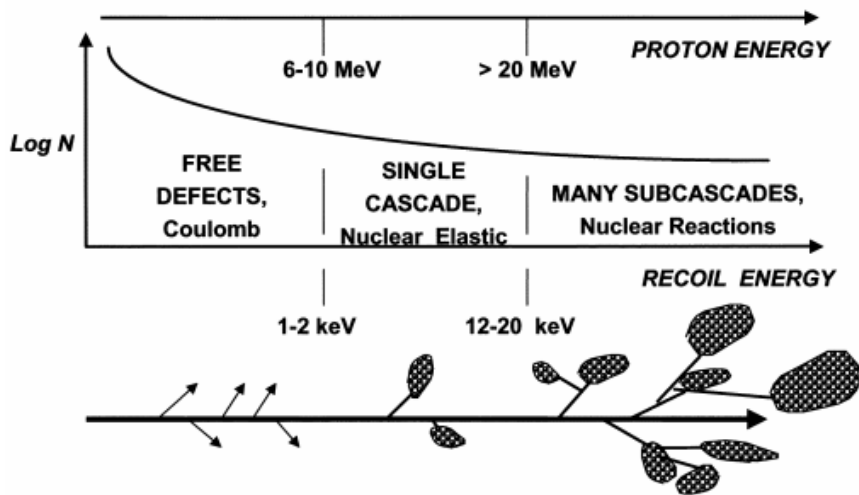


Figure 2.8: Displacement damage in silicon due to proton irradiation [35].

In Figure 2.8, displacement damage mechanism of protons in silicon is illustrated. In the upper panel, it shows the log of the number of interactions versus the incident proton kinetic energy. In the lower panel, it shows the path of secondary products. At energies below 6 MeV, Coulomb interactions dominate and generates free electrons and primary knock-on atoms with an energy of less than 2 keV. Above ≈ 6 MeV, nuclear elastic and reaction events generate cascades which results in displacement

damage. At higher proton energies, (> 20 MeV) atoms recoil with energies in excess of 12–20 keV and produce multiple subcascades similar to a tree-like structure.

METU-DBL works with protons in the range of 15-30 MeV which allows for DD effects to be explored.

2.2.2.3 Single Event Effects (SEE)

When a single and energetic particle strikes a sensitive electronic device, this can lead to a Single Event Effect (SEE). These effects are hazardous especially for digital electronic components. SEEs can either be destructive and non-destructive [36]. In Table 2.2, types of single event effects and the resulting errors are seen. Some of these errors are soft, and some are hard errors. Soft ones are transient errors caused by charged particles and these particles can, for example, alter the charge on a memory cell, but they do not damage the device. Therefore, these errors can be corrected by rewriting the memory cell with the correct data. On the other hand, a hard error on a memory device, for example, is caused by a connector error and/or faulty capacitor. These are repeating errors and need some hardware correction such as the replacement of a connector or the memory device [37]. SEEs are frequently expressed with the linear energy transfer (LET). It is the amount of transferred energy from ionizing particle to the material per unit distance. It is given in units of MeV/cm [38].

Table 2.2: Types of Single Event Effects and the resulting errors. SEU, SET, SEFI, SES are soft, while SEL, SEB and SEGR are hard errors [39].

Abbreviation	Types of SEE	Errors
SEU	Upset	Change in state of microprocessor or memory (Soft)
SET	Transient	Transient voltage pulse produced in node (Soft)
SEL	Latchup	Unusual high current state (Hard)
SES	Snapback	High-current state (Soft)
SEB	Burnout	High-current state that causes calamitous failure (Hard)
SEGR	Gate Rupture	Damage of the ability of gate to manage current flow (Hard)
SEFI	Functional Interrupt	Device pauses normal operations (Soft)

SEEs can be created either by heavy ions or by protons while they pass through the electronics. While heavy ions cause "direct ionization", the latter lead to "indirect ionization". When heavy ions pass through the material, they deposit most of their energy in the sensitive part of electronics and they create an ionization line similar to the depiction in Figure 2.9. On the other hand, protons can cause a nuclear scattering reaction close to the sensitive part of the device, which is called "indirect ionization" [40]. Radiation tests conducted at METU-DBL is sensitive to SEE effects due to this indirect ionization mechanism.

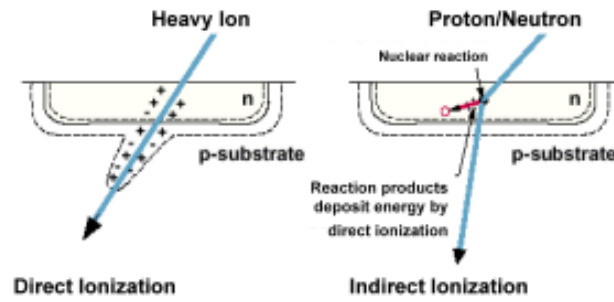


Figure 2.9: Direct and indirect ionization. Direct ionization is caused by heavy ions, while the indirect ionization is created by protons and neutrons [40].

2.3 METU-DBL Project

Turkish Atomic Energy Authority's Proton Accelerator Facility (TAEA PAF) is the only proton accelerator facility in Turkey that accelerate protons to higher than 20 MeV kinetic energy. In Turkey, the number of low energy (<20 MeV) cyclotron type accelerators is 12 and all of these accelerators are used for FDG (Fluorodeoxy-D-glucose) production [41]. FDG which has a ^{18}F isotope inside the molecule is used in tomographic imaging method performed with positron radiation and dedicated detectors. For example, Eczacıbaşı-Monrol produce FDG at several facilities for medical purposes [42]. TAEA PAF can produce various isotopes (^{123}I , ^{18}F , ^{111}In , ^{67}Ga , ^{201}Tl) as well as ^{18}F using the larger 15-30 MeV range of its accelerator. This also allows for space radiation tests according to ESA 25100 ESCC, which require a >20 MeV proton energy, to be performed here [43].

In the Figure 2.10, the schematic of the accelerator at TAEA PAF is shown. At the central right, a circular cyclotron is seen in red and it has four arms that spread into four different irradiation rooms. The room on the bottom left is the R&D room and black line is the METU-DBL which is controlled from the R&D laboratory to the left of the R&D room through control and signal cables installed in the trench (shown in red) between these two rooms. The cooling system of METU-DBL is situated in the Technical Room seen to the upper left of the R&D room. The main chiller of

TAEA PAF provides cooling power which is exchanged in the METU-DBL cooling system which then cools elements such as magnets and collimators. The connection is provided through cooling pipes connecting the Technical Room and the R&D room. The other three arms are the radio-pharmaceutical production rooms, namely solid target room (upper left), liquid target room (upper right) and gaseous target room (lower right). Isotopes produced here are used in the diagnosis of cancer and other medical conditions.

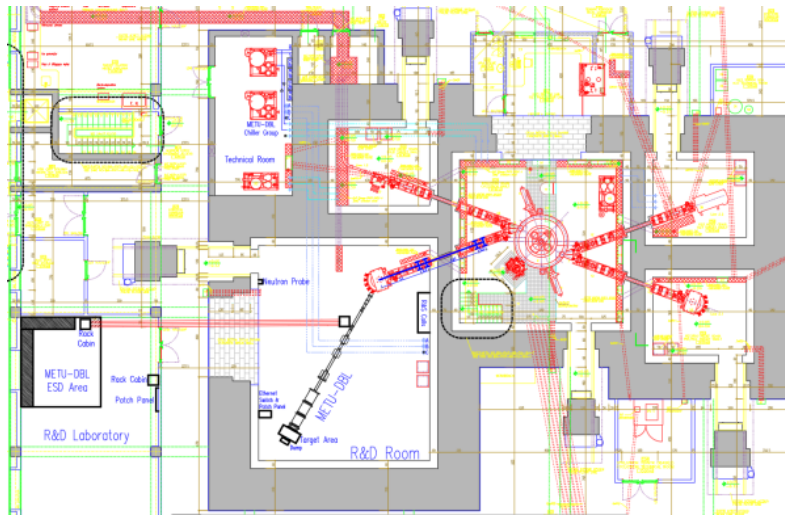


Figure 2.10: Drawing of TAEA’s Proton Accelerator Facility. At the central right, the circular cyclotron is seen in red and it has four arms that spread into four different irradiation rooms. The room on the bottom left is the R&D room and black line is the METU-DBL. The other three arms are the radio-pharmaceutical production rooms, namely solid target room (upper left), liquid target room (lower right) and gaseous target room (upper right) [43].

The R&D room is capable of conducting five different experiments thanks to a five port switching magnet procured by METU. METU-DBL uses the leftmost exit in Figure 2.10 of this switching magnet to perform radiation tests for space electronic components and materials with protons.

Radiation tests with METU-DBL should obey ESA ESCC No:25100 standard [44]. According to this standard, the beam flux should be in the range from 10^5 p/cm²/s to at least 10^8 p/cm²/s and the dimension of the beam should be to 15.40 cm x 21.55 cm.

Kinetic energy of the proton beam should include 5 test points between 20 MeV and 200 MeV. Here, only one test point between 14.3-29.3 MeV is available to the users and in a single test, the fluence should reach at least 10^{11} p/cm². Finally, the beam homogeneity in the test area should be better than $\pm 10\%$.

The TAEA PAF provides protons in the kinetic energy of 15-30 MeV which corresponds to 168 - 239 MeV in momentum range. Beam current is selectable between 0.1 μ A and 1.2 mA and the radius of proton beam at the exit of the TAEA R&D is about 1 cm. In order to meet these requirements, METU-DBL uses beam elements such as collimators and defocusing magnets. The drawing of the METU-DBL is provided in Figure 2.12. The full length of METU-DBL is 7.36 m. The beam enters from the left of the figure. The first two elements are a beam stopper and a vacuum shutter. In case of an emergency, such as loss of vacuum, METU-DBL can activate these two systems to cut the beam or separate the vacuum of METU-DBL and TAEA. The activation time of the beam stopper is ≤ 2 second [45] and the vacuum shutter is ≤ 4 second [46]. The vacuum of both systems in operation are better than 10^{-5} torr. While the beam stopper should be placed before the vacuum shutter to protect it from the beam, as the writing of this thesis, the two were still reversed because the necessary permissions could not be obtained from TAEA PAF.

Next is a scattering section where two 50 μ m titanium foils are cooled by a 10 cm long helium chamber placed between them. This section scatters and enlarges the beam to have an average angle of 13.2 mrad in x and 13.7 mrad in y [47], which is then collimated 15 cm away to only allow for only the most uniform central part of the beam to continue along METU-DBL. This conic collimator, which shapes the beam in a conical square aperture, has an adjustable opening selectable between 1 mm to 2 mm and 9 mm to 10 mm. This changeable collimator aperture provides the desired fluxes by stopping protons [48]. After a flight path of 97 cm, a protective collimator with an opening of 1 cm shields the ensuing defocusing quadrupole magnets from stray particles from the collimator section before it. While two of these magnets are supplied commercially from Scanditronix, the third one was designed by METU-DBL team and produced in Turkey at Sönmez Trafo [49] with CERN knowledge transfer. Mag-

netic and electrical tests of this magnet were first performed at TUBITAK UME and then at CERN and now this magnet is CERN certified. The images of third magnet and its certificate are seen in Figure 2.11.



Figure 2.11: The images of third magnet and its certificate from CERN. First image (middle above) is taken at CERN during the magnetic tests of the magnet. The second image (below left) is taken in TAEA PAF and the last image (below right) is the certificate of the magnet from CERN.

After this third quadrupole magnet, a long flight path of 2.97 m provides a large test area at the end of the beamline. A test and measurement table moves the DUT (device under test) and three different detectors (diamond, fiber scintillators and Timepix [50]) in and out of the test area. The detectors measure the flux and uniformity of the beam. A final beam dump stops all protons at the end. A bird eye view of METU-DBL is shown in Figure 2.13.

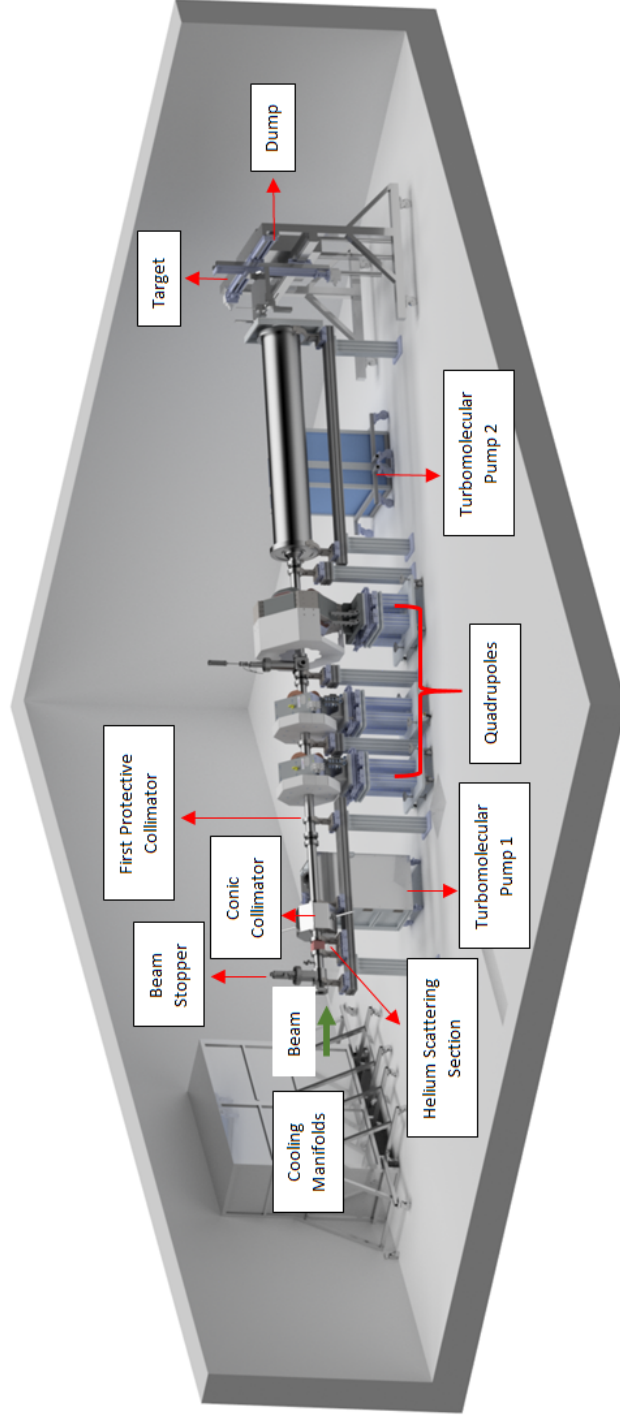


Figure 2.12: A drawing of the METU-DBL. The beam enters from the left side of the figure. In the drawing, critical beam elements used in case of emergency, namely a beam stopper and a vacuum shutter, are seen at the beginning of the beamline. Three quadrupole magnets follow a scattering section. The beam pipe grows larger after the magnets to reflect the defocusing beam. The measurement table and the beam dump are seen at the end of the beamline. The total length of METU-DBL is 7.36 m [51].

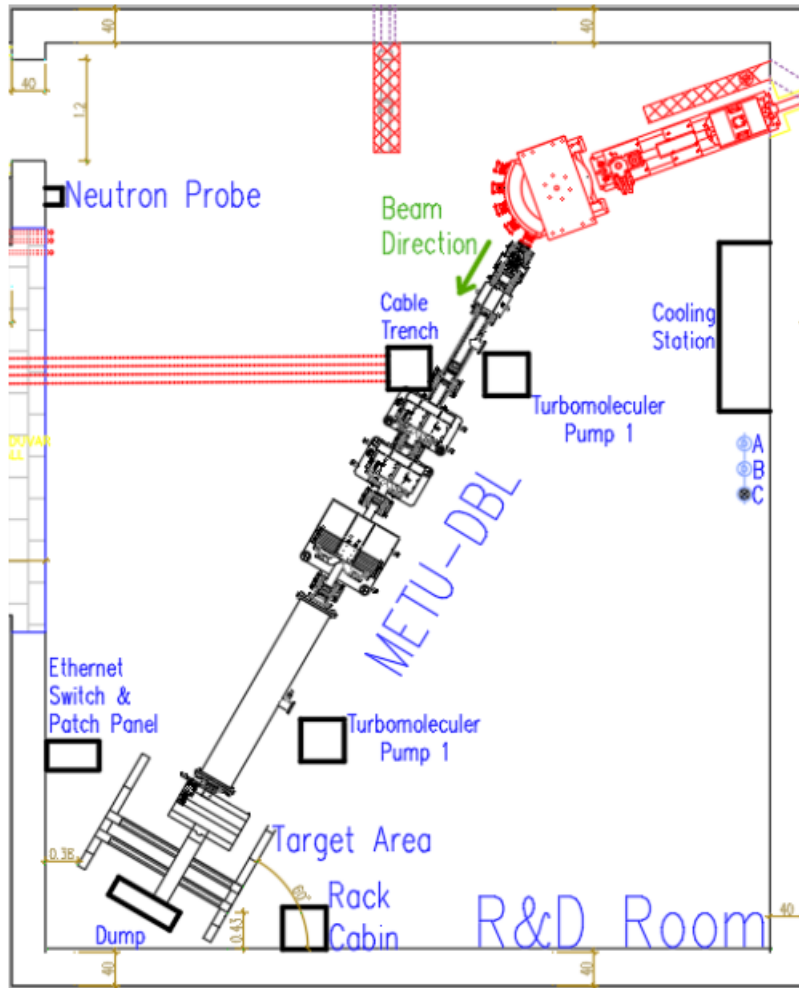


Figure 2.13: A bird eye view of METU-DBL. A user can easily pass behind METU-DBL, which was a design criteria. A large experimental area to the right of the test area is available for user electronics. The beam direction is indicated in green [52].

For beam-optics design and secondary particle production as well as activation analyses of METU-DBL, different programs are operated in comparison. For the beam optics calculations, C++ based MAD-X and FORTRAN based Transport programs are used. For particle tracking studies, FORTRAN based TURTLE and C++ based G4Beamline programs are employed. This comparison of essentially different simulation programs enhance reliability of the design. Furthermore, calculation of the dose rates of secondary particle production, energy deposition as well as activation and shielding design for electronic components are studied using FLUKA [53].

METU-DBL has several subsystems: beam optics, cooling, vacuum, control, test and measurement subsystem [54]. The beam optics subsystem consist of a helium scattering section and three quadrupole magnets. The adjustable opening of the conic collimator and the current setting of the quadrupole magnets determine the beam size at the end of METU-DBL. The cooling system is used to cool beam elements like magnets, dump and collimators, using pressurized water. Cooling water passes through a resin tube in the Technical Room to reduce the activation of water due to the radiation. Protons lose energy in air so, they are under vacuum in the beam line and this is controlled by a vacuum subsystem. There are two types of vacuum pump in this system: a mechanical and a turbomolecular pump which jointly provide a vacuum level of around 10^{-6} torr. The control subsystem monitors and controls all subsystems in the METU-DBL from the R&D laboratory. The test and measurement system is responsible for measuring the beam flux at the target region and also determining the beam profile in unison to provide users a selectable flux menu from 10^5 p/cm²/s to 10^{11} p/cm²/s [55].

2.4 Materials Under Irradiation

In radiation environments, material selection is critical for long mission duration. Several kinds of radiation tests are performed to see the durability of materials against radiation exposure, but most of them are carried out for the purpose of being used in nuclear reactors. In this case, neutron and heavy ion tests are applied to candidate materials. Although proton tests are required for the space environment due to it being the dominant radiation in this environment, examples of these tests in literature are only handful. In general, crystalline materials are used for these radiation environments, but more durable new generation materials are still being researched. One such category of them is bulk metallic glasses due to their superior properties. Their properties and their behavior under the radiation exposure will be given in the next sections.

2.5 Bulk Metallic Glasses

Bulk metallic glasses are a new generation of materials, with long-range disorder and short-range order (amorphous), and with superior properties such as high strength, excellent corrosion resistance and lack of grain boundaries [56, 57]. They carry both metallic properties like hardness and also glass properties like brittleness. Simple schematic illustrations of both amorphous and crystalline structures are shown in Figure 2.14. In crystalline materials, atoms are arranged orderly. Contrarily, amorphous materials have no crystalline structure and atoms are structured disorderly.

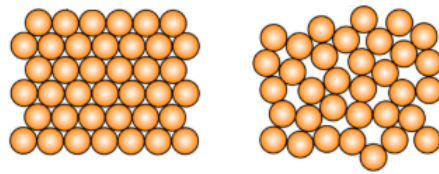


Figure 2.14: Comparison of structure of crystalline and amorphous metals. Crystalline metals (on the left), amorphous metals (on the right) are shown. While crystalline metals have ordered structure, amorphous ones are disordered, and have random structure [58].

BMGs are produced by cooling a metallic alloy very fast so that crystallization is prevented and atoms do not have enough time to arrange themselves for a crystalline structure [59]. In general, cooling rate is the critical parameter for the formation of structure and ensuing properties of metallic glass. Cooling rate should be high to produce a metallic glass either in ribbon or bulk form. In the melt spinning technique, the cooling rate can be as high as 10^6 K/s, but the sample is in the form of a ribbon with a thickness in the range of micrometers. However, to produce a BMG sample, the cooling rate should at least be 10^2 K/s and with the arc melting technique, their thickness is at least 1 mm [60]. This cooling rate for BMG production can be lowered by the addition of a large variety of elements into the alloy. There are restricted application areas for ribbon or film metallic glasses, while there are many applications areas of BMGs. With the advance of BMGs, the applications of the metallic glasses increased. BMGs are used in medical, defense and aerospace areas [61]. In this thesis, BMGs are studied for their radiation hardness properties.

Glass forming ability (GFA) is critical, for designing and developing new BMGs. GFA involves two constituents: the liquid phase stability and the resistance to crystallization. GFA of metallic glass and liquidus temperature T_l are inversely proportional to each other. Therefore, it shows the relative stability of stable glass forming liquids. The relation between glass forming ability and the liquidus temperature can be expressed as :

$$GFA \propto \frac{1}{T} \quad (2.3)$$

That is the lower T_l causes larger stability. In that case, the liquid may stay stable to a lower temperature and formation of any solid phases are not observed [62].

In this section properties of BMGs, their production techniques and possible effects of radiation on BMGs will be presented.

2.5.1 Mechanical Properties of BMGs

Bulk metallic glasses have superior mechanical properties than conventional materials. In Figure 2.15, comparison of amorphous and crystalline materials in terms of their strength and their elastic limit are seen. Glassy alloys have higher strength and elastic limits than crystalline ones, but plastic deformation are not seen much in these.

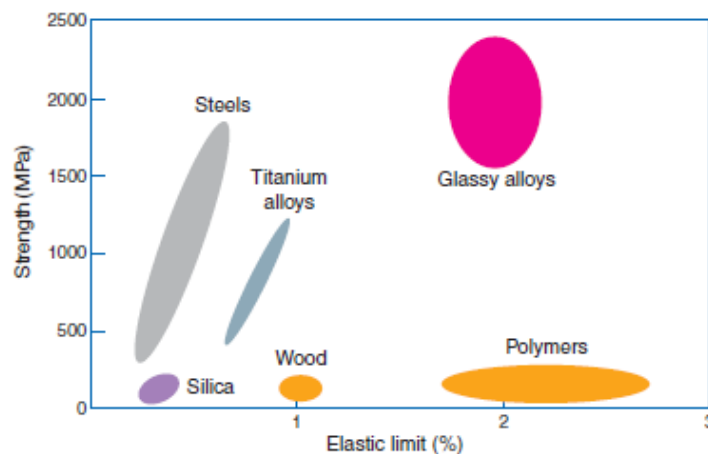


Figure 2.15: Comparison of amorphous and crystalline materials in terms of strength and elastic limit [59].

Elastic limit vs. Young's modulus graph is seen in Figure 2.16. Elastic limit vs Young's modulus plot is shown for 1507 materials. Each ellipse represents the range of values related with indicated materials and their groups. As seen, metallic glasses are located upper edge of the populated region. They have higher strength than other materials. The highest one has 5000 MPa and this indicates correlation with Young's modulus.

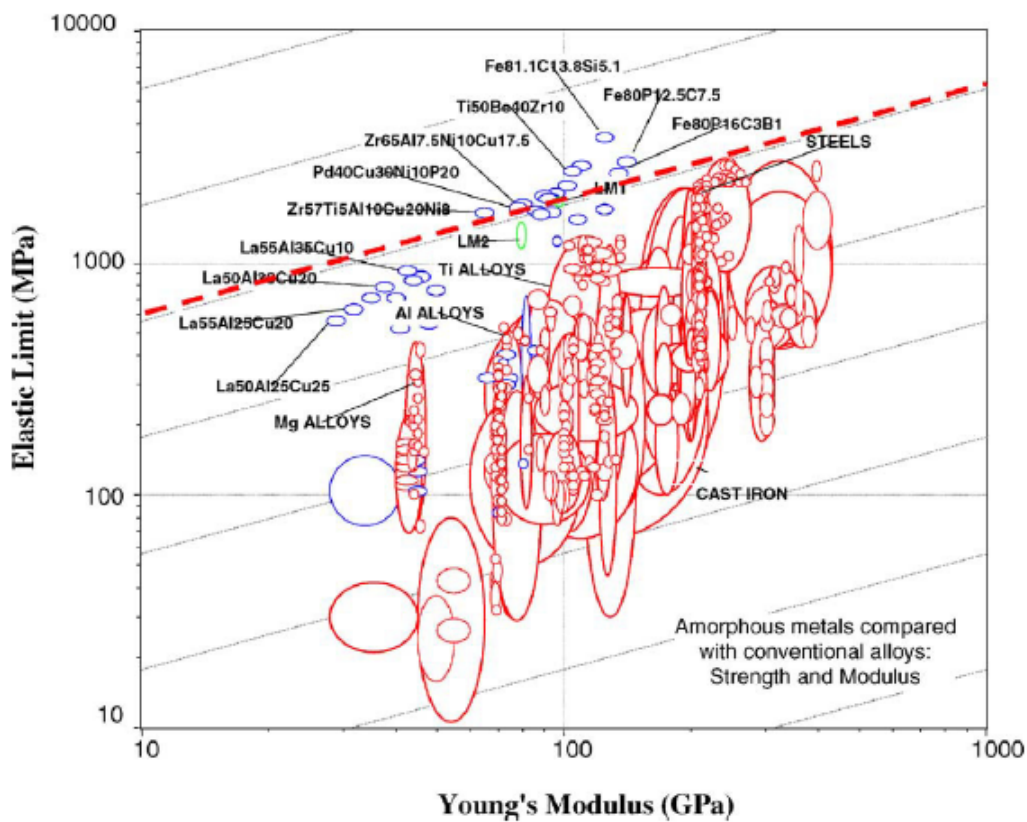


Figure 2.16: Elastic limit plotted against Young's modulus for 1507 metals, alloys, metal matrix composites and metallic glasses [63].

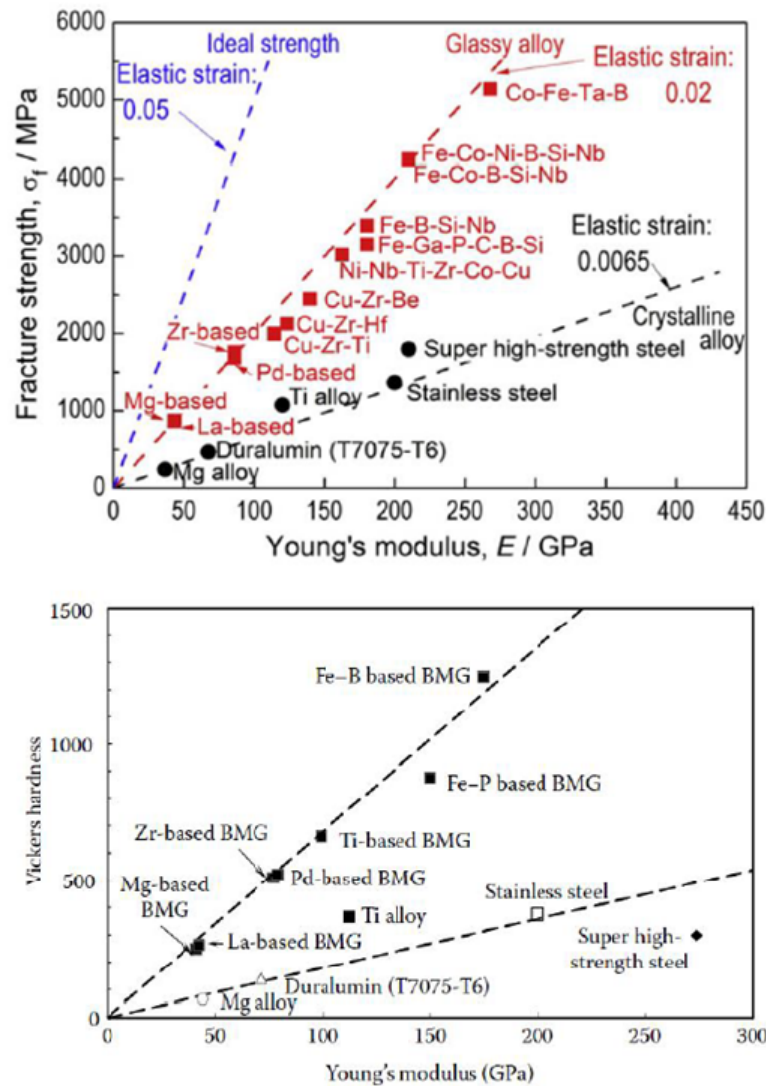


Figure 2.17: Relationship between fracture strength or Vickers hardness and Young modulus for various BMGs [64].

Figure 2.17 indicates the relationship between fracture strength or Vickers hardness and Young's modulus for BMGs and conventional crystalline counterparts. Fe-based BMGs have very high fracture strengths. Their strengths are between 3000 and 4000MPa which is 3-4 times higher than their crystalline counterparts. Also, Fe-based BMGs have high hardness. The hardness of Fe-based BMGs is between 900 to 1300HV and they are very higher than conventional steels and approximately 5 times higher than stainless steels. The mechanical properties of the BMGs are superior to crystalline alloys.

2.5.2 Magnetic Properties of BMGs

With the development of BMGs, Inoue and co-workers produced Fe-based BMG that has soft magnetic properties [65]. After this time, many systems were produced using Fe, Co and Ni and they were used in some applications such as ring-shaped microgears for micro-motors and magnetic yokes. Magnetic properties can be divided into two groups: soft and hard magnetic properties. Soft magnetic properties have low coercivity (commonly between 100 - 1000 A/m) and high magnetic saturation (generally between 0.75 - 1.50 T) [66, 67].

2.6 Fe-based BMGs

Numerous BMGs were designed in the last few decades. Among of them, most attractive ones are the Fe-based BMGs due to their mechanical properties like high corrosion resistance and high strength as well as good magnetic properties. Also they are low cost in comparison to other BMGs [68]. The historical development of the Fe-based BMGs from 1995 to 2010 is shown in Table 2.3. Each BMG has special properties. For example, Fe-B based BMGs have good soft magnetic properties. Fe-Co-Nb-Si-B BMGs have high strength over 4 GPa and Fe-Cr-Mo-C-B has a good corrosion resistance. Furthermore, several searches were conducted to find ductile Fe-based BMGs. Fe-Ga-P-C-B-Si, Fe-B-Si-Nb, Fe-Co-B-Si-Nb and Fe-Mo-C-B-Ln have higher ductility than other Fe-based BMGs. Here in this thesis, Fe-Co-Si-B-Nb and M-Cr-Mo-B-Y-Mn (M is the cast iron) are studied.

Table 2.3: The historical development of the Fe-based bulk metallic glasses [69].

Fe-based BMGs	Year
Fe-(Al,Ga)-(P,C,B,Si,Ge)	1995
Fe-(Nb,Mo)-(Al,Ga)-(P,B,Si)	1995
Fe-(Zr,Hf,Nb)-B	1996
Fe-Co-Ln-B	1998
Fe-Ga-(Cr,Mo)-(P,C,B)	1999
Fe-Ga-(Cr,Mo)-(P,C,B)	1999
Fe-Ga-(P,B)	2000
Fe-Si-B-Nb	2002
Co-Fe-Si-B-Nb	2002
Co-Fe-Ta-B-Si	2003
Fe-(Cr,Mo)-(C,B)-Ln (Ln = Y, Er, Tm)	2004
Fe-(Nb,Cr)-(P,B,Si)	2010

2.7 Bulk Metallic Glasses Under Irradiation

BMGs are a promising new generation of materials for radiation environments due to their superior mechanical, physical and chemical properties. They lack of grain boundaries and so BMGs have high corrosion resistance and high strength [3]. They are attractive candidates for irradiation environments because of their lack of crystal defects like dislocations. This property makes them preferential to crystalline ones. However, BMGs have point defects such as vacancy-like and interstitial-like defects [70]. An illustration of this is given in Figure 2.18. Target atoms can be displaced from its initial position when the energy transfer is high enough under ion or electron irradiation. Since, a vacancy-like defect forms and excessive free volume in the system rises, some properties of BMGs can be affected by this [71]. However, endurance of BMGs against radiation is altered according to chemical composition and additives and so these defects show some difference.

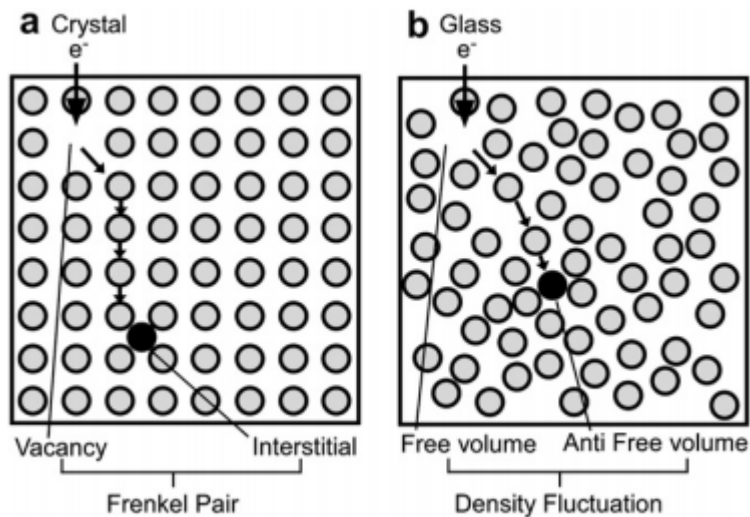


Figure 2.18: Schematic illustration of a defect created in a metallic crystal (left) and a metallic glass (right) under MeV electron irradiation [72].

One of the important fields searching for new materials is nuclear reactors and space applications which are both radiation environments. Space radiation environment is elucidated in Section 2.1 in detail. In space environment, mostly protons and electrons are found and only protons penetrate inside the satellites because electrons can be stopped by a thin aluminum shielding on the outside of satellite. Therefore, proton tests are crucial for space radiation environment. On the other hand, neutron and ion irradiations are essential for nuclear reactors and there are numerous studies of metallic glasses for nuclear reactors in literature. Particularly, Fe-based metallic glasses are thought as promising for future fusion reactors because they have a comparably high crystallization temperature, wide supercooled liquid region and less neutron activation [73].

Various techniques can be used in order to analyze the effects of radiation. Transmission electron microscope (TEM) [74] is performed for the atomic level analysis like displacement damage. Scanning electron microscope (SEM) [75] and optic microscope [76] are applied in order to observe the microstructural differences in the material before and after the irradiation. The phase structure analysis is studied by X-ray diffraction (XRD) [77] and by using differential scanning calorimetry (DSC) [78], thermal stability of glass transition and crystallization is characterized. Finally,

vibrating sample magnetometer (VSM) [79] is performed for the alteration of magnetic properties. Microhardness test [80] is performed for hardness results. These are all commonly used characterization techniques for the analysis of irradiated materials.

In the literature review, both bulk and ribbon form metallic glasses under irradiation were investigated. In the following examples, characterizations of samples before and after an irradiation are given.

As a first example, FeSiB metallic glass under 250 keV H^+ irradiation were examined [81]. XRD patterns of this material before and after the irradiation are seen in Figure 2.19, where each color represents four different fluences. As-cast sample is amorphous because it has one broad peak. After irradiations of different fluences, there is no sharp peak that is it remained amorphous. Significant changes are not observed in the phase structure of material. Therefore, different characterization techniques are used additionally. SEM analysis was also performed for this metallic glass [81] and images are seen in Figure 2.20. As-cast and irradiated metallic glasses with four different fluences are given. No delamination, exfoliation, blistering or cracking were observed on the samples. It shows that the surface morphology of the metallic glass did not change after the irradiation even with the highest fluence. It is still smooth and shows amorphous structure.

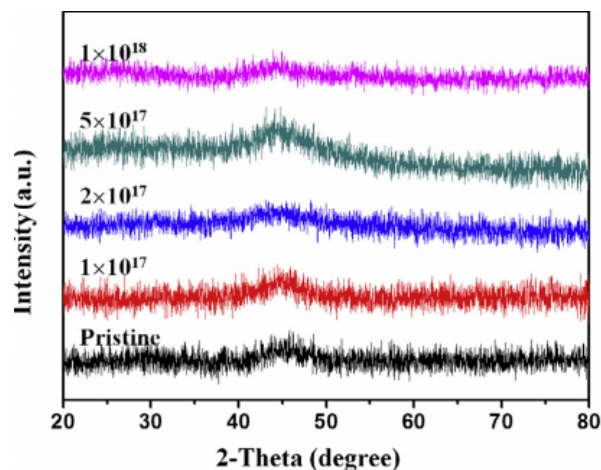


Figure 2.19: XRD patterns of FeSiB metallic glass before and after 250 keV H^+ ion irradiation. As-cast metallic glass and under four different fluences are seen in different colors [81].

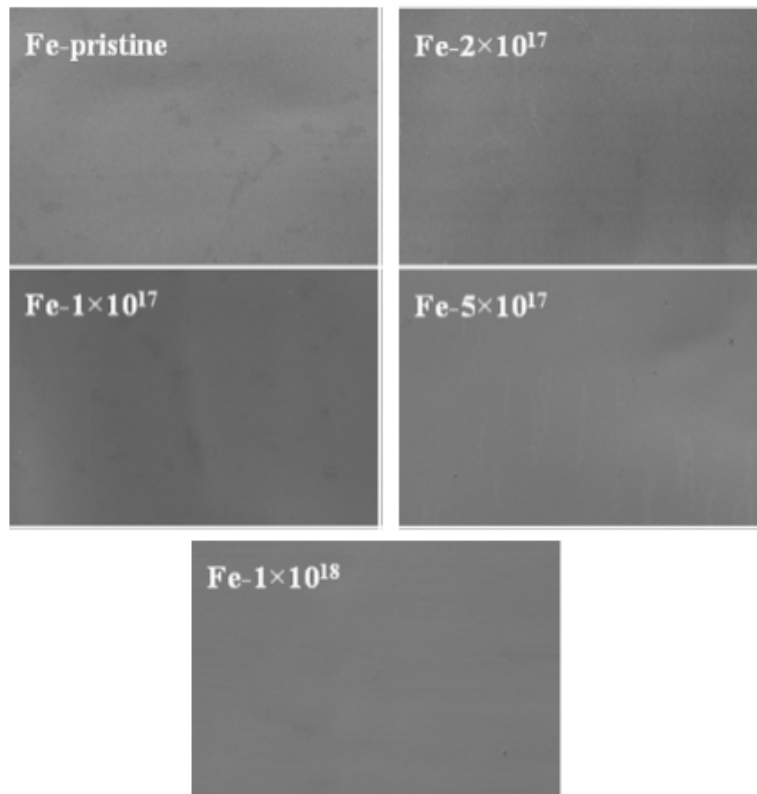


Figure 2.20: SEM images of FeSiB metallic glass before and after the 250 keV H^+ ion irradiation. Images for four different fluences and as-cast metallic glass are seen [81].

Another example is the effect of 300 keV Ar^+ irradiation on ZrCuFeAl metallic glass [82]. In this example, XRD and thermal analysis are examined. The XRD pattern of this specimen is shown in Figure 2.21, where different colors represent various fluences. After the radiation, there is no obvious change in XRD patterns. The lack of a sharp peaks shows that crystalline structure did not form. However, the intensity of the broad peak became weaker and shifted a little left and the reason for this difference is small changes in microstructure such as point defects. Additionally, differential scanning calorimetry (DSC) was examined for thermal analysis. DSC curves of both unirradiated and irradiated samples are shown in Figure 2.22. Glass transition temperatures are seen from the curves (T_g). DSC curves show that the glass transition temperature declined as the fluence increased. After the irradiation, supercooled liquid region is extended and it can be deduced that Ar^+ irradiation is forceful enough to

broaden the supercooled liquid region (ΔT_x). The possible reason for that is the point defects like vacancy and interstitial because these defects can cause small differences in the DSC curves.

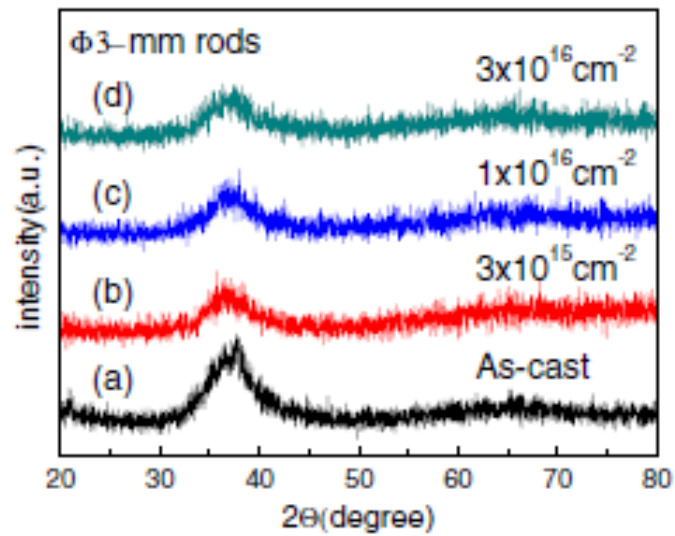


Figure 2.21: XRD patterns of ZrCuFeAl metallic glass before and after 300 keV Ar^+ ion irradiation. Metallic glass was irradiated with four different fluences and these were compared with the as-cast sample [82].

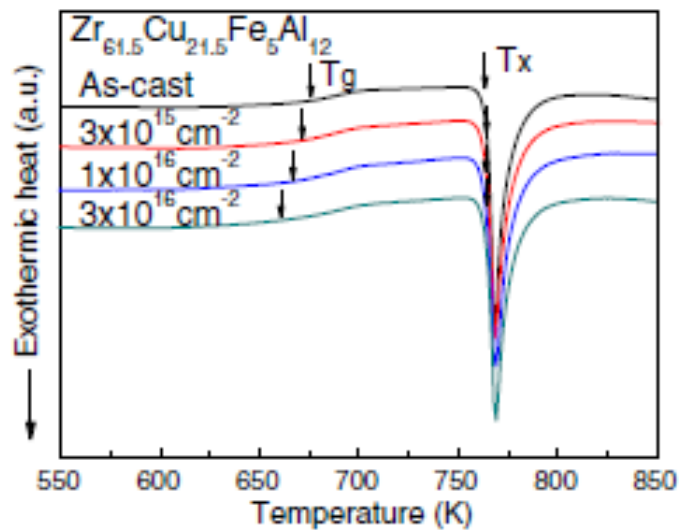


Figure 2.22: DSC curves of ZrCuFeAl metallic glass before and after the 300 keV Ar^+ ion irradiation. T_g is the glass transition and T_x is the first crystallization onset temperature [82].

Another example is the $\text{Ni}_{62}\text{Ta}_{38}$ metallic glass under He^{+2} ion irradiation with 300 keV [83]. Phase structure and microstructural analysis are given for this study. In Figure 2.23, XRD patterns of metallic glass are shown. Metallic glass was irradiated with four different fluences. Before the irradiation, it shows amorphous structure because it has one broad peak. After the irradiation, no clear peak exists that shows crystalline structure and so, specimens still have amorphous structure. In Figure 2.24, SEM images of $\text{Ni}_{62}\text{Ta}_{38}$ metallic glass are shown for different fluences. Before the irradiation, the surface morphology of $\text{Ni}_{62}\text{Ta}_{38}$ was flat due to the amorphous structure as expected. When the fluence is less than 1.0×10^{18} ion/cm², it shows still amorphous structure. However, when fluence reaches 1.6×10^{18} ion/cm², some damage like incrustation and delamination occurred due to 300 keV He^{+2} ion irradiation.

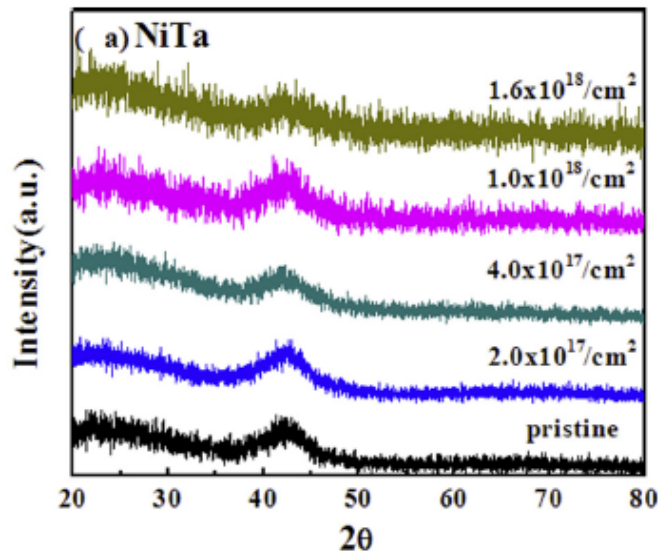


Figure 2.23: XRD patterns of $\text{Ni}_{62}\text{Ta}_{38}$ metallic glass before and after 300 keV He^{+2} ion irradiation. Different colors represent the various fluences [83].

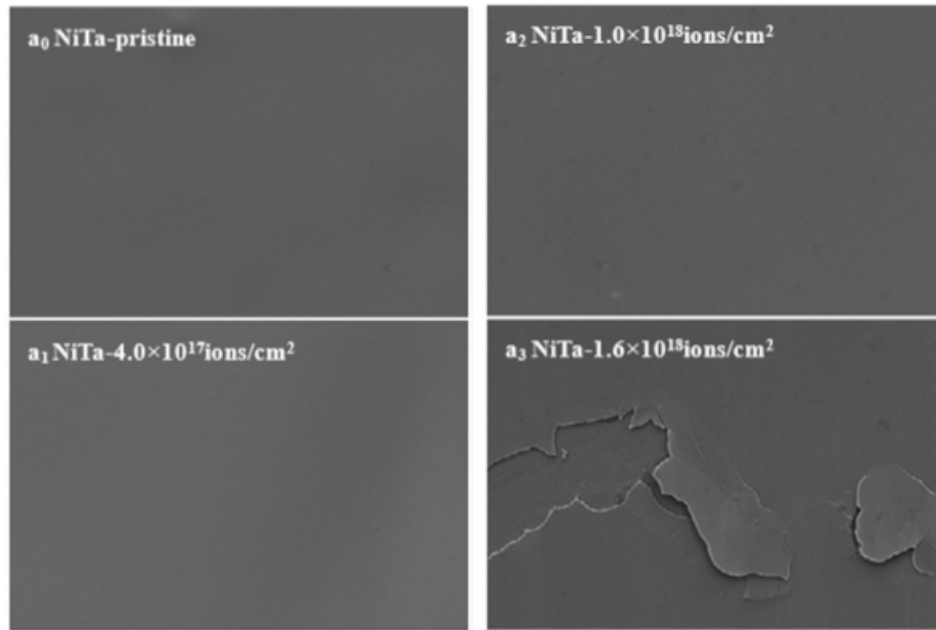


Figure 2.24: SEM images of $\text{Ni}_{62}\text{Ta}_{38}$ metallic glass before and after 300 keV He^{+2} ion irradiation. Metallic glass was irradiated with four different fluences [83].

Another example is H^+ ion induced irradiation damage of Fe and Ni based metallic glasses [73]. In Figure 2.25, XRD patterns of Fe and Ni based metallic glasses under 40 keV H^+ ion irradiation are shown. Before the irradiation, both have amorphous structure because they have one broad peak. After the irradiation, Fe-based metallic glass exhibit a crystalline diffraction peak which indicates the formation of crystallization. However, Ni-based metallic glass remained amorphous during the irradiation, since no crystal peak was not observed. In Figure 2.26, hysteresis loops of the same Fe-based metallic glass is seen before and after the irradiation. As-cast metallic glass has soft magnetic properties such as low coercivity, high permeability, high saturation magnetization. When the fluence reaches 3×10^{18} ions/cm², the coercivity increases lightly which implies that there are small structural changes in the sample such as point defects. Saturation magnetization can also be observed, but the change is not so important because it is so small. Specimen still exhibit soft magnetic properties even after the H^+ ion irradiation of 40 keV.

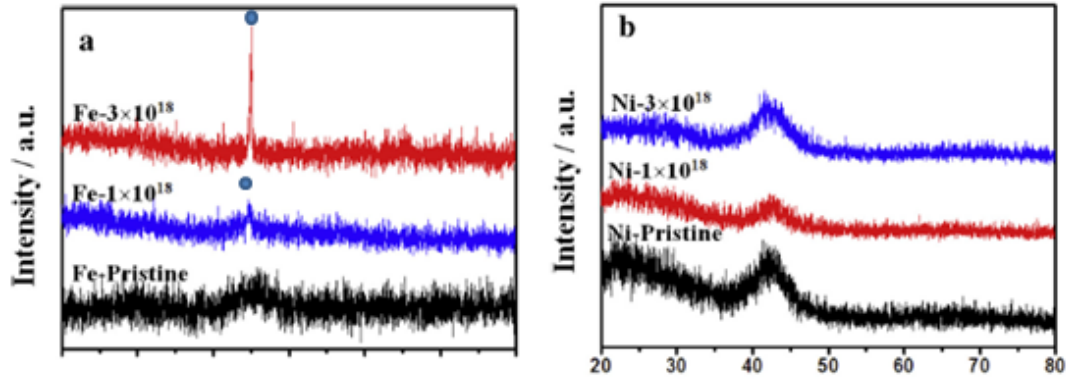


Figure 2.25: XRD patterns of Fe and Ni based metallic glasses before and after H^+ ion irradiation with 40 keV. As-cast and irradiated metallic glasses for both are seen [73].

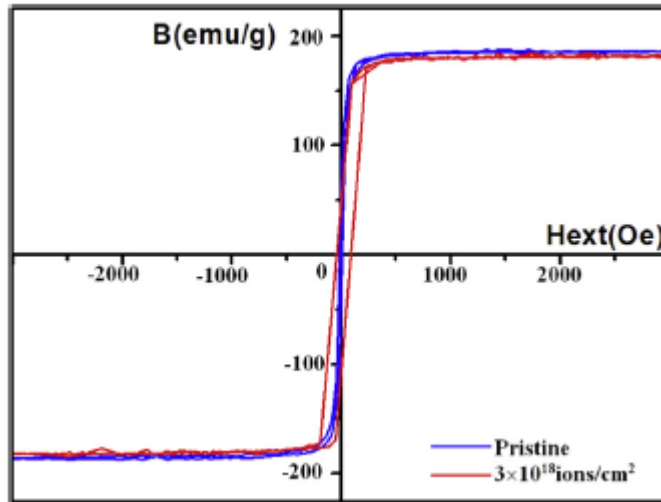


Figure 2.26: Hysteresis loops of Fe-based metallic glass before and after H^+ ion irradiation with 40 keV. As-cast and sample with 3×10^{18} ions/cm² fluence are given [73].

In general, the target atoms can leave their lattice sites under irradiation and this creates vacancy-like defects for BMGs [84]. The free volumes in the BMGs can be detected using positron annihilation spectroscopy. It is a persuasive technique to examine the point defects like vacancy-type defects in material and it is a non-destructive characterization technique [85, 86]. This technique is used in radiation

damage studies frequently and an example of such a study using positron annihilation spectroscopy is shown in Table 2.4 [87]. The lifetime of a positron is increased after 180 keV He ion irradiation because the free volume like vacancies is increased in the metallic glass after the irradiation. The lifetime of the positron is related with the free volumes inside the material. In the case of high free volume solid, positron annihilation process became slower so, the lifetime increases.

Table 2.4: Positron lifetime of ZrCuAl bulk metallic glass before and after irradiation using 15 keV positrons for positron annihilation spectroscopy [87].

Samples	Total dose(/cm ²)	Positron lifetime difference (ps)
As-cast	-	191
180 keV He ion	1×10^{16}	+23
2.5 MeV Xe ion	1×10^{14}	-3

Various characterization techniques can be used in order to analyze irradiated materials. As seen from the literature, the effects of irradiation are not observed in each analysis. Therefore, all achievable analyses should be performed for a complete study. All these techniques mentioned here has been used in this thesis to give a complete picture of the radiation damage on purpose-made BMGs which were irradiated with 30 MeV protons.

CHAPTER 3

RADIATION TESTS OF STAINLESS STEEL AND BULK METALLIC GLASS SAMPLES WITH PROTONS AND CHARACTERIZATION RESULTS

In this section, first production of BMGs at METU Metallurgical and Materials Engineering Department and the radiation tests of SS and BMG samples at METU-DBL will be presented. Later, characterization techniques and the comparative results using these techniques will be given.

3.1 Raw Materials

Two types of bulk metallic glasses were produced to be studied under radiation. These alloys are $M_{60}Cr_{13}Mo_{10}B_8Y_2Mn_7$ and $Fe_{36}Co_{36}B_{19.2}Si_{4.8}Nb_4$. For the first alloy, a cast iron piece was used as a component and it is denoted with an "M". The composition of the cast iron is shown in Table 3.1. Scrap cast iron includes many elements in addition to iron. Cast iron was alloyed with other pure elements to produce the alloy. Highly pure elements are used in the alloys and the purity grades of these elements are indicated in Table 3.2.

Table 3.1: The chemical composition of scrap cast iron with weight percentages.

Element	wt%	Element	wt%	Element	wt%
Fe	92.770	Co	0.016	Ti	0.016
C	4.330	As	0.005	V	0.016
Si	2.090	Zn	0.005	B	0.001
Mn	0.400	Zr	0.004	Ca	0.002
Cu	0.210	Mo	0.004	Sn	0.003
Ni	0.090	Pb	0.003	Al	0.003
Cr	0.060	S	0.059	P	0.050

Table 3.2: The alloying elements with their purity grades. These elements were used for the production of the two types of alloys.

Alloying Elements			
Element	Grade	Element	Grade
Mo	99.95 %	Fe	99.97 %
Y	99.90 %	Co	99.90 %
Mn	99.90 %	Nb	99.60 %
B	99.50 %	B	99.50 %
Cr	99.20 %	Si	98.50 %

All elements were supplied from Alfa Aesar except for manganese from Roketsan. The chemical composition of the bulk metallic glasses are very critical so, they were weighted carefully by using precision scale and prepared for casting.

3.2 Production of BMGs

The production of the specimens were performed by using arc melting and copper mold suction casting on January 29, 2018. Heating is supplied between electric arc struck and tungsten electrode. Elements are melted in the pot using the supplied heat and repetition of the melting process is applied to avoid heterogeneity. In order to prevent oxidation, melting process takes place in argon atmosphere due to it being an

inert gas. 15 gr batches can be prepared in a small crucible. To keep the chamber under vacuum, rotary and diffusion pump are used and the vacuum level is kept at 10^{-6} mbar. Copper mold suction casting is used to suck the alloy and this fast movement leads to rapid solidification. Diameter of the copper mold is 3 mm. In Figure 3.1, the arc melting apparatus is shown with different magnifications [57].

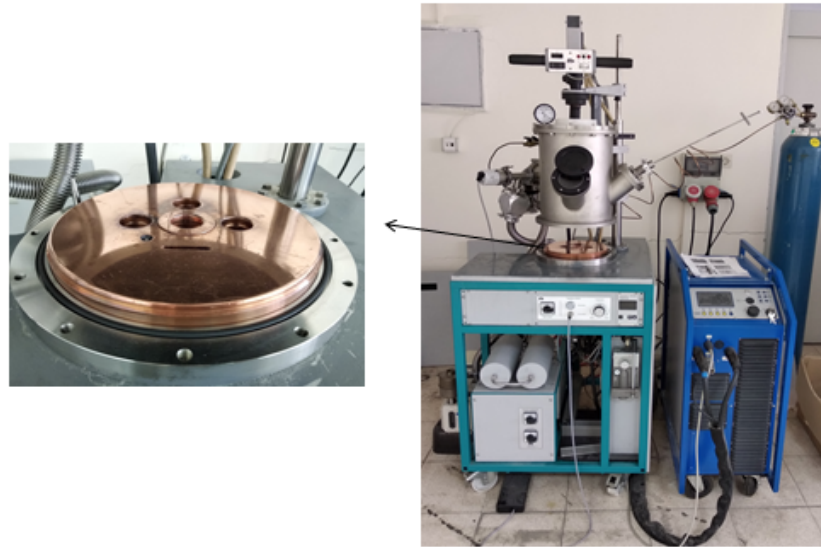


Figure 3.1: Edmund Buhler arc melting apparatus. BMGs were produced by using arc melting and copper mold suction casting.

For $M_{60}Cr_{13}Mo_{10}B_8Y_2Mn_7$, elements were put into the crucible and they were melted together several times to be homogeneous. For $Fe_{36}Co_{36}B_{19.2}Si_{4.2}Nb_4$, elements were melted together and this process were repeated many times to ensure the homogeneity. After the melting processes, molten alloy was sucked into the water-cooled copper mold. As a result, $M_{60}Cr_{13}Mo_{10}B_8Y_2Mn_7$ sample obtained a 3 mm radius and approximately a 10 cm length. $Fe_{36}Co_{36}B_{19.2}Si_{4.2}Nb_4$ also acquired a 3 mm radius and approximately a 10 cm length. These samples are very brittle due to their high hardness so the cutting process was very demanding. Therefore, a wire erosion machine, which is located in Welding Technology and Non-Destructive Testing Center, was used for cutting while preventing damage to the samples. Some examples of the cut samples are shown in Figure 3.2.



Figure 3.2: Some examples of the produced and cut samples. They were cut by the help of a wire erosion machine due to their brittleness.

3.3 Radiation Testing of Materials

Two types of Fe-based alloys were produced in order to examine the effects of radiation on these materials. Also, AISI 304 and 316 stainless steel [88] were chosen for the possible comparison of amorphous and crystalline materials. A holder was designed to clasp the samples during the irradiation because of their small size (3 mm radius) and also of the high number of samples. Designed holder is shown in Figure 3.3. Samples were irradiated from the front. These samples were examined from two sides in some analyses: front and lateral sides. Thus, penetration depth of particles on materials were investigated in the lateral side analysis.

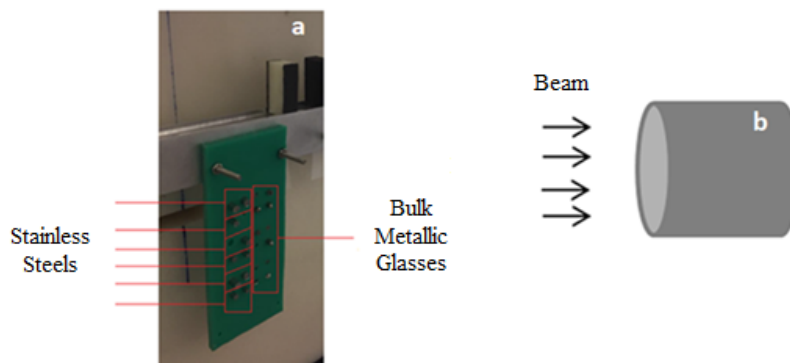


Figure 3.3: a) The designed holder for the samples during irradiation. Stainless steels (on left) and bulk metallic glasses (on right) were placed in holder. b) The direction of the beam. The beam hits the sample from the front.

These materials were irradiated by three different fluences changing the irradiation time. While the first row was irradiated for 10 minutes, the second row and the third row were irradiated for 20 and 30 minutes respectively. Irradiation date was February 28, 2018. Fluences for each material are shown in Table 3.3. This measurements were performed by using a diamond detector. Secondary dose during the irradiation were very low. Gamma dose was 1.0 ± 0.1 mSv and neutron dose was 4.2 ± 0.4 mSv.

Table 3.3: Samples and their fluences in accordance with their different exposures.

Fluence (p/cm ²) (BMGs)	Fluence (p/cm ²) (SSs)
3.3×10^{12}	4.1×10^{12}
7.2×10^{12}	7.8×10^{12}
1.3×10^{13}	1.0×10^{13}

3.4 Characterization Techniques

In this study, various characterization techniques were used to analyze the effects of radiation on materials. Materials were examined in terms of microstructure, thermal, magnetic and mechanical characteristics. First, all samples were embedded vertically and examined from the top view as shown in Figure 3.4 (left). Second, highest fluence samples were embedded horizontally and examined from the side view as indicated in Figure 3.4 (right). Examined surfaces are shown with blue arrows.

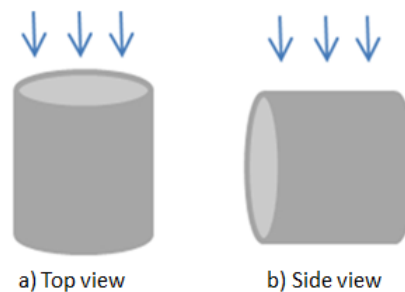


Figure 3.4: Schematic illustrations of the examined surfaces from the top and side view of all samples. The examined surfaces are shown with blue arrows.

3.4.1 X-ray Diffractometer

XRD analyses were employed in order to determine phases inside the specimens. Bruker S8 Tiger Diffractometer device was used and it was supplied from Department of Metallurgical and Materials Engineering. In this analysis, monochromatic Cu-K α was used and the diffraction was angle 2θ with the range of 30-120°. 0.1°/min was chosen as a scanning rate.

3.4.2 Optic Microscope

Huvtz brand optic microscope was used before the SEM analysis for the microstructure characterization. This microscope was supplied by Department of Metallurgical and Materials Engineering.

3.4.3 Scanning Electron Microscope

FESEM/FEI NOVA NANO430 scanning electron microscope was used for the detailed microstructure analysis. This analysis also contains energy dispersive spectroscopy (EDS). It was carried out for the chemical microanalysis [89]. For the preparation of SEM specimens, samples were first embedded in bakelite and then they were ground and polished. After the polish process, they were etched. Bulk metallic glasses were etched with nital which is a solution of nitric acid and alcohol, commonly used as a metal etchant. 304 and 316 Stainless steels were etched with aqua regia that is a composition of hydrochloric acid and nitric acid, which has a molar ratio of 3:1. After that SEM analysis was performed for all samples.

3.4.4 Differential Scanning Calorimetry

Thermal analysis was conducted by Differential Scanning Calorimeter (DSC) with Setaram Setsys 16/18 device. The purpose of this analysis to determine some phase transformation temperatures such as glass transition temperature (T_g), crystallization temperature (T_x) and melting temperature (T_m). Heating and cooling rate are 40°/min

in the range of 303-1723 K. Samples were prepared to weigh between 15 and 20 mg. The photographs of DSC apparatus are shown in Figure 3.5.

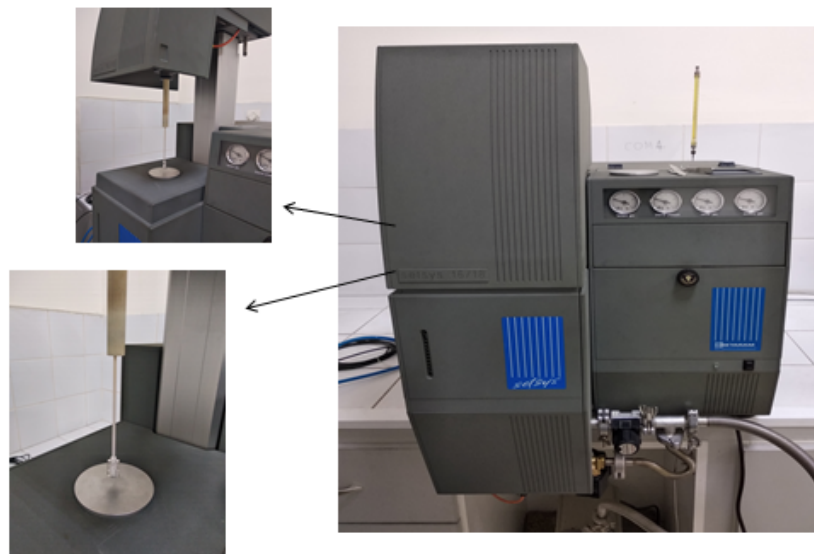


Figure 3.5: Setaram Setsys 16/18 branded differential scanning calorimetry apparatus. Thermal analyses were performed using this device.

3.4.5 Vibrating Sample Magnetometry

Magnetic properties of the samples were examined by using ADE Magnetics EV/9 Vibrating Sample Magnetometer (VSM). Samples were prepared to weigh between 30 and 50 mg. Saturation magnetization and coercivity of the samples were found using this analysis. The photographs of the VSM apparatus are shown in Figure 3.6.

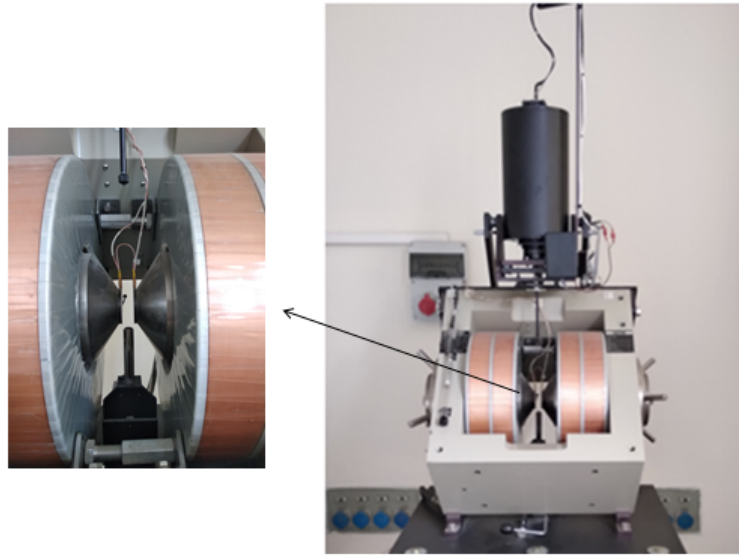


Figure 3.6: ADE Magnetics EV/9 vibrating sample magnetometer apparatus. Magnetic properties of the samples were found using this device.

3.4.6 Microhardness Test

Vickers microhardness measurements were conducted by Shimadzu-2 microhardness tester. Microhardness tests were performed for all samples to see the effects of the radiation on mechanical properties of samples. The direction of the recorded hardness values is given in Figure 3.7. The red lines indicate the points where hardness values were recorded. These microhardness analyses were performed for all samples in the same manner.

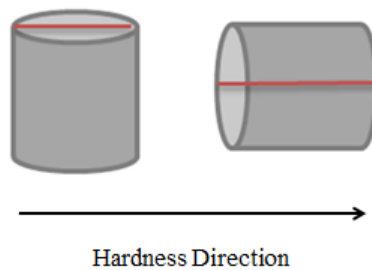


Figure 3.7: The direction of the microhardness analyses is given. The red lines indicate the points where the hardness values were recorded.

3.4.7 Positron Annihilation Lifetime Spectroscopy

The operating principle of the positron annihilation lifetime spectroscopy (PALS) is simple. The typical setup of a positron annihilation spectrometer includes ^{22}Na sandwiched between two thin Kapton foils as a positron source and two or more scintillator detectors [90]. The elapsed time between emission of positrons from the source and detection of gamma rays gives the lifetime of positron. If positrons penetrate through solid with little to no emptiness, they interact with free electrons and annihilates rapidly. However, when positrons are injected in a solid with voids, they annihilate more slowly [91]. This technique is commonly used to analyze the free volumes in BMGs before and after irradiation. The other detectors are used to detect the gamma rays which were produced by annihilating of positrons.

PALS was used to study the defects in some materials. As a positron source ^{22}Na is used. This analysis was performed at Marmara University [92] and the image of spectroscopy apparatus is given in Figure 3.8.



Figure 3.8: The positron annihilation lifetime spectroscopy apparatus. Defects inside the materials were examined with this spectroscopy [92].

3.4.8 Stopping and Range of Ions In Matter (SRIM) Simulations

This program was used to examine the effects of radiation on materials. The penetration depth of protons and the stopping power of the materials under radiation exposure were analyzed. Simulation studies were performed and also characteriza-

tion techniques were applied to specimens in order to examine the effects of radiation on materials. The results of characterization studies were interpreted by deducing the simulation output. These studies will be presented later in this Chapter.

3.5 SRIM Simulations of Irradiated Materials

SRIM which is a Monte Carlo simulation code was used to find out the stopping power of materials under radiation exposure and the range of particles in materials. This software also includes a package called TRIM (Transport of Ions In Matter) for the detailed analysis [93]. The range of protons inside the materials and vacancy formation were studied.

In SRIM, all materials were defined according to their chemical composition. Elements and their atomic percentages were used to define the materials in the program. The chemical compositions of the 304 and 316 stainless steel with their atomic and weight percentages were given in Table 3.4.

Table 3.4: Chemical compositions of 304 and 316 SS. The major differences are molybdenum and the amount of the chromium and nickel [94] [95].

Element	304 SS (wt%)	304 SS (at%)	316 SS (wt%)	316 SS (at%)
Carbon	0.08 max.	0.36	0.08 max.	0.37
Manganese	2.00 max.	1.99	2.00 max.	2.02
Phosphorous	0.045 max.	0.08	0.045 max.	0.08
Sulfur	0.03 max.	0.05	0.03 max.	0.05
Silicon	0.75 max.	1.46	0.75 max.	1.48
Chromium	18.00 - 20.00	20.98	16.00 - 18.00	19.17
Nickel	8.00 - 10.50	9.76	10.00 - 14.00	13.21
Molybdenum	-	-	2.00 - 3.00	1.73
Nitrogen	0.10 max.	0.39	0.10 max.	0.40
Iron	Balance	64.94	Balance	61.49

All materials were simulated as being irradiated with 30 MeV hydrogen ions, because

SRIM program only includes ion sources. Hydrogen atom has one proton and one electron so when it loses or gains an electron, it creates a hydrogen ion and a positively charged hydrogen ion which represents a proton. The electronic and nuclear energy losses of materials that are found from SRIM program are shown in Table 3.5.

Table 3.5: Nuclear and electronic energy losses of 30 MeV protons in different materials. Electronic energy loss is higher than nuclear energy loss.

Electronic and Nuclear Energy Losses		
304 Stainless Steel	dE/dx (Electronic)	9.73 MeV/mm
	dE/dx (Nuclear)	4.23×10^{-3} MeV/mm
316 Stainless Steel	dE/dx (Electronic)	9.63 MeV/mm
	dE/dx (Nuclear)	4.18×10^{-3} MeV/mm
$\text{Fe}_{36}\text{Co}_{36}\text{B}_{19.2}\text{Si}_{4.8}\text{Nb}_4$	dE/dx (Electronic)	8.61 MeV/mm
	dE/dx (Nuclear)	3.71×10^{-3} MeV/mm
$\text{M}_{60}\text{Cr}_{13}\text{Mo}_{10}\text{B}_8\text{Y}_2\text{Mn}_7$	dE/dx (Electronic)	9.11 MeV/mm
	dE/dx (Nuclear)	3.91×10^{-3} MeV/mm

Energy losses are calculated in SRIM by using the Bethe-Bloch formula. As mentioned in Section 2.2.1, at low energies, the nuclear stopping dominate while electronic stopping dominate at high energies.

SRIM calculates the energy loss and range of ions in material using a quantum mechanical treatment of ion-atom collision. Also the detailed analyses for materials were carried out by using TRIM. The energy loss of ions throughout the depth of the material and their ranges are indicated in Figure 3.9. These plots are called as Bragg curves as mentioned before in Section 2.2. The energy loss of protons inside the materials are seen. Plots have peaks at the end of the penetration depth because energy loss is inversely proportional with the energy of charged particle. While, the range of protons in $\text{Fe}_{36}\text{Co}_{36}\text{B}_{19.2}\text{Si}_{4.8}\text{Nb}_4$ and $\text{M}_{60}\text{Cr}_{13}\text{Mo}_{10}\text{B}_8\text{Y}_2\text{Mn}_7$ is approximately 2 mm, it is roughly 1.75 mm for stainless steels.

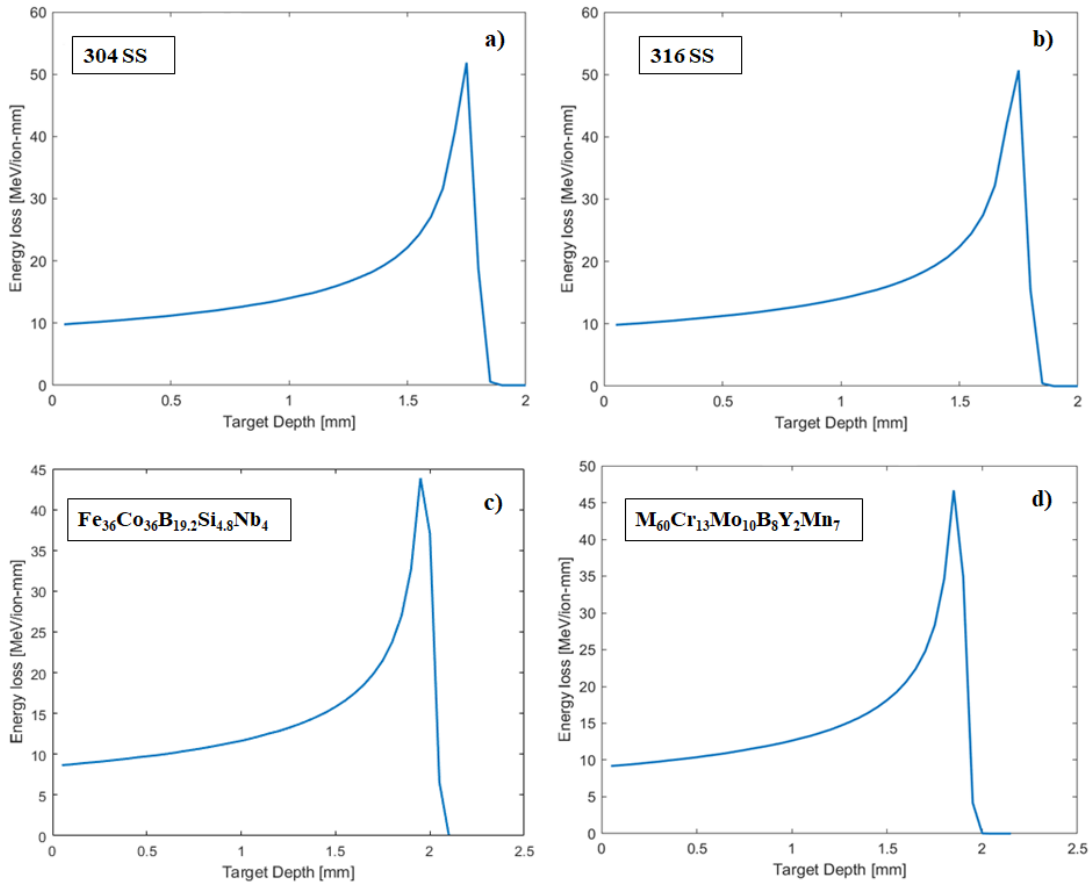


Figure 3.9: Energy losses of protons in a) 304 stainless steel, b) 316 stainless steel, c) $\text{Fe}_{36}\text{Co}_{36}\text{B}_{19.2}\text{Si}_{4.8}\text{Nb}_4$, d) $\text{M}_{60}\text{Cr}_{13}\text{Mo}_{10}\text{B}_8\text{Y}_2\text{Mn}_7$ versus target depth. While the range of protons in stainless steels is approximately 1.75 mm, the range of protons in BMGs is approximately 2.00 mm.

Some definitions are important before looking further into analyses. When an energetic incident atom collides with a lattice atom, the lattice atom leaves its original position. This is called the displacement of an atom. The empty lattice site that is created as a result of the displacement of the atom is named a vacancy and atoms that were knocked out of their original lattice sites stop in the solid because of interstitials in the crystal. Furthermore, some critical energies must be defined. The minimum energy necessary to replace the position of the target atom permanently is called the threshold displacement energy and as a result of this a Frenkel pair (vacancy and adjacent interstitial atom) is formed which is the most common damage occurs due to ions. SRIM has many options for the type of damage calculation. "Detailed calcula-

tion with full damage cascades" option was selected because it provides all energies for all the knock-on atoms generated by the primary ions [97]. With this option, each recoiling atom is followed as far as the energy of the recoiling atom drops lower than the displacement energy of target atom. Accordingly, all damage cascade can be examined.

As mentioned before, the energy loss of ions to the target electrons is called as the electronic stopping power. After that, target atom which is primary knock on starts a recoil cascade with regarding to its recoil energy. When the moving atom hits a target atom, it transfers energy more than its displacement energy. The vacancies that can occur in materials as a result of radiation was studied in SRIM and the results are shown in Figure 3.10.

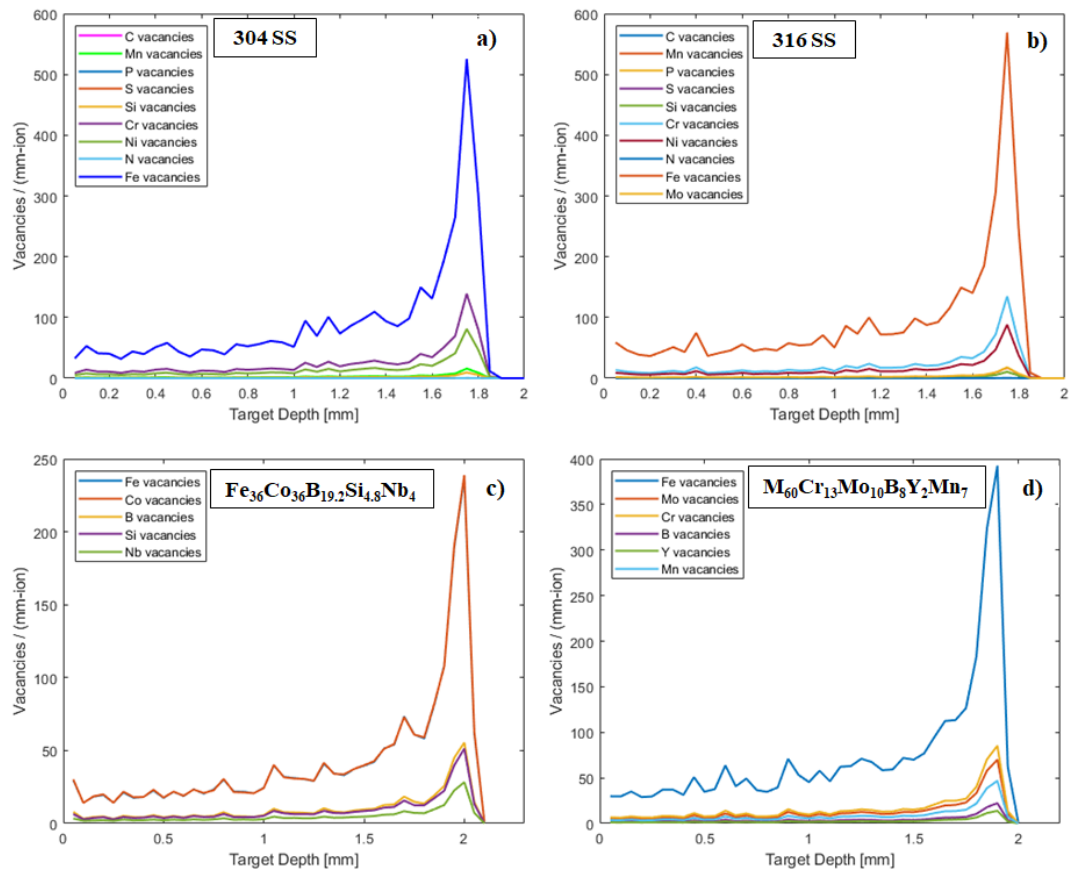


Figure 3.10: The vacancy formation of atoms in a) 304 stainless steel, b) 316 stainless steel, c) $\text{Fe}_{36}\text{Co}_{36}\text{B}_{19.2}\text{Si}_{4.8}\text{Nb}_4$, d) $\text{M}_{60}\text{Cr}_{13}\text{Mo}_{10}\text{B}_8\text{Y}_2\text{Mn}_7$ versus target depth. Colors represent lattice vacancies of different elements.

Threshold displacement energies are essential to interpret these plots and these energies are given in Table 3.6. Iron, nickel and chromium have a higher percentage than others in 304 SS and the contribution of other elements are low so their vacant atoms are a few. Threshold displacement energies of iron, nickel and chromium are close to each other, so the number of vacant atoms are directly proportional to their contribution in alloy.

316 SS is similar to 304 SS in composition, so their results are also similar. The only difference is molybdenum. Iron, nickel and chromium result in a higher number of vacant atoms than the other elements. While molybdenum has the highest, manganese has the lowest minimum displacement energy for $M_{60}Cr_{13}Mo_{10}B_8Y_2Mn_7$. According to the composition, there is more boron than manganese in the alloy and therefore more vacancies should result from manganese. However, manganese vacancies are higher than the boron vacancies because the minimum displacement energy of boron is higher than manganese. Theoretic information and SRIM results are compatible with each other. Niobium has the highest and cobalt has the lowest minimum displacement energy for $Fe_{36}Co_{36}B_{19.2}Si_{4.8}Nb_4$. Iron and cobalt have the same percentage in alloy and also their minimum displacement energies are very close. Therefore, their vacancies should also be equal and iron and cobalt overlap in the plot.

Table 3.6: Threshold displacement energies of elements contained in alloys [98].

Elements	E_d (eV)	Elements	E_d (eV)
C	69	Ni	33
Mn	33	N	40
P	20	Fe	40
S	20	Mo	65
Si	37	B	46
Cr	40	Y	36
Co	36	Nb	78

3.6 Effects of irradiation on the microstructure and properties of the materials

3.6.1 Effects of irradiation on 304 and 316 Stainless Steels

SEM analysis was carried out for the 304 and 316 SS as-received, at fluences of 4.1×10^{12} p/cm², 7.8×10^{12} p/cm² and 1.0×10^{13} p/cm² to perform microstructural characterization and to examine surface morphology changes after the irradiation. As mentioned Section 3.4, samples were examined from two different views in SEM analysis. First, the top view images for all samples of 304 SS and 316 SS are shown in Figure 3.11 and Figure 3.12 respectively.

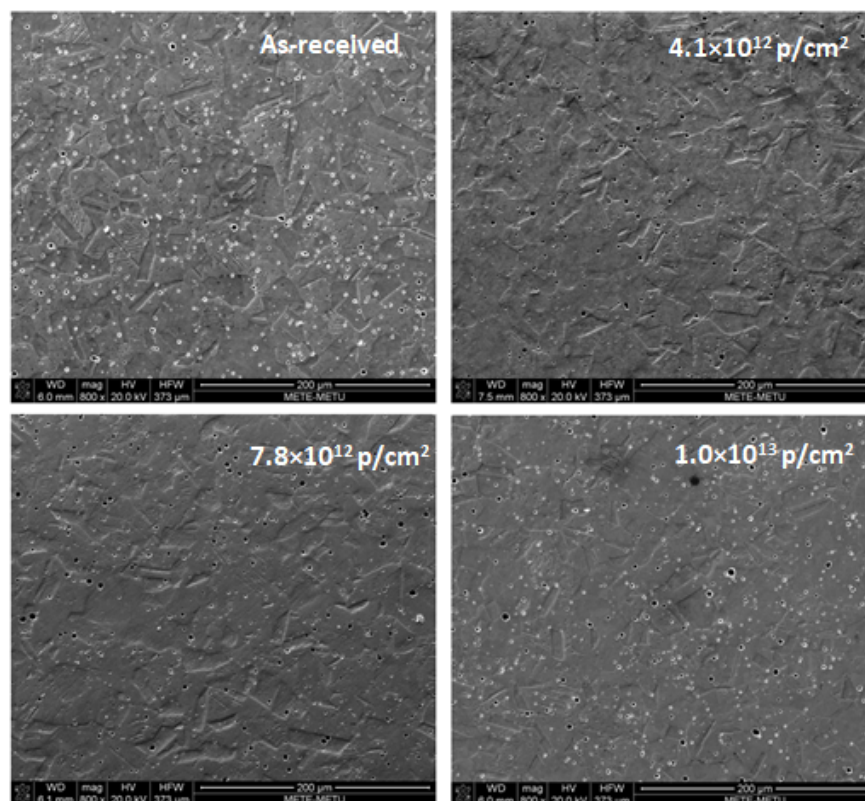


Figure 3.11: SEM images of 304 SS samples from the top view (central part). 304 SS as-received, at fluences of 4.1×10^{12} p/cm², 7.8×10^{12} p/cm² and 1.0×10^{13} p/cm² samples are given.

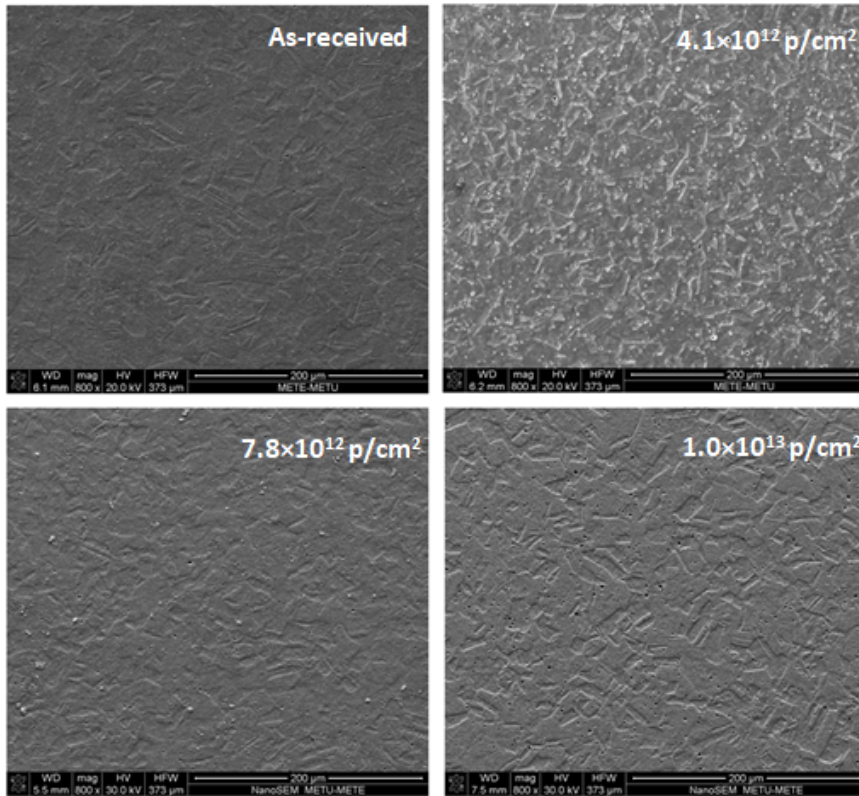


Figure 3.12: SEM images of 316 SS samples from the top view (central part). 316 SS as-received, at fluences of 4.1×10^{12} p/cm², 7.8×10^{12} p/cm² and 1.0×10^{13} p/cm² samples are given.

Secondly, 304 and 316 SS samples that have the highest fluence were examined from the side and they were analyzed along the penetration depth. In Figure 3.13, the regions for which SEM images were taken are indicated for the 304 SS (left) and 316 SS (right). Beam direction is indicated with a white arrow and SEM images were taken at three different points which are irradiated and unirradiated. Point 1 and point 2 represent approximately at a depth of 1 mm and 2 mm respectively while point 3 indicates a depth of roughly 8 mm. The SEM images of the 304 and 316 SS samples from the side view are given in Figure 3.14 and Figure 3.15 respectively.

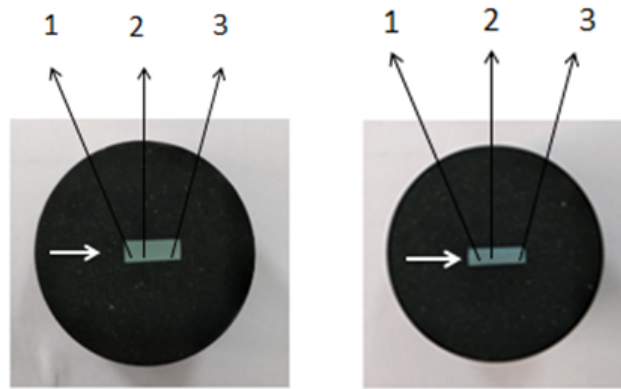


Figure 3.13: The regions at which SEM images were taken for the 304 SS (left) and 316 SS (right) samples. Beam direction is indicated with a white arrow and images were taken at three different points which are irradiated and unirradiated.

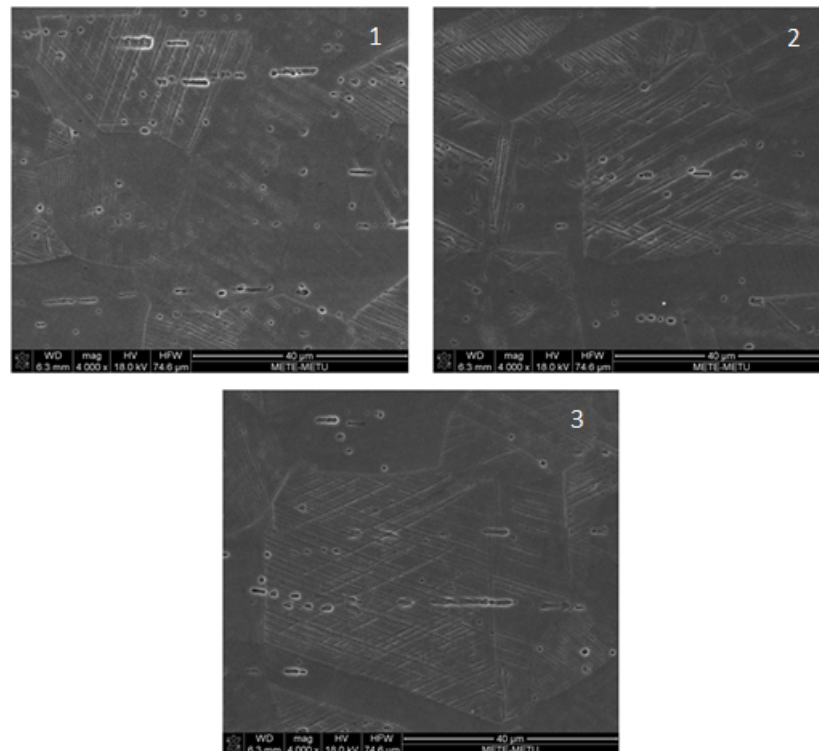


Figure 3.14: SEM images of the 304 SS sample from the side view. These images are shown for three different parts of the highest fluence sample which is 1.0×10^{13} p/cm².

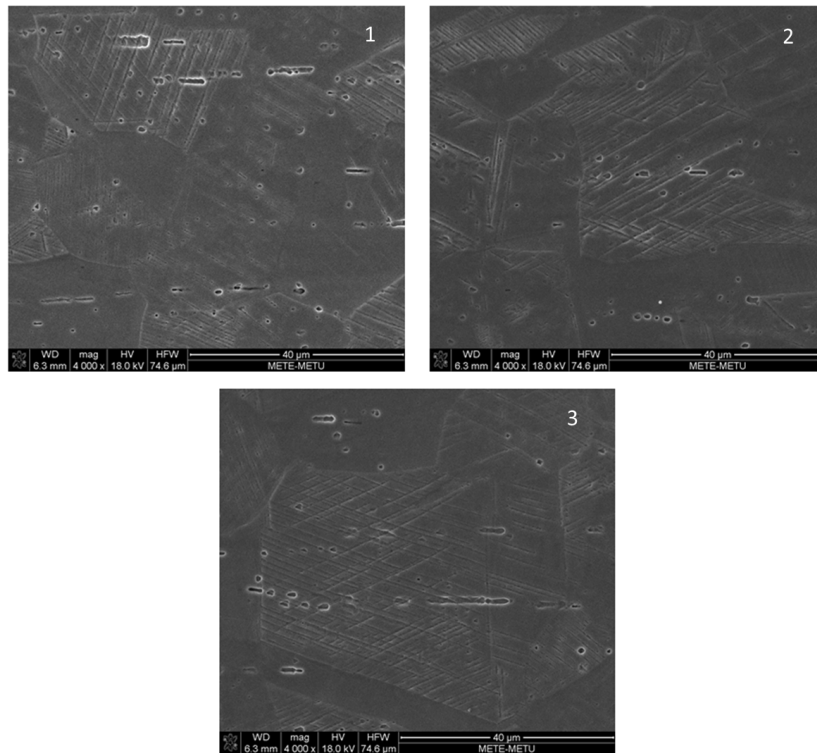


Figure 3.15: SEM images of the 316 SS sample from the side view. These images are shown for three different parts of the highest fluence sample which is 1.0×10^{13} p/cm².

In the SEM analyses, no surface damage such as delamination, exfoliation, blistering or cracking was observed after irradiation. Higher fluences than that was given here might induce such surface damage. Some black holes and dots formed on the surface of the samples are due to the etchant. Etching process of stainless steel is tougher than many alloys. Aqua regia was used as an etchant because it's powerful nature. Moreover, EDS analysis were performed and no new phase occurrence was observed on the samples in accordance with their compositions. As a result of these studies, no change was observed in the SEM analysis of irradiated samples. PALS was used to examine point defects in materials. This analysis was performed only for 316 SS and $\text{Fe}_{36}\text{Co}_{36}\text{B}_{19.2}\text{Si}_{4.8}\text{Nb}_4$ samples that received fluence of 1.0×10^{13} and 1.3×10^{13} p/cm² respectively and also for unirradiated samples as an example of each group. The result for the 316 SS sample is shown in here. The result of $\text{Fe}_{36}\text{Co}_{36}\text{B}_{19.2}\text{Si}_{4.8}\text{Nb}_4$ will be given in Section 3.6.3. PATHFIT program is used to analyze the spectrum for each sample and their results are given in Table 3.7.

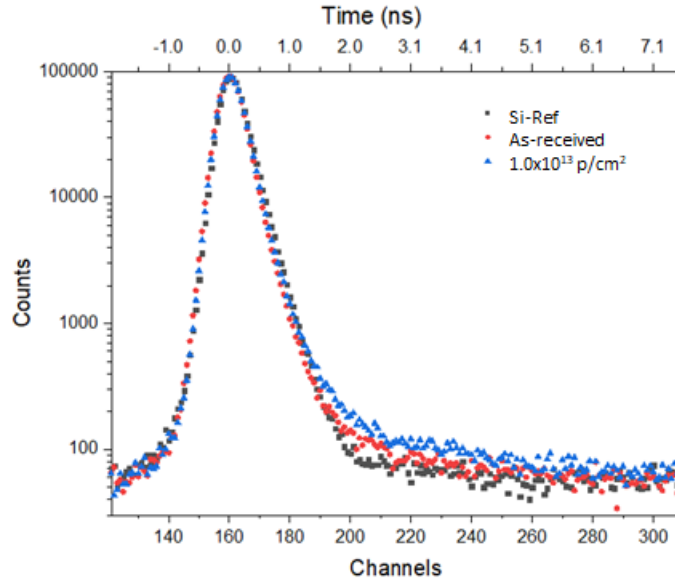


Figure 3.16: Positron annihilation lifetime spectroscopy for the 316 SS sample. This analysis was performed for unirradiated sample and sample which received a fluence of 1.0×10^{13} p/cm² samples.

Table 3.7: The analysis of positron annihilation lifetime spectroscopy. The lifetime of positrons for as-received and as-irradiated samples are given.

Protons received on the sample	$\tau \pm \Delta\tau$ (ns)	$I \pm \Delta I$ (%)
0 (As-received)	1.35 ± 0.06	1.17 ± 0.05
As-irradiated	1.37 ± 0.04	2.07 ± 0.05

The lifetime of positron for as-received and as-irradiated samples are given in Table 3.7. After irradiation, the lifetime of positrons increased and this shows that the number of point defects inside the material also increased. As the size of the defect increases, the average lifetime of the positron as, τ_2 , is also expected to increase because the lifetime is related with the defect size. On the other hand, the intensity of the lifetime is related with the number of such defects. As the intensity I_2 increases, the number of defects is expected to increase. The intensity has increased as expected and it shows the number of vacancies increased inside the material.

XRD analyses were made to find out the phases of samples before and after irradiation. XRD patterns of 304 and 316 SS samples are given in Figure 3.17 and 3.18 respectively.

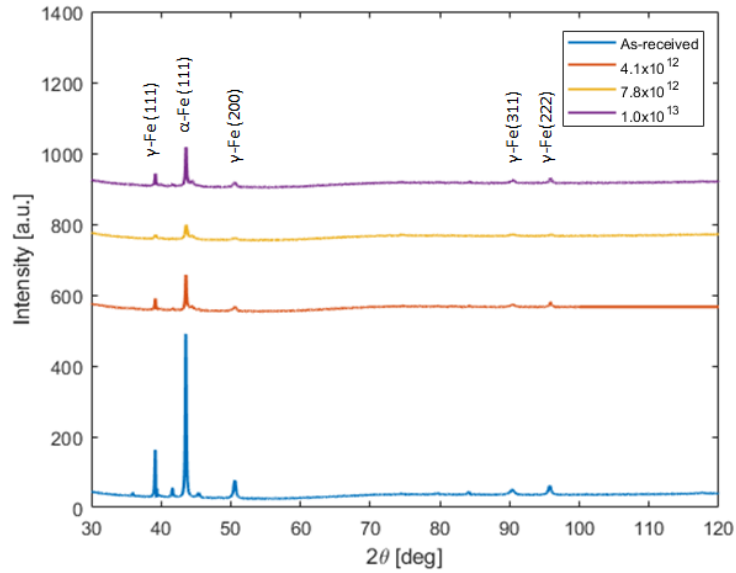


Figure 3.17: XRD patterns of 304 SS samples before and after irradiation. Different colors represent the as-received and as-irradiated samples.

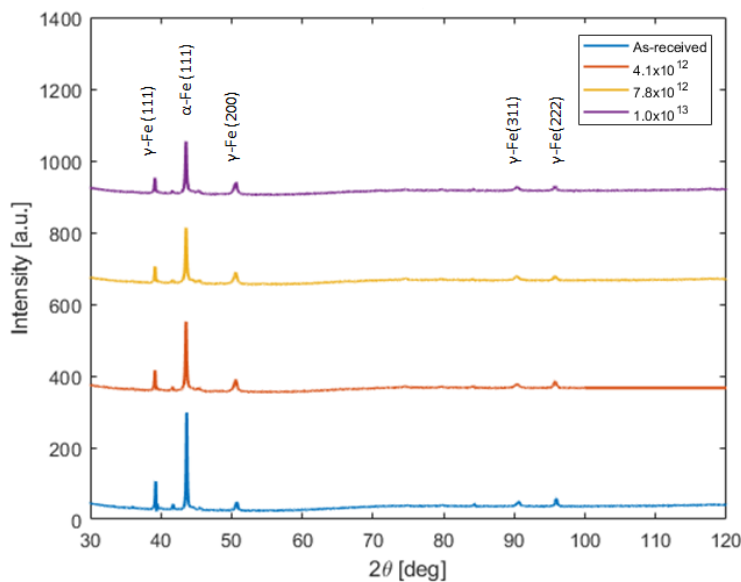


Figure 3.18: XRD patterns of 316 SS samples before and after irradiation. Different colors represent the as-received and as-irradiated samples.

In the XRD patterns, all possible phases for all observed in the samples are written. After irradiation, no phase formation was observed in the samples and this is compatible with EDS results. However, the intensity of peaks above each sample's baseline changed after irradiation. Point defects can cause this kind effect in the XRD patterns. Radiation leads to displacement damage in the crystal and so Frenkel pairs (vacancy+interstitial) can form. These kind of defects might induce lattice distortions and cause differences in the intensity of peak of the samples [99].

Additionally, thermal properties of the samples were studied to determine the phase transformation temperatures. For these analyses, 15-30 mg samples were cut from the samples. DSC curves of 304 and 316 SS samples are shown in Figure 3.19 and 3.20 for as-received and highest fluence samples which are 1.0×10^{13} p/cm². After irradiation, $T_{\gamma+\alpha-\alpha}$ decreased on the heating path. $T_{\gamma-\alpha+\gamma}$ increased after irradiation for the 304 SS sample. For 316 SS, after irradiation, $T_{\gamma-\alpha+\gamma}$ increased on the heating path. $T_{\alpha+\gamma-\alpha}$ and T_m decreased after irradiation. Transformation temperatures of the samples changed a little after the irradiation. A possible reason is the formation of point defects such as vacancies and interstitials [100] which can cause these small differences. The other reason can be experimental errors because the difference is few.

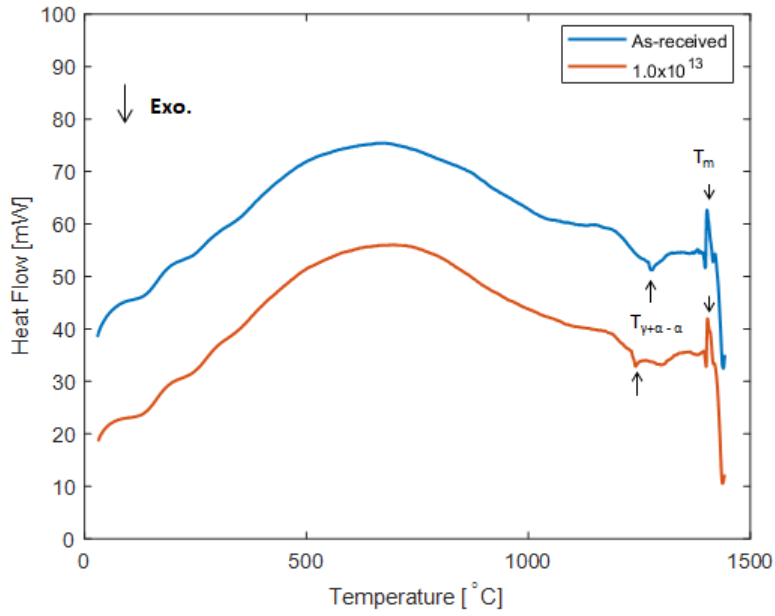


Figure 3.19: DSC curves of 304 SS for the as-received sample and a sample which received a fluence of 1.0×10^{13} p/cm².

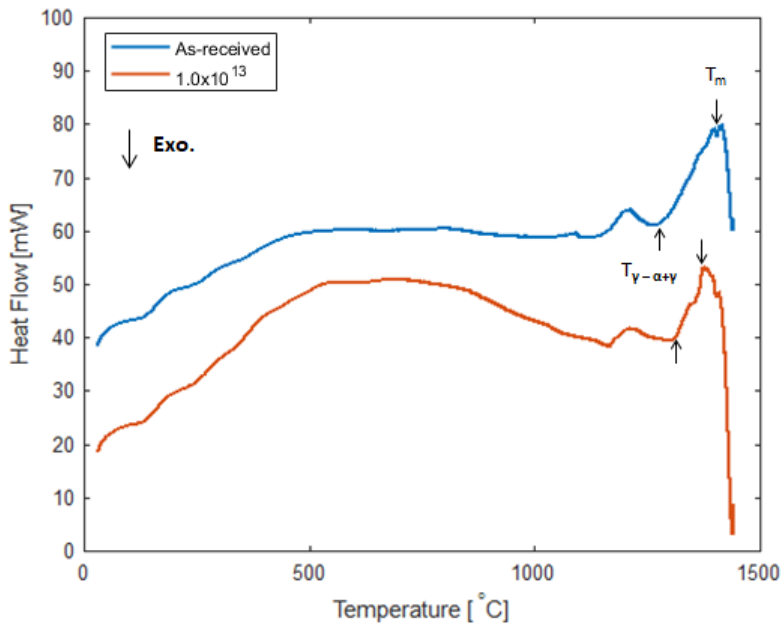


Figure 3.20: DSC curves of 316 SS for the as-received sample and a sample which received a fluence of 1.0×10^{13} p/cm².

Microhardness analyses of 304 and 316 SS from the top view for all samples were performed to examine the hardness properties. The results were given in Figure 3.21 and Figure 3.22.

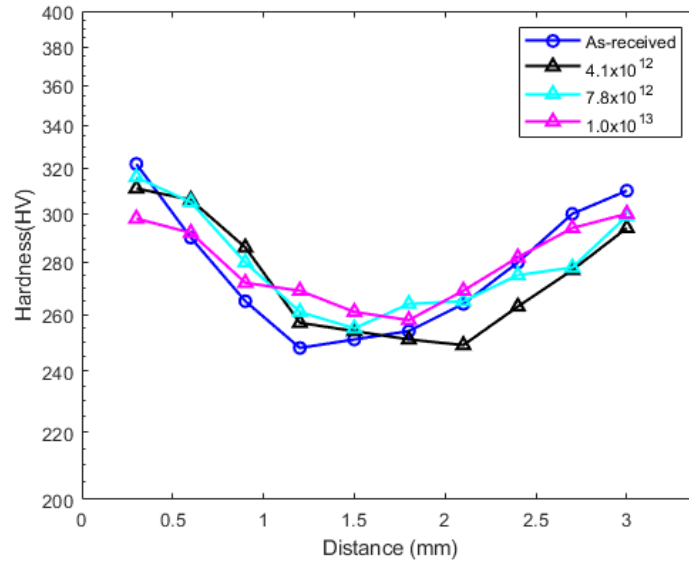


Figure 3.21: Microhardness analysis of the 304 SS samples before and after irradiation (top view).

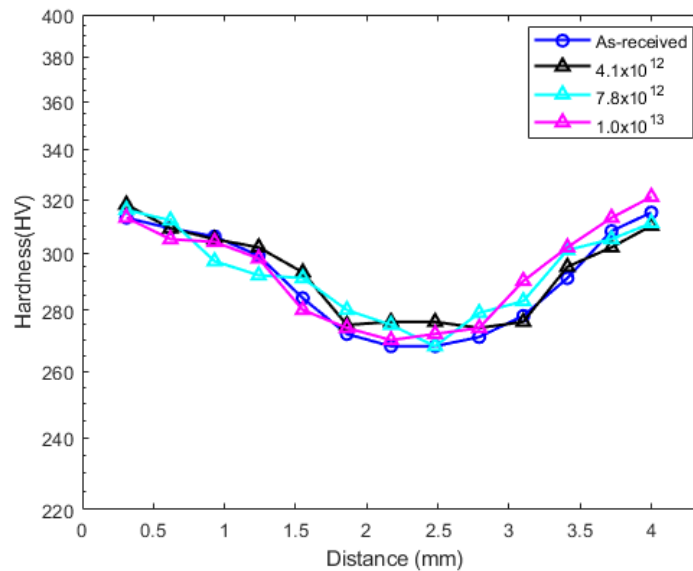


Figure 3.22: Microhardness analysis of the 316 SS samples before and after irradiation (top view).

Analyses were performed for as-received and as-irradiated samples. As seen, the microhardness of the outer surface of the samples are higher than the inner part because the cooling rate is faster in the outside. As mentioned in Section 3.4.6, hardness was measured on the red lines indicated and the values are close to each other. Average hardness using recorded points from the as-received and as-irradiated samples are shown in Table 3.8. The average hardness did not change significantly after the irradiation for the top view analyses. Next, microhardness tests were performed from the side view for the samples that received fluence of 1.0×10^{13} p/cm² to see any possible difference along the penetration depth. The results of these analyses are given in Figure 3.23 and Figure 3.24 respectively. Hardness of the samples from the irradiated end to the unirradiated end are seen. Along the depth of the material, no significant change in the hardness was observed. It can be said that hardness properties did not change after the irradiation.

Table 3.8: Average hardness for 304 and 316 SS using recorded points from the as-received and as-irradiated samples.

Protons received on the sample	Average Hardness (HV) 304 SS	Average Hardness (HV) 316 SS
0 (As-received)	278.4 ± 26.2	290.9 ± 18.3
4.1×10^{12} p/cm ²	274.8 ± 23.3	293.2 ± 15.9
7.8×10^{12} p/cm ²	279.8 ± 20.5	293.1 ± 15.4
1.0×10^{13} p/cm ²	279.8 ± 15.7	293.5 ± 17.8

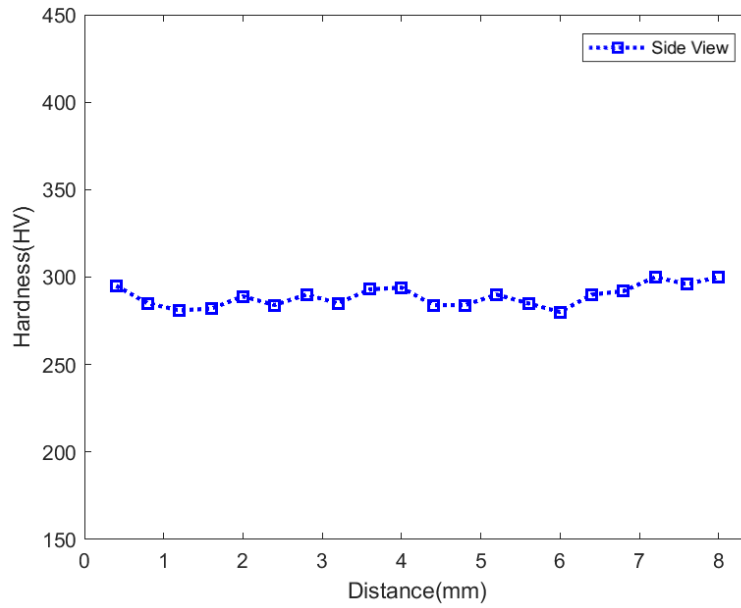


Figure 3.23: Microhardness analysis of 304 SS sample from the side view. This sample received the highest fluence which is 1.0×10^{13} p/cm².

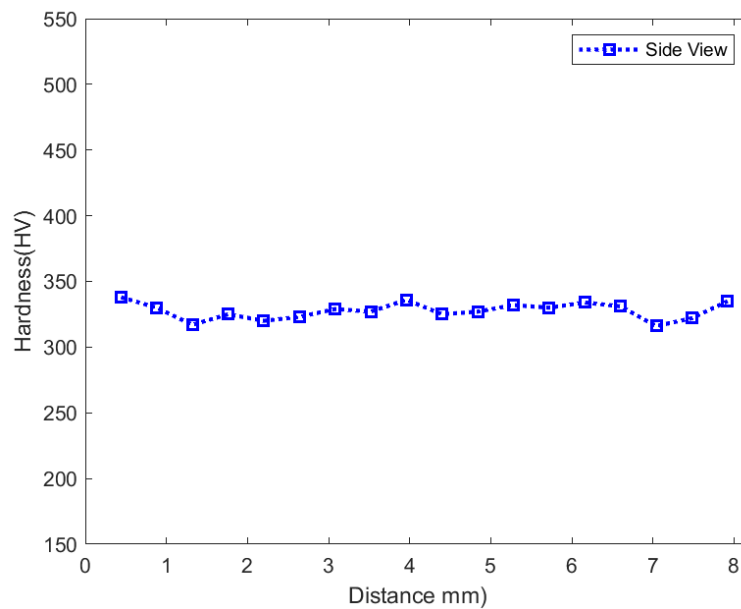


Figure 3.24: Microhardness analysis of 316 SS sample from the side view. This sample received the highest fluence which is 1.0×10^{13} p/cm².

3.6.2 Effects of irradiation on $M_{60}Cr_{13}Mo_{10}B_8Y_2Mn_7$

Optical microscope and SEM images of the specimens were taken for microstructural characterization. The optic images of the as-cast $M_{60}Cr_{13}Mo_{10}B_8Y_2Mn_7$ are shown in Figure 3.25. As seen from optical microscope images, $M_{60}Cr_{13}Mo_{10}B_8Y_2Mn_7$ does not have an amorphous structure. It has some crystalline structures and some unmelted molybdenum parts. Alloy did not form amorphous structure due to the inhomogeneities and insufficient cooling rate. However, it was still irradiated to examine radiation effects on this alloy. SEM images of the different parts of unirradiated sample from the top view are given in Figure 3.26 and 3.27 respectively.

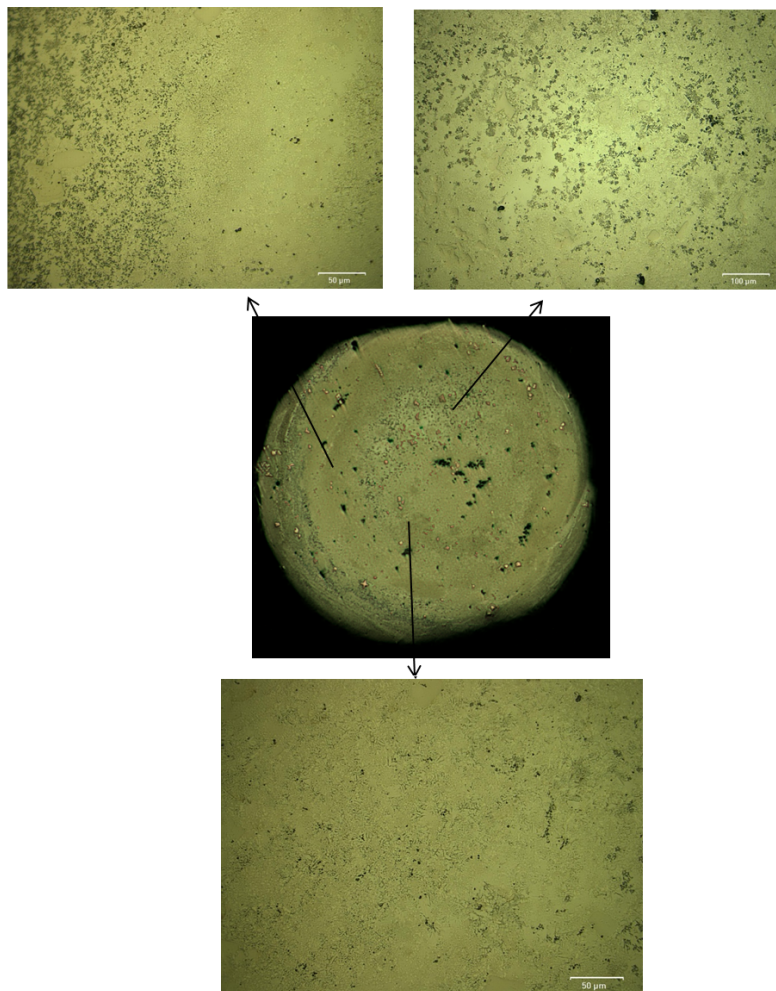


Figure 3.25: Optical microscope images of $M_{60}Cr_{13}Mo_{10}B_8Y_2Mn_7$ sample before the irradiation.

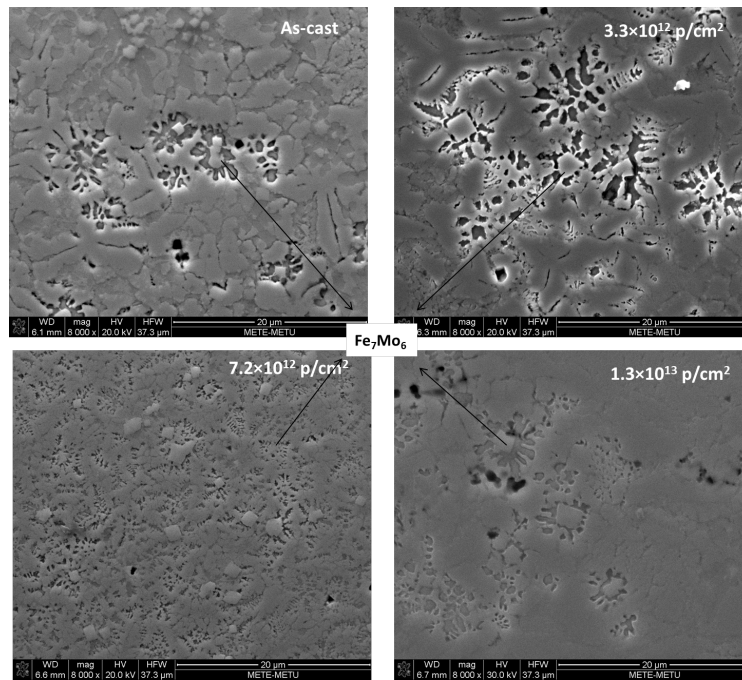


Figure 3.26: SEM images of unmelted molybdenum parts of $M_{60}Cr_{13}Mo_{10}B_8Y_2Mn_7$ samples before and after irradiation (top view). A possible phase is Fe_7Mo_6 .

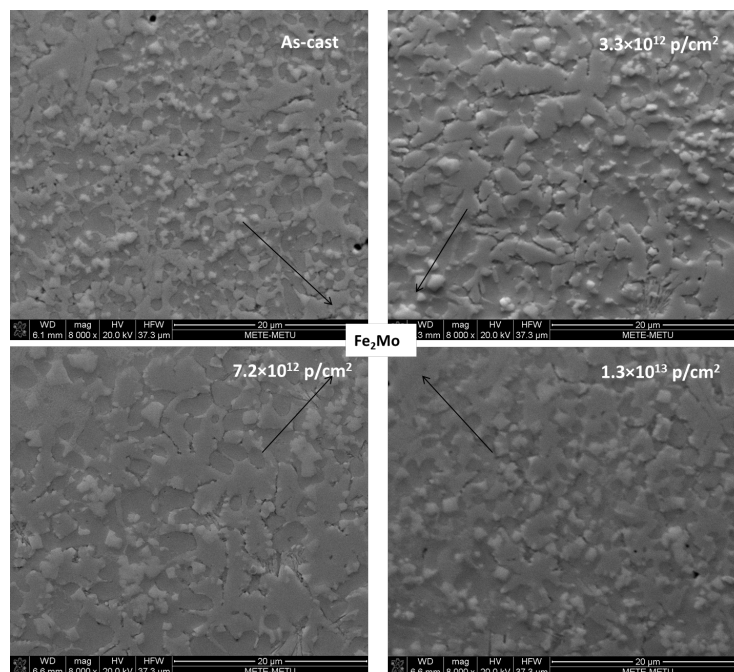


Figure 3.27: SEM images of crystalline parts of $M_{60}Cr_{13}Mo_{10}B_8Y_2Mn_7$ samples before and after irradiation (top view). A possible phase is Fe_2Mo .

After this analysis, the highest fluence sample which received fluence of 1.3×10^{13} p/cm² was analyzed from the side view to examine the sample along the penetration depth, like other samples. SEM images were taken from three different points along the beam direction are given in Figure 3.28 and 3.29 respectively. Point 1 and point 2 represent approximately at a depth of 1 mm and 2 mm respectively while point 3 indicates a depth of roughly 8 mm.

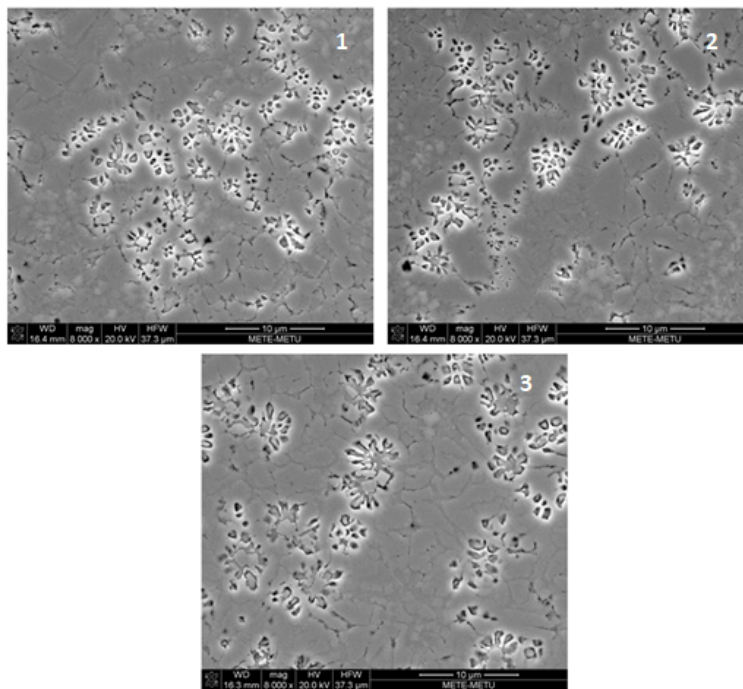


Figure 3.28: SEM images of unmelted molybdenum parts of $M_{60}Cr_{13}Mo_{10}B_8Y_2Mn_7$ sample from side view. These images are shown for three different parts of the highest fluence sample which is 1.3×10^{13} p/cm².

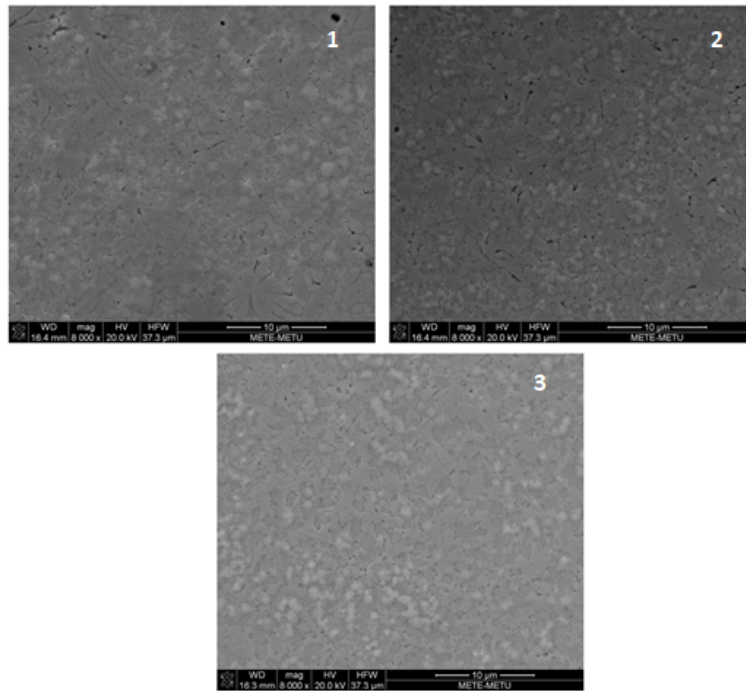


Figure 3.29: SEM images of the crystalline part of $M_{60}Cr_{13}Mo_{10}B_8Y_2Mn_7$ from side view. These images are shown for three different parts of the highest fluence sample which is $1.3 \times 10^{13} \text{ p/cm}^2$.

Defects such as delamination, exfoliation, blistering or cracking were not observed after the irradiation in neither the top nor the side view images. Similar crystalline structures were observed before and after the irradiation and no new phase formation was seen on the samples in according to EDS analysis.

XRD analysis was performed and the results are shown in Figure 3.30. XRD patterns of $M_{60}Cr_{13}Mo_{10}B_8Y_2Mn_7$ alloy show that no new phase formation was seen. A small intensity difference is only observed and a possible reason of that is point defects like vacancies and interstitials are formed, as mentioned before.

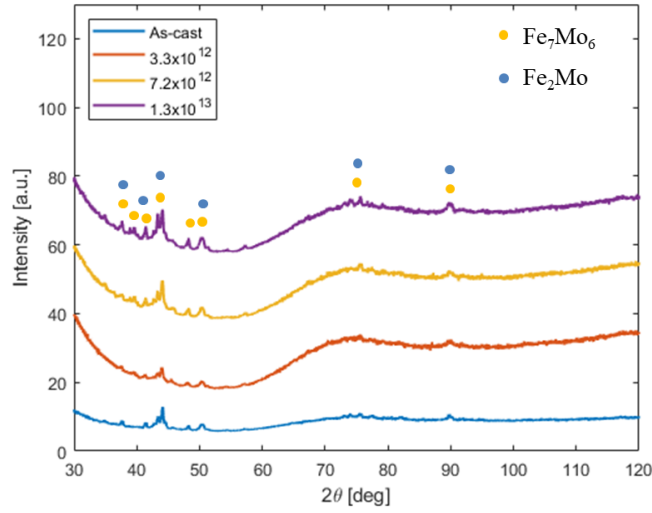


Figure 3.30: XRD patterns of the $M_{60}Cr_{13}Mo_{10}B_8Y_2Mn_7$ samples before and after irradiation. Different colors show the as-cast sample and as-irradiated samples with different fluences.

Microhardness analysis of the alloy are given in Figure 3.31. This analysis was initially performed from the top view. $M_{60}Cr_{13}Mo_{10}B_8Y_2Mn_7$ contains some inhomogeneities so hardness can have small variations. However, hardness of samples are similar to each other for as-cast and all irradiated samples.

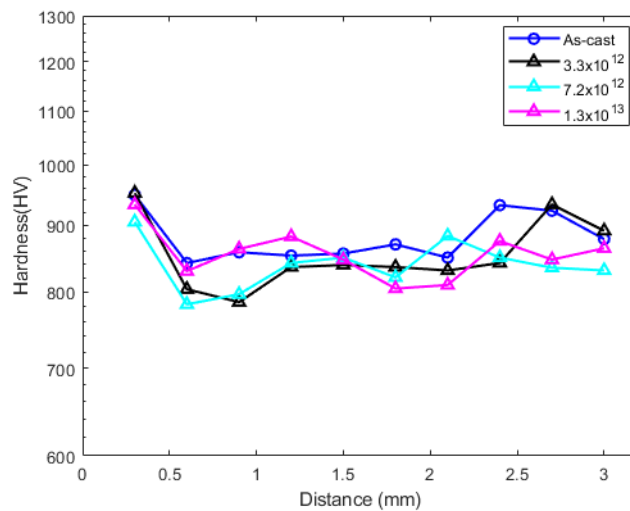


Figure 3.31: Microhardness analysis of the $M_{60}Cr_{13}Mo_{10}B_8Y_2Mn_7$ samples before and after the irradiation (top view).

Average hardness using ten points from the as-received and as-irradiated samples are shown in Table 3.9. The average hardness did not change significantly after the irradiation for the top view analyses. All hardnesses are within error bars of each other and no significant change was observed with increasing radiation.

Table 3.9: Average hardness using ten points from the as-cast and as-irradiated samples.

Protons received on the sample	Average Hardness (HV)
0 (As-cast)	881.1 ± 38.8
3.3x10 ¹² p/cm ²	855.0 ± 53.6
7.2x10 ¹² p/cm ²	839.7 ± 36.3
1.3x10 ¹³ p/cm ²	855.6 ± 37.5

In order to see possible differences along the depth of material, microhardness test was also performed from the side view. The highest fluence sample that received 1.3x10¹³ p/cm² was selected for this analysis. Hardness of the sample through the depth of the material are seen in Figure 3.32. Hardness properties did not change significantly after the irradiation from the unirradiated end to the irradiated end.

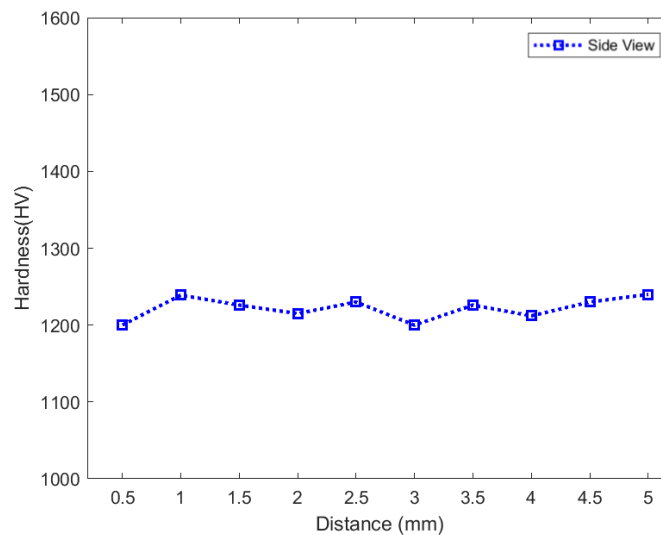


Figure 3.32: Microhardness analysis of the $M_{60}Cr_{13}Mo_{10}B_8Y_2Mn_7$ sample from the side view. This sample received the highest fluence which is 1.3x10¹³ p/cm².

3.6.3 Effects of irradiation on $\text{Fe}_{36}\text{Co}_{36}\text{B}_{19.2}\text{Si}_{4.8}\text{Nb}_4$ Bulk Metallic Glass

Both optical and SEM images of the $\text{Fe}_{36}\text{Co}_{36}\text{B}_{19.2}\text{Si}_{4.8}\text{Nb}_4$ samples are shown before and after the irradiation. Firstly, specimens were examined in the optical microscope and then they were over etched for SEM analysis with higher magnifications. The optical images of the $\text{Fe}_{36}\text{Co}_{36}\text{B}_{19.2}\text{Si}_{4.8}\text{Nb}_4$ BMG samples are shown in Figure 3.33.

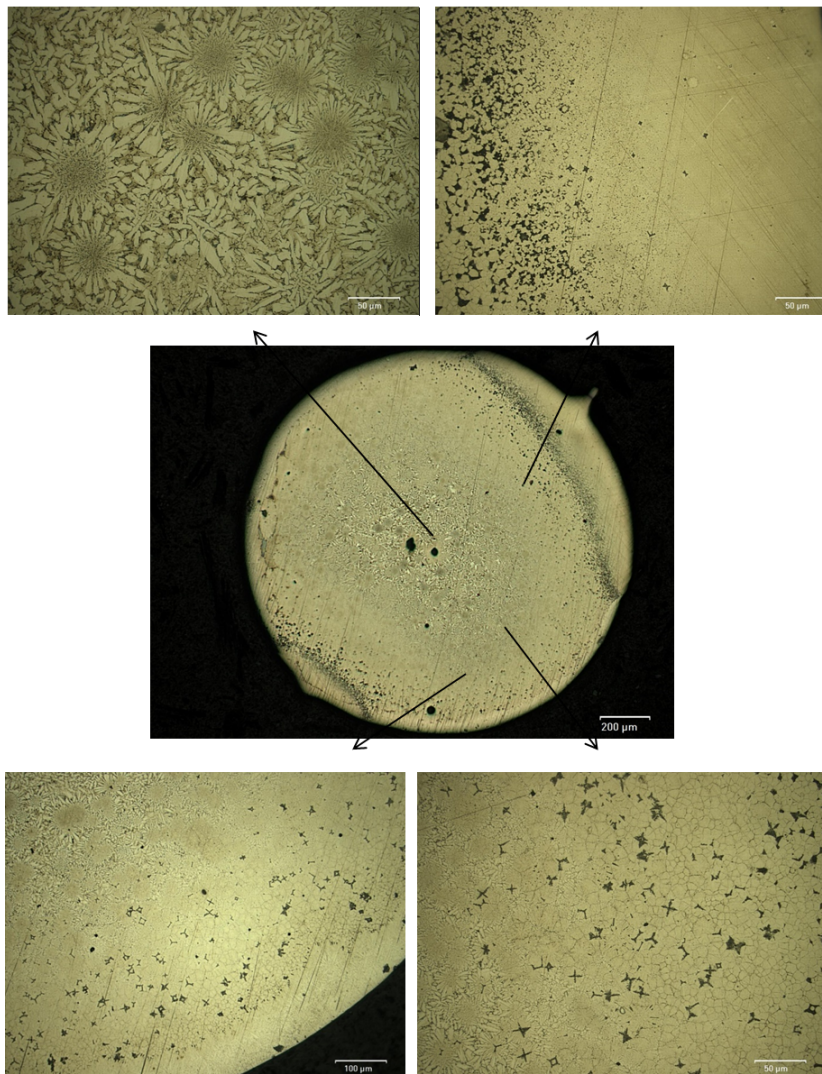


Figure 3.33: Optical microscope image of $\text{Fe}_{36}\text{Co}_{36}\text{B}_{19.2}\text{Si}_{4.8}\text{Nb}_4$ sample before the irradiation.

Optical microscope images $\text{Fe}_{36}\text{Co}_{36}\text{B}_{19.2}\text{Si}_{4.8}\text{Nb}_4$ alloy reveal that the sample is not fully amorphous. The outer surface of the sample cooled faster than the inner part and

so the outer surface of the sample is amorphous. Since the cooling rate was insufficient, the sample was cast as partially amorphous. From the outer surface to the inner, dendrites are seen in the images. In the SEM analysis, both amorphous and dendrite parts are shown in detail with higher magnifications. SEM images of the different parts of $\text{Fe}_{36}\text{Co}_{36}\text{B}_{19.2}\text{Si}_{4.8}\text{Nb}_4$ bulk metallic glass sample before and after the irradiations from the top view are given. In Figure 3.34, SEM images of amorphous part of the $\text{Fe}_{36}\text{Co}_{36}\text{B}_{19.2}\text{Si}_{4.8}\text{Nb}_4$ samples before and after the irradiation are given. SEM images of different dendrite parts of as-cast and as-irradiated samples are shown in Figure 3.35 and Figure 3.36 respectively.

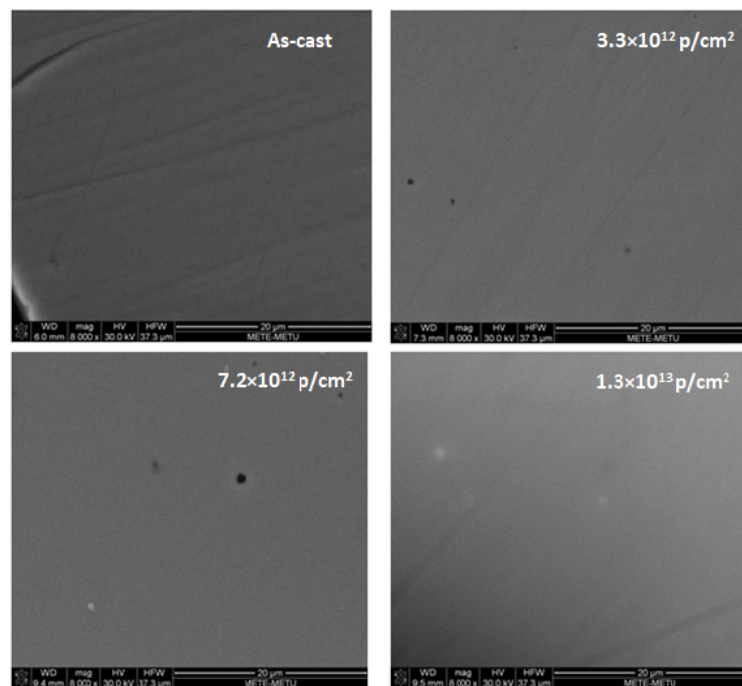


Figure 3.34: SEM images of amorphous part of the $\text{Fe}_{36}\text{Co}_{36}\text{B}_{19.2}\text{Si}_{4.8}\text{Nb}_4$ samples before and after the irradiation (top view).

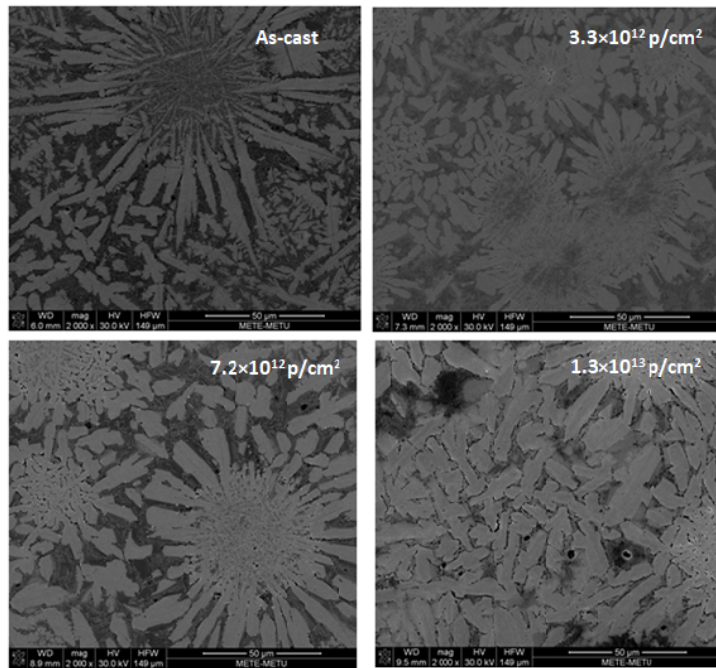


Figure 3.35: SEM images of dendrite part in the $\text{Fe}_{36}\text{Co}_{36}\text{B}_{19.2}\text{Si}_{4.8}\text{Nb}_4$ samples before and after the irradiation (top view).

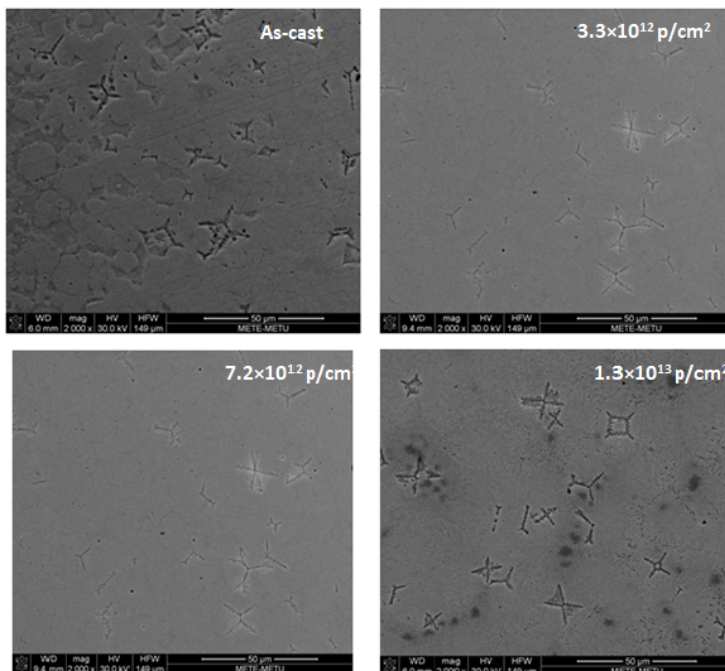


Figure 3.36: SEM images of the dendrite part in the $\text{Fe}_{36}\text{Co}_{36}\text{B}_{19.2}\text{Si}_{4.8}\text{Nb}_4$ samples before and after the irradiation (top view).

After that, the sample which has the highest fluence was examined from the side view. SEM images were taken from three different points along the penetration depth. The SEM images of the sample from the side view are given in Figure 3.37.

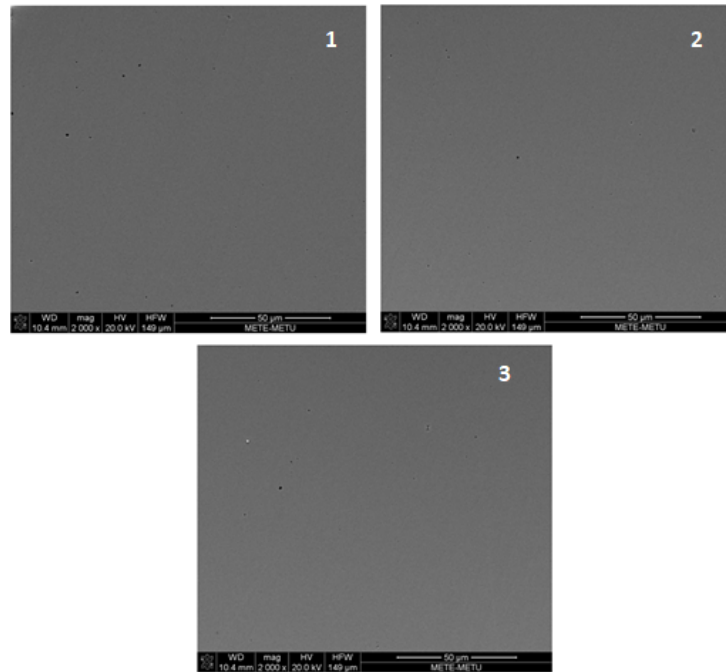


Figure 3.37: The SEM images of the highest fluence $\text{Fe}_{36}\text{Co}_{36}\text{B}_{19.2}\text{Si}_{4.8}\text{Nb}_4$ sample from side view. These images are shown for three different parts of the highest fluence sample which is $1.3 \times 10^{13} \text{ p/cm}^2$.

The microstructures in the $\text{Fe}_{36}\text{Co}_{36}\text{B}_{19.2}\text{Si}_{4.8}\text{Nb}_4$ samples were examined before and after the irradiation. After irradiation, no changes were observed in either top or side view analyses. Amorphous parts remained still amorphous as expected. No surface damage was seen on the samples after 30 MeV proton radiation. These fluences was not enough to create surface damage. According to EDS analysis, no phase formation was observed after the irradiation.

PALS analysis was also performed for this sample and the plot is given in Figure 3.38. Using PATHFIT program, the lifetime and the intensity of the positron were found. After the irradiation, the lifetime of the positrons increased and this shows the defect size inside the material also increased. The number of the vacancies also increased

after the irradiation. These results are in agreement with the SRIM results.

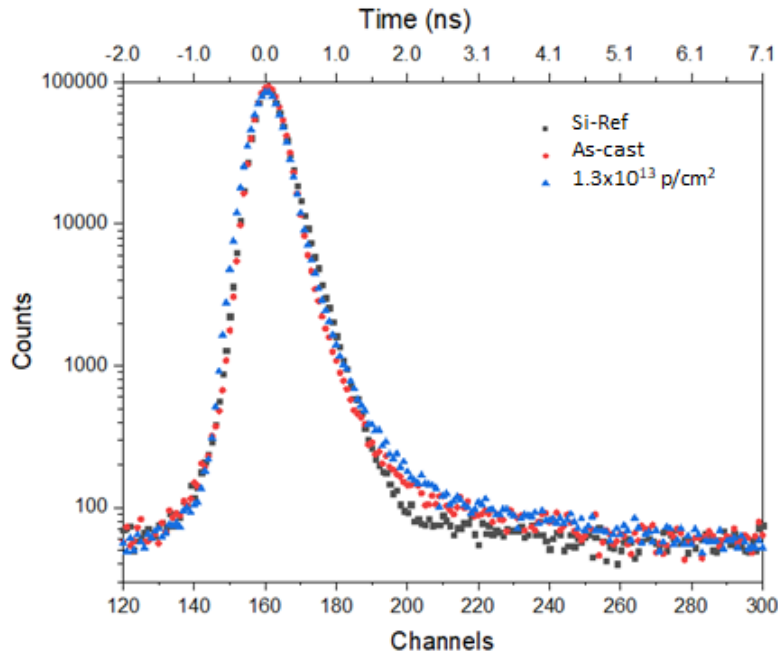


Figure 3.38: Positron annihilation lifetime spectroscopy for $\text{Fe}_{36}\text{Co}_{36}\text{B}_{19.2}\text{Si}_{4.8}\text{Nb}_4$ samples. This analysis was performed for unirradiated sample and sample which received a fluence of $1.3 \times 10^{13} \text{ p/cm}^2$ samples.

Table 3.10: The analysis of positron annihilation lifetime spectroscopy. The lifetime of positron for as-cast and highest fluence samples which is $1.3 \times 10^{13} \text{ p/cm}^2$ samples are given.

Protons received on the sample	$\tau \pm \Delta\tau$ (ns)	$I \pm \Delta I$ (%)
0 (As-cast)	1.40 ± 0.05	1.36 ± 0.04
$1.3 \times 10^{13} \text{ p/cm}^2$	1.81 ± 0.06	1.42 ± 0.03

In order to detect the phases in the sample, XRD analysis were performed. In Figure 3.39, XRD patterns of the $\text{Fe}_{36}\text{Co}_{36}\text{B}_{19.2}\text{Si}_{4.8}\text{Nb}_4$ as-cast and irradiated samples with different fluences are seen.

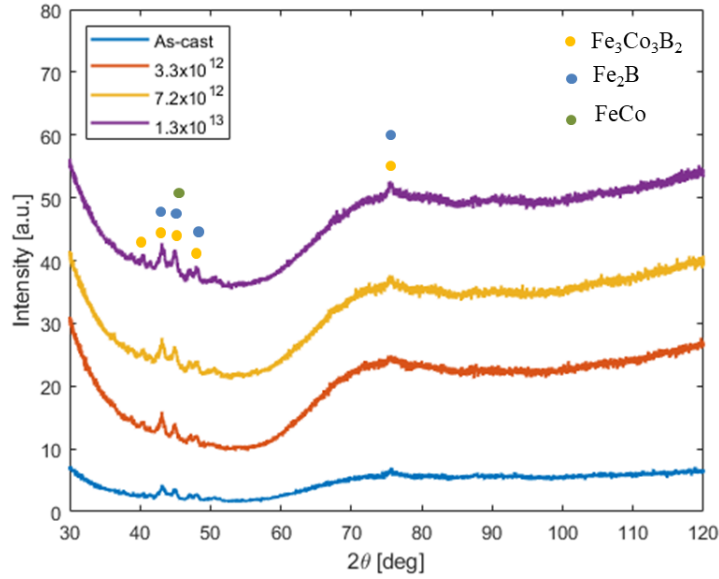


Figure 3.39: XRD patterns of $\text{Fe}_{36}\text{Co}_{36}\text{B}_{19.2}\text{Si}_{4.8}\text{Nb}_4$ samples before and after the irradiation. Different colors represent the as-cast sample and irradiated with different fluences samples.

Normally, amorphous structure has one broad peak in the XRD pattern but, this alloy is partially amorphous therefore, other peaks are also seen. By comparing the XRD and EDS analyses, emerged phases in the pattern were found. The peaks are same for the unirradiated and irradiated samples. No phase formation was observed after the irradiation and this was also checked using EDS results. However, the intensities of peaks changed after irradiation. The reason of this alteration can be vacancy-like defects in material. As explained before in Section 2.4.2, amorphous materials also have point defects and they are called vacancy-like and interstitial-like defects. After the XRD analysis, thermal analysis was also carried out and DSC curves of the $\text{Fe}_{36}\text{Co}_{36}\text{B}_{19.2}\text{Si}_{4.8}\text{Nb}_4$ sample are given in Figure 3.40 and Figure 3.41 for heating paths. Also, cooling paths are given in Figure 3.42 and Figure 3.43 respectively. For these analyses, smaller samples weighing between 15 and 30 mg were prepared.

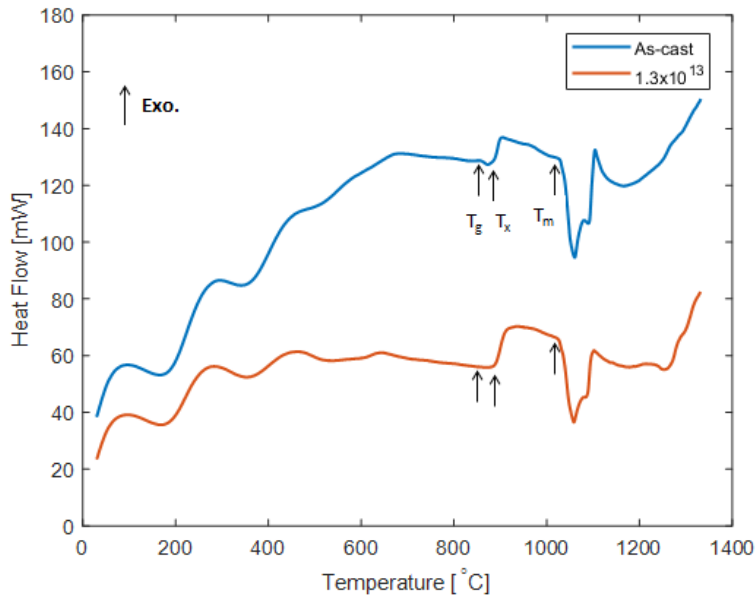


Figure 3.40: DSC curves of the $\text{Fe}_{36}\text{Co}_{36}\text{B}_{19.2}\text{Si}_{4.8}\text{Nb}_4$ for as-cast and the sample which received a highest fluence which is 1.3×10^{13} p/cm² (First Heating Paths).

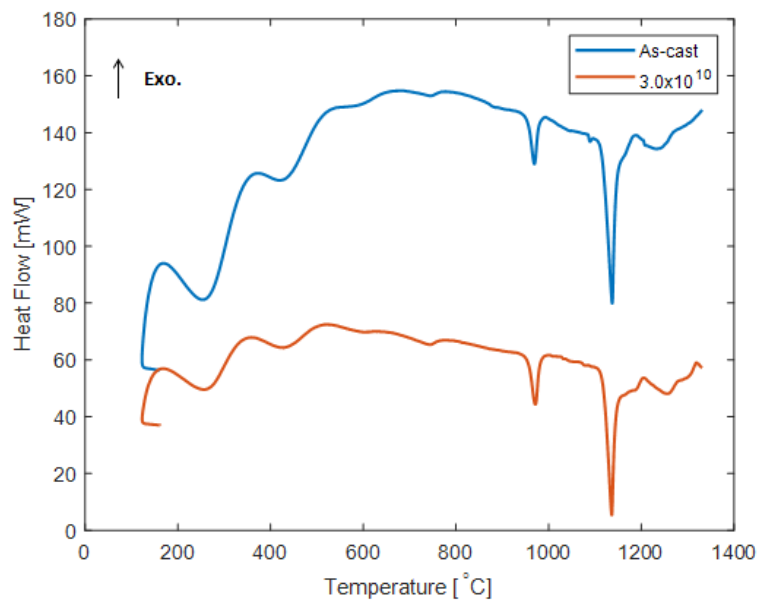


Figure 3.41: DSC curves of the $\text{Fe}_{36}\text{Co}_{36}\text{B}_{19.2}\text{Si}_{4.8}\text{Nb}_4$ for as-cast and the sample which received a highest fluence which is 1.3×10^{13} p/cm² (Second Heating Paths).

Table 3.11: Phase transformation temperatures of as-cast and after receiving a fluence of 1.3×10^{13} p/cm² samples.

Protons received on the sample	T _x (°C)	T _g (°C)	T _m (°C)
0 (As-cast)	873	844	1013
1.3×10^{13} p/cm ²	881	846	1013

Phase transformation temperatures of as-cast and after receiving a fluence of 1.3×10^{13} p/cm² samples from heating paths are shown in Table 3.11. T_x, T_g and T_m temperatures are seen and Supercooled liquid region (T_x-T_g) is 29 °C before the irradiation and it is 35 °C after receiving a fluence of 1.3×10^{13} p/cm². Supercooled liquid region for sample that has the highest fluence, which is 1.3×10^{13} p/cm², enhanced after the 30 MeV proton irradiation.

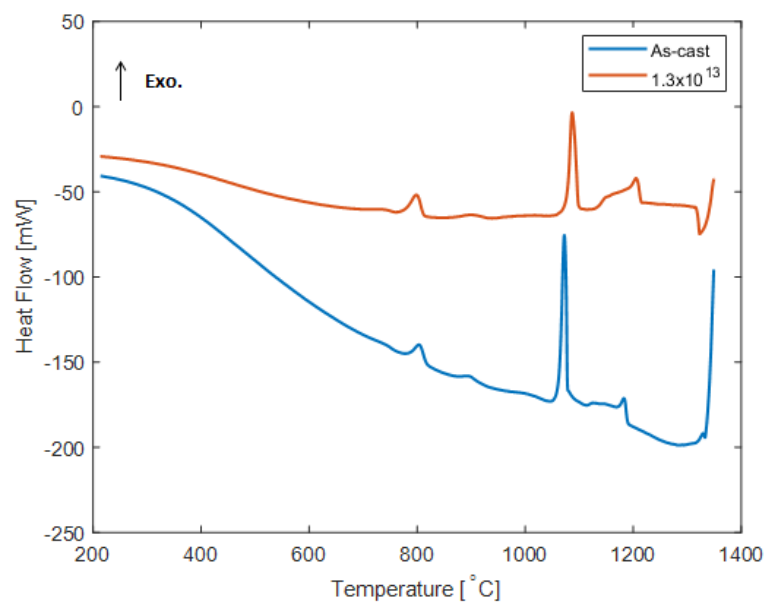


Figure 3.42: DSC curves of the Fe₃₆Co₃₆B_{19.2}Si_{4.8}Nb₄ for as-cast and the sample which received a highest fluence which is 1.3×10^{13} p/cm² (First Cooling Paths).

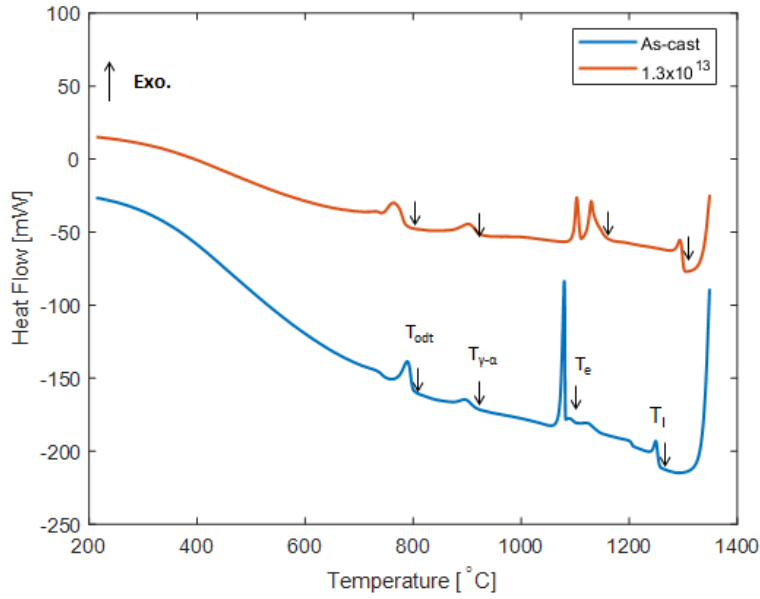


Figure 3.43: DSC curves of the $\text{Fe}_{36}\text{Co}_{36}\text{B}_{19.2}\text{Si}_{4.8}\text{Nb}_4$ for as-cast and the sample which received a highest fluence which is $1.3 \times 10^{13} \text{ p/cm}^2$ (Second Cooling Paths).

Table 3.12: Phase transformation temperatures for as-cast and after receiving a fluence of $1.3 \times 10^{13} \text{ p/cm}^2$ samples.

Protons received on the samples	T_{odt} (°C)	$T_{\gamma-\alpha}$ (°C)	T_e (°C)	T_i (°C)
0 (As-cast)	814	940	1110	1270
$1.3 \times 10^{13} \text{ p/cm}^2$	805	940	1120	1317

Phase transformation temperatures of the samples for as-cast and after receiving a fluence of $1.3 \times 10^{13} \text{ p/cm}^2$ from the cooling path are shown in Table 3.12. Some transformation temperatures changed after the irradiation. A possible reason for this case is structural defects such as vacancy and interstitial like defects. Furthermore, VSM analysis explain some changes like structural defects because coercivity is also affected from these defects. Therefore, VSM analysis for the $\text{Fe}_{36}\text{Co}_{36}\text{B}_{19.2}\text{Si}_{4.8}\text{Nb}_4$ samples were conducted for analyzing of magnetic properties and the results are given in Figure 3.44. Smaller 30-50 mg samples were prepared for this analysis.

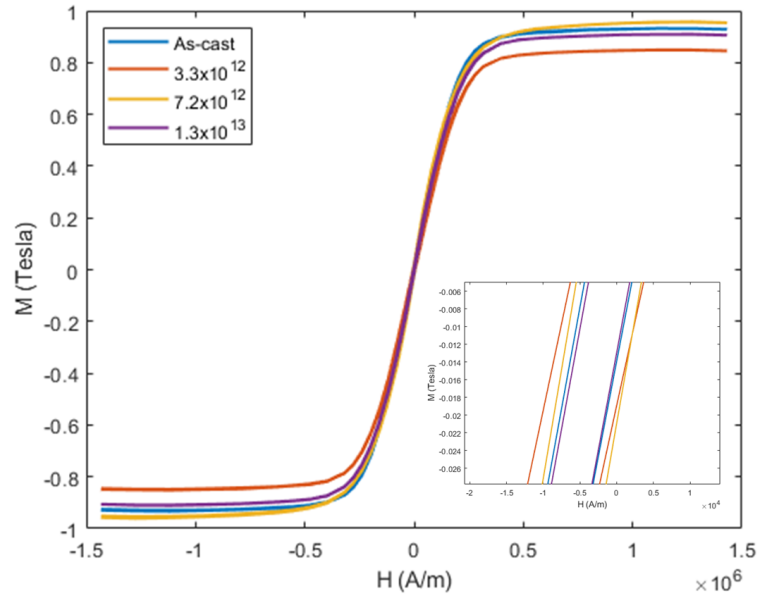


Figure 3.44: VSM analysis of the $\text{Fe}_{36}\text{Co}_{36}\text{B}_{19.2}\text{Si}_{4.8}\text{Nb}_4$ samples before and after irradiation. Colors indicate different fluences.

VSM studies were performed for magnetic characterization before and after the irradiation. VSM curve of the $\text{Fe}_{36}\text{Co}_{36}\text{B}_{19.2}\text{Si}_{4.8}\text{Nb}_4$ samples gives the saturation magnetization (M) in terms of Tesla and coercivity (H) with the units of A/m. This material has soft magnetic properties such as high saturation magnetization (0.75 - 1.1 T) and low coercivity (100 - 1000 A/M). These values were found from the analysis and shown in Table 3.13.

Table 3.13: Saturation magnetization and coercivity of $\text{Fe}_{36}\text{Co}_{36}\text{B}_{19.2}\text{Si}_{4.8}\text{Nb}_4$ samples. VSM analysis was carried out as-cast and as-irradiated samples.

Protons received on the samples	Saturation Magnetization (T)	Coercivity (A/m)
0 (As-cast)	0.929	159.54
3.3×10^{12} p/cm ²	0.845	319.10
7.2×10^{12} p/cm ²	0.958	398.85
1.3×10^{13} p/cm ²	0.906	478.62

Saturation magnetization is only dependent on the composition of material and small

changes are negligible. Saturation magnetization values of the $\text{Fe}_{36}\text{Co}_{36}\text{B}_{19.2}\text{Si}_{4.8}\text{Nb}_4$ samples before and after irradiation are between 0.845 and 0.958 so they are close. Mapping analysis was performed to see the composition of the irradiated sample for saturation magnetization. In Figure 3.45, the mapping images of the irradiated sample are given and this analysis provides a virtual demonstration. The composition of the sample remains homogeneous as expected after irradiation, so saturation magnetization has not changed enough to cause significant difference.

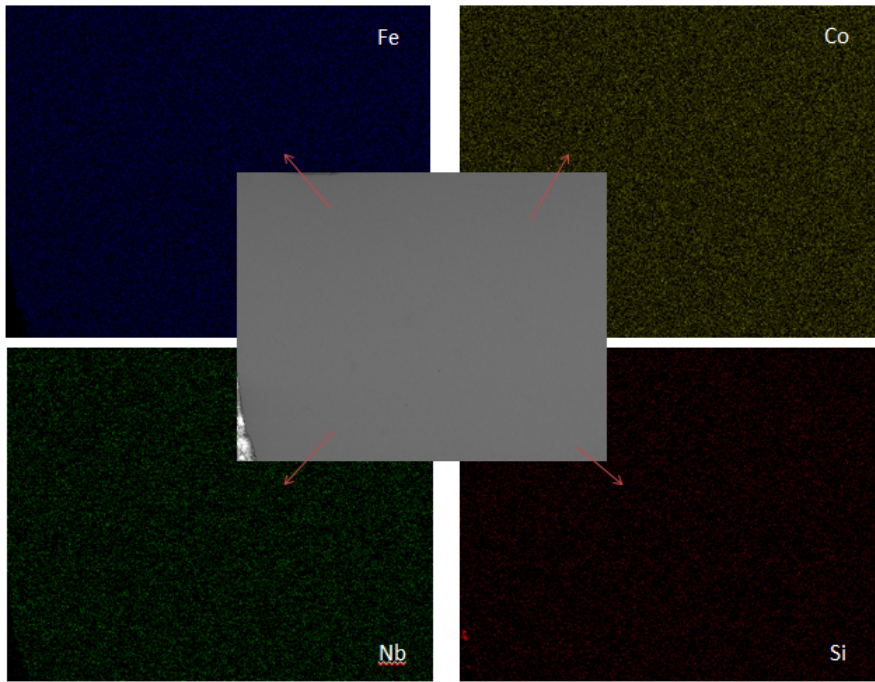


Figure 3.45: EDS mapping analysis for the $\text{Fe}_{36}\text{Co}_{36}\text{B}_{19.2}\text{Si}_{4.8}\text{Nb}_4$ sample at a received fluence of 1.3×10^{13} p/cm².

Coercivity is susceptible to structural defects rather than composition. For instance, in the case of low coercivity, domain walls move easily. On the other hand, if the material has structural defects like voids, the movement of the domain walls became tougher and the coercivity increases [101]. In the case of the $\text{Fe}_{36}\text{Co}_{36}\text{B}_{19.2}\text{Si}_{4.8}\text{Nb}_4$ sample analyzed here, the coercivity increased as a result of structural defects. VSM results also prove the formation of defects in the sample as a result of radiation. Finally, microhardness test were conducted and the results are given in Figure 3.46. The hardness of unirradiated and irradiated samples averaged over ten values are listed in

Table 3.14 and the average hardness did not change with irradiation.

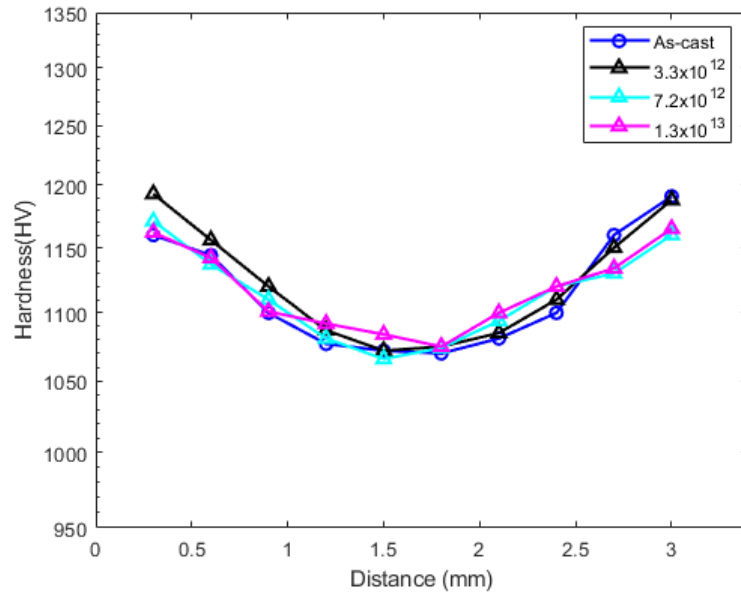


Figure 3.46: Microhardness analysis of the Fe₃₆Co₃₆B_{19.2}Si_{4.8}Nb₄ samples before and after the irradiation (top view).

Table 3.14: Average hardness values of the samples before and after irradiation. These averages were taken for ten points on each sample.

Protons received on the sample	Average Hardness (HV)
0 (As-cast)	1115.5 ± 48.5
3.3x10 ¹² p/cm ²	1123.6 ± 43.8
7.2x10 ¹² p/cm ²	1114.3 ± 34.3
1.3x10 ¹³ p/cm ²	1117.5 ± 31.7

After this analysis, microhardness test was performed from the side view for the sample that received the highest fluence, to see the hardness along the penetration depth of the material. The result of this analysis is given in Figure 3.47 from the irradiated end to the unirradiated end. No alteration of the hardness was not observed.

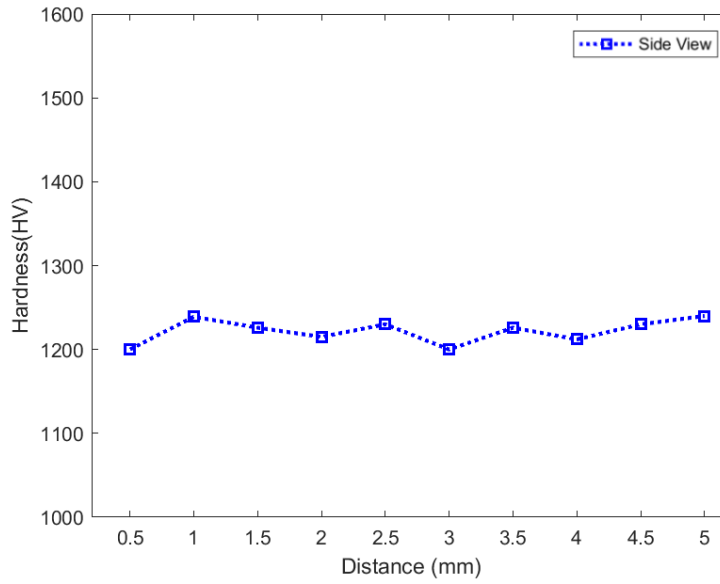


Figure 3.47: Microhardness analysis of the $\text{Fe}_{36}\text{Co}_{36}\text{B}_{19.2}\text{Si}_{4.8}\text{Nb}_4$ sample from side view. This sample received the highest fluence which is 1.3×10^{13} p/cm².

In this chapter, first, the production of BMGs were discussed. Then, radiation tests of SSs and BMGs were followed by characterization of these materials to examine the effects of radiation. Radiation damage was observed in some analyses such as XRD, DSC, VSM and PALS, but no surface damage in SEM nor any difference in the microhardness analyses was observed.

CHAPTER 4

SHIELDING DESIGNS FOR METU-DBL AND RADIATION PROTECTION

Shielding is a mandatory precaution to decrease the radiation dose in the R&D room of TAEA PAF for the health of the METU-DBL workers and users and also to protect the electronic components of METU-DBL from radiation damage. For the pretests performed between 21 December 2017 and 19 March 2018, first, a shielding study to reduce prompt dose on electronic components and beam elements of the METU-DBL will be presented and then, radiation protection studies that contain radioisotope activation and the necessary cooling time studies will be given in this section. For these studies, FLUKA which is a very comprehensive program for various applications in high energy, particle and nuclear physics was employed. Owing to its flexible geometry interface and user friendly input files in FLUKA, many functions, such as shielding, detector design, medical studies and nuclear calculations, can be modeled [53].

ALARA (As Low As Reasonably Achievable) principle is imperative for shielding and radioprotection studies. Principle expresses that the dose should be kept as low as reasonably achievable, while economic and social factors are being taken into account [102]. This principle is the guiding rule for evaluating the simulation results which were always performed using 30 MeV protons as the highest momentum transfer scenario.

4.1 Shielding Studies for Electronic Components and Beam Elements of METU-DBL

In this section, shielding studies for electronic components in the METU-DBL subsystems and beam elements, such as the first protective collimator, will be presented. First, the protective collimator, which receives a dose from the primary protons and can get activated, was shielded for the pretests to reduce the dose in the room. Also, the electronic components of diamond and Timepix detectors and the components of fiber scintillators as well as the readout of the pixel detector, its step engine and also a mobile radiation robot were shielded. Moreover, electronic components of the cooling subsystem, the turbomolecular pump of the vacuum subsystem, electronic components of the cooling subsystem and finally a programmable logical controller (PLC) of the control subsystem were shielded to preserve them from radiation damage during irradiations. A study with primary protons is more important than secondaries, for the shielding studies of the electronics of the test and measurement subsystem. On the other hand, for the cooling, vacuum, and control subsystems, which are not directly exposed to the beam, secondary particles are more critical. All simulations were run with 10^6 particles to have adequate statistics.

For shielding studies, material selection is critical. A literature search was performed to find promising materials. Electrons are the main secondary particle produced at METU-DBL followed by gammas and neutrons. For shielding materials, aluminum, polyethylene and lead were preferred for their machinability, and their stopping power as mentioned in Section 2.2. Aluminum 6082 was selected to stop primary protons in the collimator design as well as secondary electrons. The 6000 series of aluminum are used in space structures and satellites due to their durable and lightweight nature. For example, the windows of ISS are made with thicker glass than their Earth counterparts and in addition to these windows, aluminum shutters are placed to increase the safety of the astronauts [103]. Al6082 has a good machinability, is light weight, has excellent corrosion resistance and also is good at stopping protons, so it was used in shielding studies. The chemical composition of the Al6082 is shown in Table 4.1.

Table 4.1: The chemical composition of Aluminum alloy 6082 [104].

Element	wt %
Si	0.7-1.3
Fe	0.0-0.5
Cu	0.0-0.1
Mn	0.4-1.0
Mg	0.6-1.2
Zn	0.0-0.2
Ti	0.0-0.1
Cr	0.0-0.25
Al	Balance

Polyethylene was chosen to slow down neutrons due to its very high hydrogen content. At the time of writing this thesis, borated high density polyethylene, which would have been preferable, was not readily available in Turkey. A related R&D and production project was filed with TUBITAK to mitigate this procurement issue [105]. Lead is a dense material with a high atomic number, which is very effective in stopping gammas, but extreme care must be taken during its processing due to its toxicity.

The electronic components, which must be protected, are modelled in FLUKA as consisting of teflon (0.18 cm thick), copper (0.06 cm thick) and silicon (0.1 cm thick) because in general, conventional electronics comprise of these materials. All beam elements in METU-DBL in TAEA PAF room such as magnets, collimators and the beam dump were defined in FLUKA. In Figure 4.1, the model of the room that includes some TAEA PAF beamline elements and the 5 port magnet as well as METU-DBL are indicated with black arrows. METU-DBL follows from the right-most exit of the 5-port magnet at an angle of 40° . Electronic components and beam elements are placed in their prospective positions in the R&D room and shielding studies for each were carried out separately by considering their locations. Positions of each electronic component in various subsystems will be given in the related section.

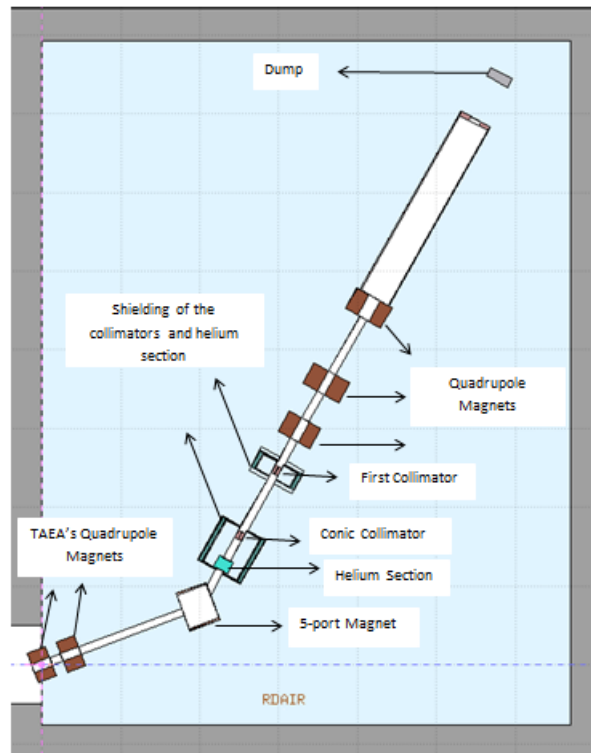


Figure 4.1: A model of the R&D room in the FLAIR, the visual interface of FLUKA includes TAEA PAF beamline elements as well as the 5 port magnet and METU-DBL. Beam elements, such as magnets, collimators, and beam dump, are indicated with black arrows. METU-DBL follows from the right-most exit of the 5-port magnets at an angle of 40° .

METU-DBL has four pre-defined characteristic irradiation scenarios. These scenarios are shown in Table 4.2. Radiation tests of solar cells should be performed with 1 MeV electrons or 10 MeV protons, which are LET-equivalent. The lowest energy setting of TAEA PAF, which is 15 MeV, will be used to test solar cells after a degrader. In this so-called scenario A, the proton energy is reduced to an average of 10 MeV at a flux of 8.3×10^5 p/cm²/s. Preliminary SEE tests, classified as scenario B, provide a very low proton flux for users who would like to test electronics slowly. The scenario C provides a high flux for users that would like to reach a high fluence in short period of time. The final scenario, D, is intended to provide a 10^{14} p/cm² fluence to users that want to test electronics for Hi-Lumi LHC in just 80 minutes [47].

The dose in the room depends on parameters such as collimator aperture, irradiation time and current. These are important for shielding studies because the radiation dose level in the room and also deposited energies in the electronics are different for each of these scenarios. The conical collimator used in METU-DBL can be adjusted to different apertures. The minimum conical square opening extends from 1 to 2 mm while the maximum opening extends from 9 to 10 mm. The aperture of the first protective collimator is fixed (1 cm).

Table 4.2: The possible radiation scenarios of METU-DBL. Each scenario is planned to be used for different purposes. Energy, current and aperture of the conic collimator for each one are shown.

Scenario	Energy (MeV)	Current (μA)	Aperture of conic collimator	Purpose	Flux ($\text{p}/\text{cm}^2/\text{s}$)
A	15	1	1 mm \rightarrow 2 mm	Solar cell radiation tests	8.3×10^5
B	30	1	1 mm \rightarrow 2 mm	Pre SEE Tests	8.3×10^5
C	30	1	9 mm \rightarrow 10 mm	SEE Tests (ESA ESCC No. 25100)	1.9×10^7
D	30	100	9 mm \rightarrow 10 mm	High Luminosity LHC Tests	1.9×10^9

The worst scenario that produces the highest secondary dose in both the R&D room and also on the electronic components is Scenario D. Therefore, shielding studies were performed by considering the worst scenario of METU-DBL for reliable and robust performance. This scenario uses 100 μA current, 80 minutes of irradiation time and a conic collimator aperture setting is extending from 9 mm to 10 mm. Shielding of electronic components in the target area were performed using Scenario C. The reason is that for, Scenario D, which is the worst-case situation for radiation protection, the beam's uniformity will be measured using a lower setting (1 μA as in Scenario C). The flux will only be spot-checked using the most radiation hard detector, which is the diamond detector, to validate the proportionality between the beam current and the flux.

4.1.1 Shielding Studies for METU-DBL Collimators

TAEA PAF R&D room is defined as a supervised area. The upper limit for exposure to radiation workers in controlled areas at CERN is $3.0 \mu\text{Sv/h}$ [106]. Therefore, shielding and protection studies have been carried out according to a more conservative limit of $2.5 \mu\text{Sv/h}$ to allow for statistical errors. In order to reduce the dose in R&D room, the shielding studies for METU-DBL were started with the shielding of the beam line. The most active part of the beam line was found as the first protective collimator in FLUKA because primary protons from the beam and the resulting secondary particles leave high doses around the collimator during an irradiation. The conic collimator was not yet ready for the pretest. In its place a first protective collimator shown in Figure 4.2 was used. The first protective collimator was made of SS 316 and has a 14.0 cm length including flanges and its inner radius is 10.0 cm.

In order to decrease the dose level in the room and also to protect electronic components from secondaries, this first collimator was shielded with a sandwich structure consisting of Al: 0.5 cm, Pb: 1.0 cm, PE: 5.0 cm and Al: 0.5 cm from the inside to the outside. Dose received on a tissue sample 5.0 cm away from the collimator was minimized. The geometry of the design was chosen as octagonal shape for ease of production and integration. Minimizing the space between the collimator and shielding helps to stop the secondary particles without spreading over a large area and reduces the amount of material that will be required. The shielding of the first collimator from two different angles are shown in Figure 4.3. The mass of the shielding in total is 51.0 kg. Its face has an area of 40.5 cm x 40.5 cm and its length is 15.0 cm. The shielding of first protective collimator consists of four parts mechanically, the upper and lower halves of the shielding and front and back covers, which were designed not to limit the accessibility to the flanges. Therefore, the covers are slightly thinned with respect to the upper and lower halves. The shielding of the covers is Al: 0.5 cm, PE: 2.0 cm, Pb: 1.0 cm and Al: 0.5 cm from the outside to the inside.

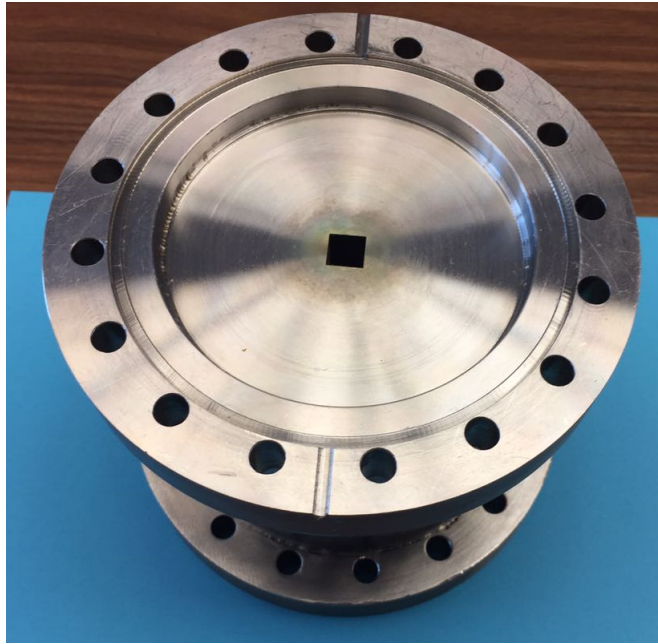


Figure 4.2: The first protective collimator of METU-DBL without shielding. It has a 14.0 cm length including flanges and its inner radius is 10.0 cm.

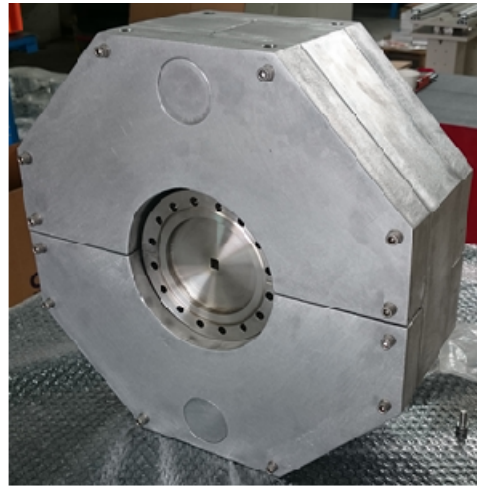
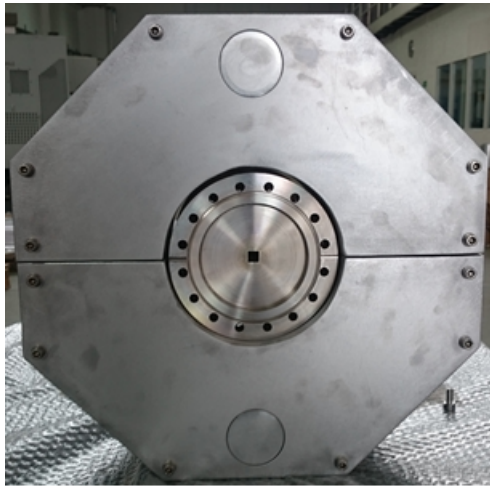


Figure 4.3: The shielding of the first collimator from two different angles. It consists of upper and lower halves of shielding and front and back covers. Its face has an area of 40.5 cm x 40.5 cm and its length is 15.0 cm.



Figure 4.4: The first protective collimator assembled into the METU-DBL pretest beam line. Shielding of the collimator has an octagonal shape.

The dismantling of this protective SS316 collimator after the pretests proved to be challenging due to high doses observed 5 cm away from it. A sarcophagus was custom made for this collimator to protect METU-DBL personnel during its removal to a safe zone. The lesson learnt from this exercise was that collimators should preferably be made from Al6082 which activates less during irradiation. These studies will be presented in Section 3.2.1. Shielding studies also were performed for the adjustable conic collimator made of Al6082. Various shielding designs were tried to find the optimum one. Dose received on a tissue sample 5.0 cm away from the collimator was minimized.

Table 4.3: Comparative results of shielding studies for different shielding options of the adjustable conic collimator. Dose received in 1 second, 1 hour or 1 day after an irradiation lasting 1 hour is given.

No	Shield thicknesses from the inside to the outside (cm)	Dose received 1 second after (μSv)	Dose received 1 hour after (μSv)	Dose received 1 day after (μSv)
1	Al:0.5 – PE: 0.5 - Pb:0.5 - PE:0.5 - Al:0.5	119.0	21.6	2.9
2	Al:0.5 – Pb:3.0 – PE: 1.0 - Pb:1.0 - Al:0.5	11.6	9.5	0.8
3	Al:0.5 – PE: 1.0 - Pb:1.0 - PE:1.0 - Al:0.5	10.0	8.8	1.1
4	Al:0.5 – Pb:1.0 – PE: 1.0 - Pb:1.0 - Al:0.5	9.6	8.9	2.4
5	Al:0.5 – PE: 1.0 - Pb:0.5 - PE:1.0 - Al:0.5	55.0	15.1	1.8
6	Al:0.5 – PE: 1.0 - Pb:2.0 - PE:1.0 - Al:0.5	7.7	3.3	1.2
7	Al:0.5 – PE: 2.0 - Pb:1.0 - PE:1.0 - Al:0.5	21.1	6.6	2.3
8	Al:0.5 – PE: 3.0 - Pb:1.0 - PE:1.0 - Al:0.5	76.7	23.9	2.5
9	Al:1.5 – Pb:1.5 - Al:1.0	38.9	8.2	1.6

Nine different shielding designs were studied. In the innermost and outermost layers, 0.5 cm aluminum are required for mechanical integrity and also to stop stray 30 MeV protons inside the aluminum layer. Third design was selected as a shielding of the conic collimator. Increasing the polyethylene layers, also increases the dose as seen from the seventh and eighth options. In some options, received dose is lower than the third option, but the thicker lead layer causes a larger weight and also a higher cost. The technical drawing of the adjustable conical collimator is shown in Figure 4.5. It has an octagonal shape and its facial area is 40.0 cm x 40.0 cm while its depth is 28.0 cm.

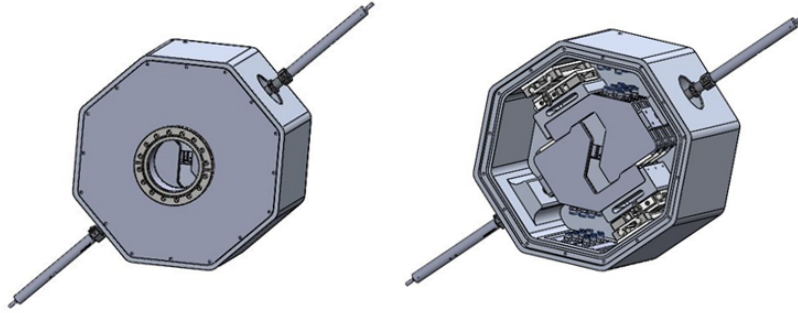


Figure 4.5: The technical drawing of the adjustable conical collimator. The outer part (left) and the inner part (right) of it are shown. It has an octagonal shape and its area of 40.0 cm x 40.0 cm while its depth is 28.0 cm.

4.1.2 Shielding Studies for Electronic Components in the METU-DBL Subsystems

METU-DBL is divided into several subsystems such as cooling, vacuum, control, robotic and, test and measurement system. Each system has electronic components that are susceptible to radiation damage. In FLUKA, shielding studies were performed for each of these electronic components taking into account the specific dose they will receive at their designated locations.

4.1.2.1 Shielding Studies for Electronic Components of Test and Measurement System

Several electronic components were shielded to prevent radiation damage, namely: the TimePix3 pixel and diamond detector's on-board electronics, photodiodes and components of the fiber scintillators that are used in the measurement of radiation in the target area. Also shielding studies were conducted for other components in the target area such as step motors.

There is a thickness restriction for the shielding of electronic components in the target area. The device under test should not be more than 5 cm away from the titanium

vacuum window to avoid energy loss and scattering in air. Therefore the detectors plus the shielding must fit in this 5 cm distance. The technical drawing of the position of the detectors and the device under test (DUT) for the pretest setup are seen in Figure 4.6. The parking positions and movement mechanisms of the TimePix3 detector, the diamond detector, the fiber scintillators and readout electronics can be seen.

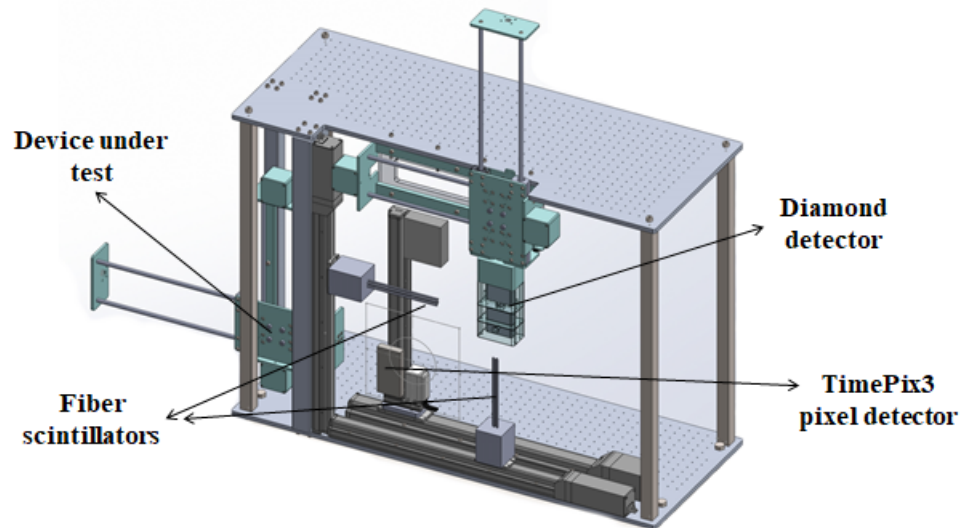


Figure 4.6: Technical Design of the test table in target area for the pretests. The parking positions and movement mechanisms of the TimePix3 detector, the diamond detector, the fiber scintillators and readout electronics can be seen [107].

Shielding of the Timepix3 and Diamond Detectors

The shielding studies of the electronic components in the readout of the pixel and diamond detectors have been carried out simultaneously because they have similar positions in the target area. These detectors scan the target area on the same plane and then return to their respective parking position. Therefore, each of these detectors scan the beam for a period of approximately three to five minutes. In Table 4.4, comparative results of several shielding studies for their electronic components to find optimum one are presented. It shows the doses received by the electronics in one hour of irradiation for designs of varying shielding materials and thicknesses.

Table 4.4: Comparative results of shielding studies for the readout electronics of the pixel and diamond detectors. Doses received in one hour of irradiation for designs of varying shielding materials and thicknesses are shown.

No	Shield thicknesses from outside to inside (cm)	Total Thicknesses (cm)	Dose received after 1 hour of radiation (rad)
1	Al:0.25 – PE:1.30 – Al: 0.20	1.75	1.6×10^3
2	PE:0.30 - Pb: 0.40 - PE: 0.30 Al: 0.20	1.20	1.1×10^3
3	Al: 0.25 - Pb: 0.40 - PE: 0.70	1.35	3.8×10^3
4	Al: 0.25 - Pb: 0.40 - PE: 0.30 - Al: 0.20	1.15	1.7×10^3
5	Al: 0.25 – Pb: 0.40 - PE: 0.30 – Al: 0.25	1.20	2.2×10^3
6	PE: 0.30 – Pb: 0.40 – PE: 0.30	1.00	9.7×10^2
7	Al: 0.25 - PE: 0.30 - Pb: 0.40 - PE: 0.25	1.20	1.4×10^3
8	Al: 0.25 - Pb: 0.40 - PE: 0.40	1.05	1.7×10^3
9	Al: 1.00 - PE: 1.30 - Al: 0.20	2.50	1.8×10^3
10	Al: 0.25 - Pb: 0.40 - PE: 0.60 - Al: 0.20	1.45	3.2×10^3
11	Al: 0.50 - Pb: 0.40 - PE: 0.30 - Al: 0.20	1.40	2.6×10^3
12	Al: 0.25 - Pb: 0.80 - PE: 0.30 - Al: 0.20	1.55	2.2×10^3
13	Al: 0.25 - Pb: 0.40 - PE: 0.50 - Al: 0.20	1.35	3.7×10^3
14	Al: 0.25 - Pb: 0.40 - PE: 0.30 - Al: 0.20	1.15	1.9×10^3
15	Al: 0.25 - PE: 0.50 - Pb: 0.40 - PE: 0.30 - Al: 0.20	1.65	1.3×10^3

While Table 4.4 gives the total received dose in the target area when the beam is on per one hour, the detectors and electronics spend approximately only three to five minutes in the beam. Therefore, the electronics will receive less dose than those given in the Table 4.4 where 15 different sandwiches were studied. In the second and sixth options, prompt doses are lower than the others, but the outmost polyethylene layer can undergo mechanical deformation due to its low melting temperature. The seventh and the eighth options were selected for the shielding of TimePix3 pixel and diamond electronics respectively. The other options either result in a higher dose or are thicker. The depth allowed for the shielding of the diamond detector electronics is less than that of the pixel detector, so its shielding thickness was chosen to be less than the pixel

detector's shielding. In Figure 4.7, unshielded and shielded pixel detector electronics are shown and the shielding is Al: 0.25 cm - PE: 0.30 cm - Pb: 0.40 cm - PE: 0.25 cm from the outside to the inside. In Figure 4.8, unshielded and shielded diamond detector electronics are shown and the shielding is Al: 0.25 cm - Pb: 0.40 cm - PE: 0.40 cm from the outside to the inside.

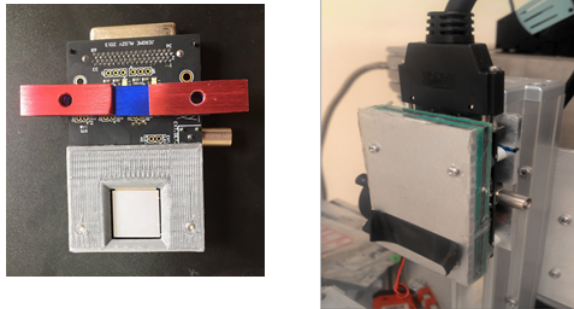


Figure 4.7: Unshielded (left) and shielded (right) pixel detector electronics. The shielding of the detector is Al: 0.25 cm - PE: 0.30 cm - Pb: 0.40 cm - PE: 0.25 cm from the outside to the inside. Aluminum is light grey, polyethylene is green and lead is dark grey in this photo. The detector hole was covered with duct tape here to keep it clean during assembly.



Figure 4.8: Unshielded (left) and shielded (right) diamond detector. The shielding of the detector is Al: 0.25 cm - Pb: 0.40 cm - PE: 0.40 cm from the outside to the inside. Lead and polyethylene layers are embedded inside the light grey aluminum casing. The round detector hole corresponding to the 5.9 mm diameter diamond detector is also visible.

Electronic readout of fiber scintillators

Electronic readout components of fiber scintillators were shielded to protect them from the radiation damage. As shown in Figure 4.6, two separate units of fiber scintillators scan the beam vertically and horizontally. After scanning the target area, they return to their parking positions. Each of them remain in the target region for approximately three to five minutes similar to the pixel and diamond detectors. Dose calculations for these readout components were conducted where they are directly exposed to the beam. The scintillator readout that moves along the x axis receives a higher dose than the others according to simulations and the rest of the shielding studies were performed for this scintillator. In Table 4.5, shielding studies are shown for their electronic components. Four different designs were tried.

Table 4.5: Shielding studies for the electronic readout components of fiber scintillators. 4 different shielding thicknesses and doses received after one hour of exposure are seen.

No	Shield Thicknesses from outside to inside (cm)	Dose received after 1 hour of radiation (rad)
1	Al: 0.50 - PE: 0.50	2.2×10^3
2	Al:0.20 - PE: 0.20 - Pb: 0.50 - PE: 0.20	6.8×10^2
3	Al: 0.25 - Pb: 0.40 - PE: 0.20	2.9×10^3
4	Al:0.20 - PE: 0.20 - Pb: 0.40 - PE: 0.20	1.1×10^3

Second option has the lowest received dose due to its thick lead layer. However, the thickness restriction is strict (<1 cm) for the shielding of these electronics. The, Al:0.20 cm - PE: 0.20 cm - Pb: 0.40 cm - PE: 0.20 cm option was preferred, which lowers the received dose while being inside the thickness limit. The unshielded and shielded fiber scintillator readout electronics are shown in Figure 4.9.



Figure 4.9: Unshielded (left) and shielded (right) lower fiber scintillator readout. Aluminum is grey and polyethylene is green on this photo. Lead layer is not seen because it is inside.

Shielding of the readout of the pixel detector

While the pixel detector scans the target area to measure the flux of the beam, the readout box of the pixel detector stays about 20.0 cm away from the center of the target area. This readout box transmits the data via 3.0 m long USB 3.0 cable from the pixel detector to the mini-computer in the R&D room, was shielded to protect against exposure to radiation. The calculations are performed for when it is closest to the beam spot. A structure consisting of Al: 0.25 cm - PE: 1.00 cm from the outside to the inside was tried for the shielding of the readout of the pixel detector and the calculated dose is indistinguishable from 0 with high statistics. Unshielded and shielded readout of the pixel detector are shown in Figure 4.10.



Figure 4.10: Unshielded (left) and shielded (right) readout of the pixel detector. Shielding consist of Al: 0.25 cm - PE: 1.00 cm from the outside to the inside. Aluminum layer is outside facing the beam (grey) and the polyethylene layer is behind it (green).

Shielding of the Step Motor

A step motor is in charge of moving both the diamond detector and the device under test. It is exposed to primary and secondary radiation and so, shielding studies were carried out for this motor. Two shielding designs were tried and the doses received by the motor during an irradiation of one hour are shown in Table 4.6.

Table 4.6: Shielding studies for the step motor. Shielding thicknesses and the corresponding received doses during an irradiation of one hour.

No	Shield thicknesses from outside to inside (cm)	Dose received after 1 hour of radiation (rad)
1	Al: 0.25 - PE: 0.50	1.1×10^3
2	Al: 0.50 - PE: 0.25	6.7×10^2

Second design was selected as the shielding of the step motor. The motor stops approximately three to five minutes in an intense radiation area and then it returns to its parking position. The received dose in its park position is quite low. Therefore, this

shielding is considered sufficient for the step motor. Only one side of the step motor which looks towards the beam was shielded with aluminum because the received dose is very low. Unshielded and shielded step motor are shown in Figure 4.11. Aluminum is grey in this photo and the white polyethylene layer is behind it.

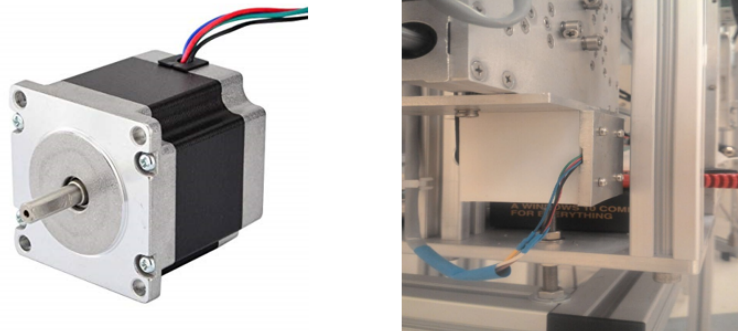


Figure 4.11: The unshielded (left) and shielded (right) step motor. Aluminum is grey in this photo and the white polyethylene layer is behind it.

Shielding of the electronic components of the mobile radiation measurement robot

A mobile radiation measurement robot will navigate in the R&D room and record the dose on a Geiger counter at pre-determined steps, producing a radiation map. The electronics of the robot, which is exposed to secondary radiation, needs to be shielded. The most intense radiation area, which is close to the shielded adjustable conic collimator, was chosen for running these shielding studies. The doses received in one hour by the electronics of mobile radiation robot with various shielding options are shown in Table 4.7.

Table 4.7: Shielding studies for the mobile radiation monitor. Shielding thicknesses and received doses in one hour by the electronics of mobile radiation robot are shown.

No	Shield thicknesses from outside to inside (cm)	Dose received after 1 hour of radiation (rad)
1	Al:0.25 - PE: 1.00	2.4×10^2
2	Al:0.50 - PE :0.50	7.2×10^2

The minimum dose is obtained from first choice, which is Al:0.25 cm - PE: 1.00 cm from the outside to the inside so it was selected as the shielding of the electronic components of the mobile radiation measurement robot.

Shielding of the Electronic Components of the Cooling Subsystem

Electronic components of the cooling subsystem were shielded to protect them from radiation damage. This subsystem has 22 manifolds with attached thermocouples to monitor temperature. Half of them distribute cold input water, controlled by flow meters and pressures gauges. While the rest carry warm return water. The position of the cooling subsystem is seen in Figure 4.12 and has a size of 200 cm x 180 cm x 60 cm. An additional requirement for the shielding of its electronics is that it should be easily movable so that the cooling subsystem remains accessible. Since the size of the subsystem that should be protected is rather large, the shield should be as light as possible and be movable on wheels.

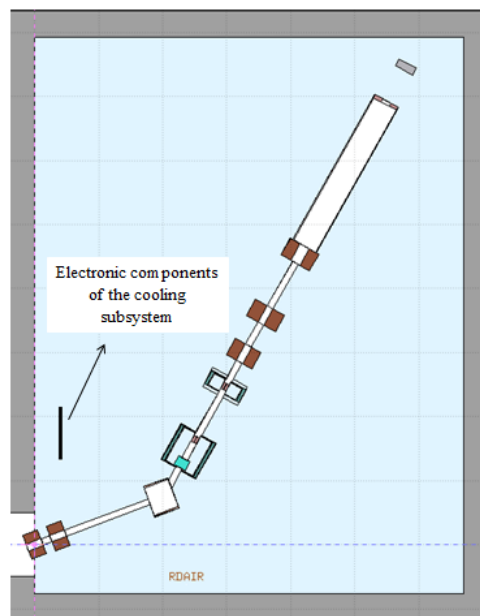


Figure 4.12: The position of the cooling subsystem is shown in FLAIR, the visual interface of FLUKA. Electronics are near the left wall above the cooling connections from the Technical Room.

Shielding studies were conducted for the electronics placed at the indicated position and various shielding options were tried. In Table 4.8, shielding sandwiches and the doses received on the electronic components of the cooling subsystem are shown.

Table 4.8: Shielding studies for the electronic components of the cooling subsystem. Shielding sandwiches and the doses received on the electronic components of the cooling subsystem are shown.

No	Shield Thicknesses from outside to inside (cm)	Dose received after 1 hour of radiation (rad)
1	Al: 1.00 - Pb: 1.00 - PE: 1.00 - Pb: 1.00 - Al: 0.50	1.9×10^2
2	Al: 1.00 - Pb: 1.00 - PE: 2.00 - Al: 0.25	1.2×10^2
3	Al: 1.00 - Pb: 0.50 - PE: 2.00 - Al: 0.25	2.9×10^2
4	Al: 0.50 - Pb: 0.40 - PE: 1.00 - Al: 0.25	1.4×10^2
5	Al: 1.00 - Pb: 1.00 - PE: 1.00 - Al: 0.25	1.9×10^2

Second option has the lowest dose, but this design is very thick therefore, it has a high cost and also a large weight. First option is the thickest, but the received dose is higher than the others because increasing the lead thickness too much also increases the number of secondary particles. Therefore, the optimum choice is the fourth option, Al: 0.50 cm - Pb: 0.40 cm - PE: 1.00 cm - Al: 0.25 cm from the outside to the inside, which was selected for production. The final design consists of four panels that are on platforms with four wheels each. In Figure 4.13, unshielded and shielded subsystem is shown from similar angles. At the top of the cooling subsystem, the upper part of a PLC is seen and it is shown with a red circle. Shielding studies were also performed for these electronics and will be presented in the next section.



Figure 4.13: Unshielded (above) and shielded (below) cooling subsystem. The shield consists of Al: 0.50 cm - Pb: 0.40 cm - PE: 1.00 cm - Al: 0.25 cm from the outside to the inside and is movable on wheels.

Shielding of the Cooling PLC (Programmable Logical Controller)

A PLC is in charge of the control and communication of the cooling subsystem with the control subsystem. While the PLC is far from the target area and receives less dose than other components, a rare Single Event Effect can upset the electronics. Therefore, shielding studies were carried out for this PLC. PE: 0.5 cm - Al: 0.1 cm was selected as a shielding of PLC. Unshielded and shielded PLC are seen in Figure 4.14. On 24 November 2017, this PLC failed during an irradiation because it did not have sufficient shielding for its top part which protrudes out of the shielding of the cooling subsystem. In addition, 5 cm of polyethylene was added to the top part of the PLC and it is shown with a red circle.



Figure 4.14: Unshielded (left) and shielded (right) Programmable Logical Controller. Shielding inside the hinged door consists of PE: 0.5 cm - Al: 0.1 cm from the outside to the inside. In addition, a 5 cm thick polyethylene was used to cover the top part of the PLC and it is shown with red circle.

Shielding of the Turbomolecular Pump in the Vacuum Subsystem

If protons from the cyclotron did not travel in a good vacuum, they would scatter and lose their energy. A turbomolecular and mechanical vacuum pump ensures that the vacuum inside the METU-DBL beam pipes is better than 10^{-5} torr. The electronic components of the turbomolecular vacuum pump were shielded to avoid radiation damage. The position of electronics of the turbomolecular pump is shown in Figure 4.15. This pump has a 23.5 cm length and its radius is 10.0 cm. Shielding studies were carried out for the electronic components of the turbomolecular vacuum pump. Shielding trials and their results are shown in Table 4.9.

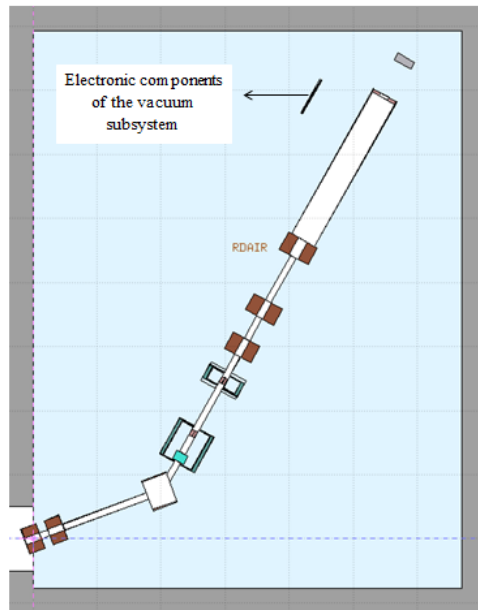


Figure 4.15: The position of the turbomolecular pump in the vacuum subsystem is shown in FLAIR, the visual interface of FLUKA. It is placed close to the vacuum connection in the middle of the 25 cm-radius beam pipe.

Table 4.9: Shielding studies for the electronic components in the vacuum subsystem. Shielding thicknesses and received doses are shown.

No	Shield thicknesses from outside to inside (cm)	Dose received after 1 hour of radiation (rad)
1	Al: 0.25 - Pb: 0.20 - PE: 1.00 - Al: 0.25	3.5×10^{-2}
2	Al: 0.25 - PE: 1.00 - Pb: 0.20 - Al: 0.25	4.2×10^{-2}
3	Al: 0.25 - Pb: 0.20 - PE: 0.50 - Al: 0.25	1.0×10^1
4	Al: 0.25 - PE: 0.50 - Pb: 0.20 - PE: 0.50 - Al: 0.25	3.9×10^0

The first option was selected since it results in the lowest received dose. The shield consists of two symmetrical mechanical halves joined by hinges and movable on wheels. The turbomolecular pump (upper panel), connected to the beam pipe with a 1.5 m long and 100 mm wide flex pipe during pretests, and with its shield during the final assembly of METU-DBL (lower panel) are shown in Figure 4.16

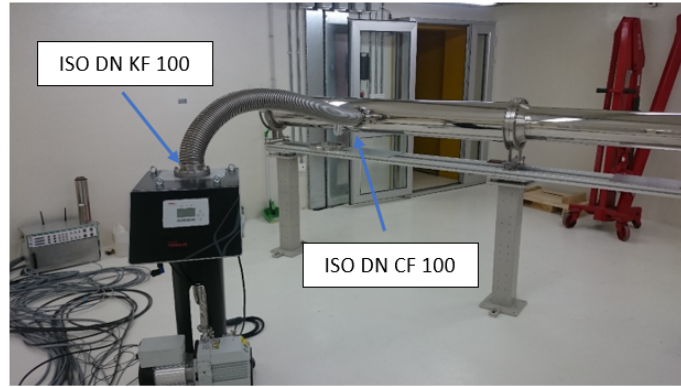


Figure 4.16: The turbomolecular pump (upper panel), connected to the beam pipe with a 1.5 m long and 100 mm wide flex pipe during pretests, and with its shield during the final assembly of METU-DBL (lower panel).

While one turbomolecular pump was used during the pretests, two turbomolecular pumps are needed for the final setup. Same shielding materials and thicknesses were used for both assemblies, but the geometry is modified. The final shielding box has a size of 61.0 cm x 59.0 cm x 102.5 cm. In Figure 4.17, the shielding for the second turbomolecular pump is shown from two different angles.



Figure 4.17: The shielding of the second turbomolecular pump from two different angles. The shielding box has a size of 61.0 cm x 59.0 cm x 102.5 cm.

Shielding of the Electronic Components of the Control Subsystem

Electronic components of the control subsystem were shielded to protect them from radiation damage. For this purpose, the electronic components were placed in the FLUKA at the locations are shown in Figure 4.18, close to the entrance of the R&D room. Electronics are near the right wall, close to the entrance of the R&D room. Received doses of the electronic components of the control subsystem were calculated using FLUKA. Various shielding options were studied for these components and they are given in Table 4.10.

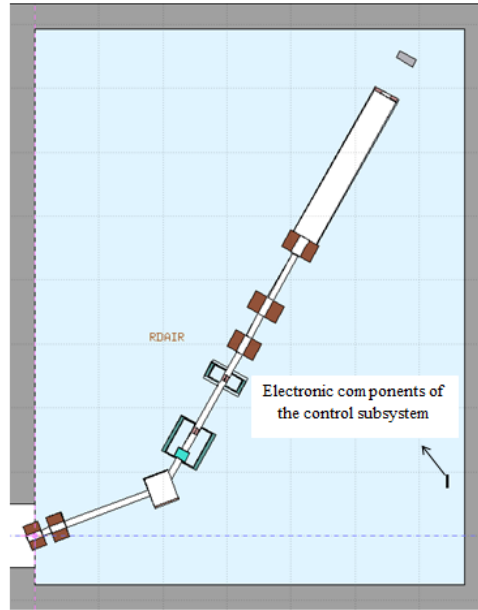


Figure 4.18: Position of the electronic components of the control subsystem in FLAIR, the visual interface of FLUKA is shown. Electronics are near the right wall, close to the entrance of the R&D room.

Table 4.10: Shielding studies for the electronic components in the control subsystem. Various shielding thicknesses and received doses after one hour of irradiation are given.

No	Shield thicknesses from outside to inside (cm)	Dose received after 1 hour of radiation (rad)
1	Al: 0.25 - PE: 0.50 - Al:0.25	1.4×10^{-1}
2	PE: 0.50	2.1×10^{-1}
3	Al: 0.50 cm - PE: 0.50	1.2×10^{-1}

Three shielding designs were studied. The minimum dose is obtained from third design, but inner layer should be aluminum due to the mechanical requirements. Therefore, first choice was selected for these electronics. The back side of the shielding is protected by the wall and this part is left open for cooling purposes. Two images from the front (upper panel) and one image from the back (lower panel) of the electronics box of control subsystem are shown in Figure 4.19. The shielded hinged door covers

the network switch (black), which in the charge of the communication of the wired network devices in the irradiation room and the control room.



Figure 4.19: Two images from the front (upper panel) and one image from the back (lower panel) of the electronics box of control subsystem are shown. Shielding is Al: 0.50 cm - PE: 1.00 cm from the outside to the inside [108].

4.2 Radioprotection Studies

Radioprotection studies were performed for the safety of the radiation workers and long-term sustainability of the METU-DBL. In this section, radioisotope studies, activation and cooling time studies for METU-DBL will be presented. Activation of isotopes have a threshold of about ≈ 6 MeV [109]. While for TID tests performed with 3.1 MeV gammas from Co-60 do not produce radioisotopes SEE tests which are performed between 20-200 MeV proton energy necessarily produces radioisotopes. Therefore all materials and electronics which will be tested must undergo a radioisotope study to ensure reasonable extraction times for the tested samples.

4.2.1 Radioisotope Studies

Numerous radioisotope studies were conducted for various purposes. Shieldings of some components and beam elements may be activated over time due to repetitive irradiations and so radioisotope studies are important to understand the activation levels of components. For all activation studies in this chapter, the following convention will be followed. Half lives higher than 1 year are shown in red, while those higher than 1 day are in orange and those higher than 1 hour are in green. The lists are always given in order of atomic number from the biggest to the smallest and the results are given for 1 second after a 1 hour irradiation is finished.

First work was performed for the activation of lead shielding layers for two different cases. In the first case, the lead layer is behind 0.25 cm of pure aluminum, while in the second case, 0.50 cm of aluminum. The range of 30 MeV protons in aluminum is approximately 0.43 cm [110]. While 30 MeV protons reach the lead in the first case, in the second case, protons do not reach the lead layer due to the thickness of the aluminum. The activation levels of lead layers for each of these cases were performed. When the protons hit lead nuclei, many radioisotopes can emerge and this effects the total dose level in the R&D room. The activation of lead is higher for the first case as expected. In Table 4.11, radioisotopes that arise from a 0.25 cm thick lead layer that is behind a pure aluminum layer of thickness 0.25 cm, 1 second after an irradiation of 1 hour is finished are shown. In Table 4.12, radioisotopes emerge from lead layer that behind aluminum with a thickness of 0.50 cm are shown. The number of isotopes arising from the lead layer decreased when the aluminum layer was increased. When the thickness of aluminum increases, protons can not penetrate into the lead layer and only secondary particles reach the lead.

Table 4.11: Radioisotope studies for the lead layer behind the aluminum with a thickness of 0.25 cm. Activation values and radioisotopes taken from the FLUKA are seen. Decay mode, half life and the decay product of the related radioisotopes are shown.

Isotope	Activity (Bq/cm ³)	Decay Mode	Half Life	Decay Product
²⁰⁸ Bi	8.8x10 ⁻⁵	β^+	3.7x10 ⁵ y	²⁰⁸ Pb
²⁰⁷ Bi	6.0x10 ⁰	β^+	32.9 y	²⁰⁷ Pb
²⁰⁶ Bi	6.4x10 ³	β^+	6.2 d	²⁰⁶ Pb
²⁰⁵ Pb	5.2x10 ⁻⁹	EC	15.3x10 ⁶ y	²⁰⁵ Tl
²⁰⁵ Bi	2.0x10 ³	β^+	15.3 d	²⁰⁵ Pb
²⁰⁴ Bi	1.5x10 ³	β^+	11.2 h	²⁰⁴ Pb
²⁰³ Pb	9.6x10 ⁰	EC	2.2 d	²⁰³ Tl
²⁰³ Bi	1.4x10 ³	β^+	11.8 h	²⁰³ Pb
¹⁹⁹ Tl	6.4x10 ⁻⁶	β^+	7.4 h	¹⁹⁹ Hg

Table 4.12: Radioisotope studies for the lead layer behind the aluminum with a thickness of 0.50 cm. Calculated activation values and radioisotopes from the FLUKA are seen. Decay mode, half life and the decay product of the related radioisotopes are shown.

Isotope	Activity (Bq/cm ³)	Decay Mode	Half Life	Decay Product
²⁰⁵ Pb	1.3x10 ⁻⁷	EC	15.3x10 ⁶ y	²⁰⁵ Tl

Additionally, radioisotope studies were conducted for the various materials considered for the first protective collimator. In Table 4.13, radioisotope studies of Al6082, Al6061, Al7075 and Al7050 considered for the first protective collimator are shown. Al6082 gives better results than the other aluminum series. It mostly results in isotopes with short half lives and those with long half lives generally have lower activities than others. Al7075 and Al7050 produces many isotopes. Some of them have long half lives and some even have high activities. These are not suitable materials for the first collimator. Isotopes coming from Al6061 is similar to Al6082 but, there are more long half life isotopes than Al6082.

Table 4.13: Radioisotope studies of Al6082, Al6061, Al7075 and Al7050 considered for the first protective collimator. Emerged radioisotopes and their activities are seen.

Isotope	Activity (6082) (Bq/cm ³)	Activity (6061) (Bq/cm ³)	Activity (7075) (Bq/cm ³)	Activity (7050) (Bq/cm ³)	Half Life	Decay Mode	Decay Product
¹¹⁹ Sb	-	-	2.3x10 ⁻⁷	-	1.6 d	EC	¹¹⁹ Sn
¹¹⁸ Sb	-	-	6.2x10 ⁴	-	3.6 min	β ⁺	¹¹⁸ Sn
¹¹⁷ Sb	-	-	4.1x10 ⁴	-	2.8 h	β ⁺	¹¹⁷ Sn
⁹⁵ Nb	-	-	-	2.6x10 ¹	35.0 d	β ⁻	⁹⁵ Mo
⁹⁴ Nb	-	-	-	2.3x10 ⁰	2.0x10 ⁴ y	β ⁻	⁹⁴ Mo
⁹¹ Nb	-	-	-	1.8x10 ⁻²	6.8x10 ² y	β ⁺	⁹¹ Zr
⁹⁰ Nb	-	-	-	1.2x10 ¹⁰	14.6 h	β ⁺	⁹⁰ Zr
⁸⁹ Nb	-	-	-	1.9x10 ⁸	2.0 h	β ⁺	⁸⁹ Zr
⁸⁹⁽¹⁾ Zr	-	-	-	1.2x10 ⁷	3.3 d	β ⁺	⁸⁹ Y
⁶⁹ Zn	-	-	1.7x10 ⁴	-	56.4 min	β ⁻	⁶⁹ Ga
⁶⁸ Ga	2.9x10 ⁴	2.9x10 ⁴	5.5x10 ⁵	6.6x10 ⁹	1.1 h	β ⁺	⁶⁸ Zn
⁶⁷ Cu	-	-	7.0x10 ²	-	2.6 d	β ⁻	⁶⁷ Zn
⁶⁷ Ga	1.1x10 ³	-	1.9x10 ⁴	2.0x10 ⁸	3.3 d	EC	⁶⁷ Zn
⁶⁶ Ga	-	8.8x10 ³	1.5x10 ⁵	1.4x10 ⁹	3.9 d	β ⁺	⁶⁶ Zn
⁶⁵ Zn	-	1.5x10 ¹	3.4x10 ²	4.7x10 ⁶	243.7 d	β ⁺	⁶⁵ Cu
⁶⁵ Ga	-	-	-	5.8x10 ⁹	15.2 min	β ⁺	⁶⁵ Zn
⁶⁴ Cu	-	1.3x10 ⁴	6.0x10 ⁴	5.0x10 ⁸	12.7 h	β ⁺ , β ⁻	⁶⁴ Ni, ⁶⁴ Zn
⁶⁴ Ga	-	-	3.7x10 ⁵	8.7x10 ⁹	2.6 min	β ⁺	⁶⁴ Zn
⁶³ Ga	-	-	6.1x10 ⁴	6.1x10 ⁸	32.4 s	β ⁺	⁶³ Zn
⁶³ Zn	8.3x10 ⁴	2.5x10 ⁵	3.0x10 ⁶	2.8x10 ¹⁰	38.5 min	β ⁺	⁶³ Cu
⁶³ Ni	-	-	-	9.9x10 ⁻²	101.2 y	β ⁻	⁶³ Cu
⁶² Cu	6.2x10 ⁴	2.5x10 ⁵	3.5x10 ⁶	4.2x10 ¹⁰	9.7 min	β ⁺	⁶² Ni
⁶² Zn	-	4.5x10 ⁵	1.8x10 ⁴	3.6x10 ⁸	9.2 h	β ⁺	⁶² Cu
⁶¹ Cu	-	2.3x10 ⁴	2.2x10 ⁵	2.2x10 ⁹	3.3 h	β ⁺	⁶¹ Ni
⁶¹ Co	-	-	-	2.1x10 ⁸	1.6 h	β ⁻	⁶¹ Ni
⁶⁰ Cu	1.0x10 ⁵	5.2x10 ⁴	5.7x10 ⁵	5.2x10 ⁹	23.7 min	β ⁺	⁶⁰ Ni
⁵⁹ Ni	6.5x10 ⁻⁵	1.3x10 ⁻⁴	7.8x10 ⁻⁴	2.3x10 ⁻³	7.6x10 ⁴ y	EC	⁵⁹ Co
⁵⁸ Co	-	-	1.3x10 ¹	-	70.9 d	β ⁺	⁵⁸ Fe
⁵⁷ Co	-	-	1.3x10 ¹	1.3x10 ³	271.7 d	EC	⁵⁷ Fe

Continued on next page

Table 4.13 : continued from previous page

Isotope	Activity (6082)	Activity (6061)	Activity (7075)	Activity (7050)	Half Life	Decay Mode	Decay Product
⁵⁶ Co	1.2x10 ²	1.9x10 ²	2.6x10 ²	9.3x10 ¹	77.2 d	β ⁺	⁵⁶ Fe
⁵⁵ Fe	-	6.2x10 ¹	4.0x10 ¹	1.4x10 ¹	2.7 y	EC	⁵⁵ Mn
⁵⁵ Co	4.8x10 ³	2.4x10 ³	-	-	17.5 h	β ⁺	⁵⁵ Fe
⁵⁴ Mn	1.1x10 ²	1.7x10 ¹	8.0x10 ¹	2.9x10 ¹	312.2 d	EC	⁵⁴ Cr
⁵³ Mn	5.3x10 ⁻⁶	5.3x10 ⁻⁶	6.6x10 ⁻⁶	4.0x10 ⁻²	3.7x10 ⁶ y	EC	⁵³ Cr
⁵² Mn	8.1x10 ²	9.8x10 ²	6.5x10 ²	1.3x10 ⁷	5.6 d	β ⁺	⁵² Cr
⁵¹ Mn	-	7.4x10 ⁴	-	3.7x10 ⁸	46.2 min	β ⁺	⁵¹ Cr
⁵¹ Cr	6.5x10 ²	7.6x10 ²	8.5x10 ²	1.1x10 ⁷	27.7 d	EC	⁵¹ V
⁴⁹ V	-	5.3x10 ⁰	-	5.3x10 ⁰	330.0 d	EC	⁴⁹ Ti
⁴⁸ V	1.1x10 ²	2.3x10 ²	-	9.0x10 ⁶	15.9 d	β ⁺	⁴⁸ Ti
⁴⁷ V	4.5x10 ⁴	-	-	9.0x10 ⁸	32.6 min	β ⁺	⁴⁷ Ti
⁴⁶ Sc	-	-	-	4.3x10 ¹	83.8 d	β ⁻	⁴⁶ Ti
⁴⁶ V	-	-	-	2.4x10 ⁸	422.5 ms	β ⁺	⁴⁶ Ti
⁴⁵ Ti	-	-	-	2.5x10 ⁸	3.1 h	β ⁺	⁴⁵ Sc
⁴⁴⁽¹⁾ Sc	3.7x10 ²	5.1x10 ³	-	2.0x10 ⁸	2.0 d	IT	⁴⁴ Sc
⁴³ Sc	-	-	-	1.0x10 ⁸	3.9 h	β ⁺	⁴³ Ca
³⁰ P	-	6.2x10 ⁴	6.2x10 ⁴	1.2x10 ⁹	2.5 min	β ⁺	³⁰ Si
²⁸ P	4.8x10 ³	-	4.8x10 ³	-	270.3 ms	β ⁺	²⁸ Si
²⁸ Al	2.5x10 ⁵	2.5x10 ⁵	4.4x10 ⁵	5.6x10 ⁹	2.2 min	β ⁻	²⁸ Si
²⁷ Al	4.2x10 ⁴	-	4.2x10 ⁴	-	-	-	Stable
²⁷ Si	4.4x10 ⁷	4.6x10 ⁷	4.2x10 ⁷	4.0x10 ¹¹	4.2 s	β ⁺	²⁷ Al
²⁷ Mg	1.0x10 ⁶	1.2x10 ⁶	7.4x10 ⁵	1.3x10 ¹⁰	9.5 min	β ⁻	²⁷ Al
²⁶ Al	8.3x10 ⁻³	8.6x10 ⁻³	-	-	7.2x10 ⁵ y	β ⁺	²⁶ Mg
²⁶ Si	2.7x10 ⁵	2.8x10 ⁵	1.4x10 ⁵	4.1x10 ⁹	2.2 s	β ⁺	²⁶ Al
²⁵ Al	4.5x10 ⁵	4.0x10 ⁵	4.0x10 ⁵	2.8x10 ⁹	7.2 s	β ⁺	²⁵ Mg
²⁵ Na	-	-	6.2x10 ⁴	-	59.1 s	β ⁻	²⁵ Mg
²⁴ Al	-	-	-	1.7x10 ⁹	2.1 s	β ⁺	²⁴ Mg
²⁴ Na	5.1x10 ⁴	4.8x10 ⁴	3.4x10 ⁴	2.6x10 ⁸	14.9 h	β ⁻	²⁴ Mg
²³ Mg	3.6x10 ⁶	4.0x10 ⁶	3.1x10 ⁶	3.8x10 ¹⁰	11.3 s	β ⁺	²³ Na
²² Na	-	1.1x10 ¹	1.3x10 ¹	1.9x10 ¹	2.6 y	β ⁺	²² Ne
²¹ Na	-	-	1.2x10 ⁵	2.4x10 ⁹	22.5 s	β ⁺	²¹ Ne
¹⁸ F	-	-	2.0x10 ⁴	-	1.8 h	β ⁺	¹⁸ O

Continued on next page

Table 4.13 : continued from previous page

Isotope	Activity (6082)	Activity (6061)	Activity (7075)	Activity (7050)	Half Life	Decay Mode	Decay Product
¹⁷ F	-	-	-	6.2x10 ⁸	1.1 min	β ⁺	¹⁷ O
³ H	3.6x10 ⁰	2.4x10 ⁰	4.0x10 ⁰	2.8x10 ⁰	12.3 y	β ⁻	³ He

After the aluminum series, 304, 316 SS and iron were also studied. In Table 4.14, radioisotope studies of these materials considered for the first protective collimator are shown. Irradiation of 304 and 316 SS produces high activity isotopes. Iron produces fewer radioisotopes and their activities not so high and their half lives are short. However, pure iron is not appropriate due to its potential physical deformations like corrosion and production of rust.

Table 4.14: Radioisotope studies of 304, 316 SS and iron considered for the first protective collimator. Emerged radioisotopes and their activities are seen.

Isotope	Activity (Bq/cm ³) (304)	Activity (Bq/cm ³) (316)	Activity (Bq/cm ³) (Iron)	Half Life	Decay Mode	Decay Product
⁶⁴ Cu	3.3x10 ³	-	-	12.7 h	β ⁺ , β ⁻	⁵⁴ Ni, ⁵⁴ Zn
⁶³ Ni	2.4x10 ⁻¹	-	-	101.2 y	β ⁻	⁶³ Cu
⁶² Cu	6.2x10 ⁵	9.8x10 ⁵	-	9.7 min	β ⁺	⁶² Ni
⁶¹ Cu	9.4x10 ⁴	7.0x10 ⁴	-	3.3 h	β ⁺	⁶¹ Ni
⁶⁰ Cu	1.6x10 ⁶	1.1x10 ⁶	-	23.7 min	β ⁺	⁶⁰ Ni
⁵⁹ Fe	-	-	4.1x10 ¹	44.5 d	β ⁻	⁵⁹ Co
⁵⁹ Ni	6.4x10 ⁻¹	7.2x10 ⁻³	-	7.6x10 ⁴ y	EC	⁵⁹ Co
⁵⁸ Cu	9.1x10 ⁵	7.0x10 ⁵	-	3.2 s	β ⁺	⁵⁸ Ni
⁵⁸ Co	3.2x10 ²	5.5x10 ²	5.3x10 ⁻¹	70.9 d	β ⁺	⁵⁸ Fe
⁵⁷ Co	2.0x10 ³	2.2x10 ³	2.1x10 ²	271.7 d	EC	⁵⁷ Fe
⁵⁷ Ni	9.3x10 ⁴	9.5x10 ⁴	-	1.5 d	β ⁺	⁵⁷ Co
⁵⁶ Co	2.9x10 ⁴	3.0x10 ⁴	4.4x10 ⁴	77.2 d	β ⁺	⁵⁶ Fe
⁵⁶ Mn	2.8x10 ⁵	3.2x10 ⁵	2.2x10 ⁵	2.6 h	β ⁻	⁵⁶ Fe

Continued on next page

Table 4.14 : continued from previous page

Isotope	Activity (Bq/cm ³) (304)	Activity (Bq/cm ³) (316)	Activity (Bq/cm ³) (Iron)	Half Life	Decay Mode	Decay Product
⁵⁵ Co	5.0x10 ⁵	4.8x10 ⁵	7.3x10 ⁵	17.5 h	β^+	⁵⁵ Fe
⁵⁵ Fe	5.7x10 ³	5.7x10 ³	8.3x10 ³	2.7 y	EC	⁵⁵ Mn
⁵⁴ Mn	5.7x10 ²	5.9x10 ²	3.0x10 ²	312.2 d	EC	⁵⁴ Cr
⁵⁴ Co	1.6x10 ⁴	1.1x10 ⁴	2.1x10 ⁴	193.3 ms	β^+	⁵⁴ Fe
⁵³ Fe	3.8x10 ⁶	5.1x10 ⁶	5.4x10 ⁶	8.5 min	β^+	⁵³ Mn
⁵³ Mn	4.3x10 ⁻⁴	4.5x10 ⁻⁴	5.3x10 ⁻⁴	3.7x10 ⁶ y	EC	⁵³ Cr
⁵² V	3.1x10 ⁵	1.9x10 ⁵	-	3.7 min	β^-	⁵² Cr
⁵² Mn	9.0x10 ⁴	8.3x10 ⁴	3.3x10 ⁴	5.6 d	β^+	⁵² Cr
⁵¹ Cr	5.3x10 ⁴	4.7x10 ⁴	3.5x10 ²	27.7 d	EC	⁵¹ V
⁵¹ Mn	3.9x10 ⁶	4.3x10 ⁶	1.5x10 ⁵	46.2 min	β^+	⁵¹ Cr
⁵⁰ Mn	2.4x10 ⁴	-	-	283.2 ms	β^+	⁵⁰ Cr
⁴⁹ V	3.2x10 ²	3.4x10 ²	-	330 d	EC	⁴⁹ Ti
⁴⁹ Cr	1.0x10 ⁶	1.2x10 ⁶	-	42.3 min	β^+	⁴⁹ V
⁴⁸ V	3.4x10 ³	4.9x10 ³	-	16.0 d	β^+	⁴⁸ Ti
⁴⁸ Cr	2.0x10 ³	-	-	21.6 h	β^+	⁴⁸ V
⁴⁷ V	9.0x10 ⁴	4.5x10 ⁴	-	32.6 min	β^+	⁴⁷ Ti
⁴⁶ V	-	-	5.3x10 ⁰	422.5 ms	β^+	⁴⁶ Ti
³¹ S	4.8x10 ⁴	-	-	2.6 s	β^+	³¹ P
³⁰ P	1.2x10 ⁵	6.2x10 ⁴	-	2.5 min	β^+	³⁰ Si
²⁹ P	1.6x10 ⁵	-	-	4.1 s	β^+	²⁹ Si
²⁸ Al	-	1.2x10 ⁵	-	2.2 min	β^-	²⁸ Si
²⁷ Si	2.1x10 ⁵	1.6x10 ⁵	-	4.2 s	β^+	²⁷ Al
²⁵ Al	1.1x10 ⁵	5.7x10 ⁴	-	7.2 s	β^+	²⁵ Mg
¹⁴ O	6.2x10 ⁴	-	-	1.2 min	β^+	¹⁴ N
¹³ N	3.1x10 ⁵	-	-	10.0 min	β^+	¹³ C
¹¹ C	1.6x10 ⁵	1.1x10 ⁵	-	20.4 min	β^+	¹¹ B
⁷ Be	3.4x10 ¹	-	-	53.2 d	EC	⁷ Li
³ H	8.0x10 ⁻¹	1.2x10 ⁰	8.0x10 ⁻¹	12.3 y	β^-	³ He

As a another choice, marble which is a clean shielding material easily available in Turkey was tried. In Table 4.15, radioisotope studies of marble considered for the first collimator are shown. Irradiation of marble produces isotopes with long half life with both low and high activities. This material is not suitable due to its machinability and brittleness.

Table 4.15: Radioisotope studies of marble considered for the first protective collimator. Emerged radioisotopes and their activities are seen.

Isotope	Activity (Bq/cm ³)	Half Life	Decay Mode	Decay Product
⁴⁷ Sc	5.4x10 ²	3.3 d	β^-	⁴⁷ Ti
⁴⁴ Sc	9.7x10 ⁴	4.0 h	β^+	⁴⁴ Ca
⁴⁴⁽¹⁾ Sc	7.0x10 ³	2.4 d	<i>IT</i>	⁴⁴ Sc
⁴³ Sc	5.1x10 ⁴	3.9 h	β^+	⁴³ Ca
⁴² Sc	2.3x10 ⁴	680.8 ms	β^+	⁴² Ca
⁴¹ Sc	6.1x10 ⁵	596.3 ms	β^+	⁴¹ Ca
⁴¹ Ca	1.6x10 ⁻³	9.9x10 ⁴ y	<i>EC</i>	⁴¹ K
⁴⁰ K	8.0x10 ⁻⁸	1.2x10 ⁹ y	β^-	⁴⁰ Ca
⁴⁰ Sc	5.6x10 ³	182.3 ms	β^+	⁴⁰ Ca
³⁹ Ca	1.1x10 ⁶	859.6 ms	β^+	³⁹ K
³⁸ K	3.1x10 ⁴	7.6 min	β^+	³⁸ Ar
³⁷ Ar	7.7x10 ²	35.0 d	<i>EC</i>	³⁷ Cl
³⁷ K	4.3x10 ⁵	1.2 s	β^+	³⁷ Ar
³⁶ Cl	1.6x10 ⁻⁵	3.0x10 ⁵ y	β^-	³⁶ Ar
³³ Cl	9.5x10 ⁴	2.5 s	β^+	³³ S
³⁰ P	1.9x10 ⁵	2.5 min	β^+	³⁰ Si
²⁸ P	1.4x10 ⁴	270.3 ms	β^+	²⁸ Si
²⁷ Al	5.6x10 ⁵	-	-	Stable
²⁷ Si	2.6x10 ⁶	4.2 s	β^+	²⁷ Al
²⁶⁽¹⁾ Al	1.7x10 ⁶	6.3 s	β^+	²⁶ Mg
²⁶ Al	2.1x10 ⁻⁴	7.2x10 ⁵ y	β^+	²⁶ Mg
²⁵ Na	1.2x10 ⁵	59.1 s	β^-	²⁵ Mg
²⁵ Al	7.4x10 ⁵	7.2 s	β^+	²⁵ Mg
²⁴ Al	8.4x10 ⁵	2.1 s	β^+	²⁴ Mg
²⁴ Na	1.7x10 ⁴	14.9 h	β^-	²⁴ Mg

Continued on next page

Table 4.15 : continued from previous page

Isotope	Activity (Bq/cm³)	Half Life	Decay Mode	Decay Product
²³ Mg	2.1x10 ⁶	11.3 s	β^+	²³ Na
²² Na	3.2x10 ¹	2.6 y	β^+	²² Ne
²¹ Na	6.1x10 ⁴	22.4 s	β^+	²¹ Ne
¹⁸ F	2.0x10 ⁴	1.8 h	β^+	¹⁸ O
¹⁵ O	1.6x10 ⁷	2.0 min	β^+	¹⁵ N
¹⁴ C	1.7x10 ⁻³	5700.0 y	β^-	¹⁴ N
¹³ N	9.2x10 ⁶	10.0 min	β^+	¹³ C
¹¹ C	1.1x10 ⁶	20.3 min	β^+	¹¹ B
³ H	1.2x10 ⁰	12.3 y	β^-	³ He

After marble, bismuth was also studied as a candidate material for the first protective collimator due to its high atomic mass. In Table 4.16, the results of this study are seen. Irradiation of bismuth mostly results in long half life isotopes. In some cases, their activities are high. Bismuth is not an appropriate option because cooling time will be longer with this material.

Table 4.16: Radioisotope studies of bismuth considered for the first protective collimator. Emerged radioisotopes and their activities are seen.

Isotope	Activity (Bq/cm ³)	Half Life	Decay Mode	Decay Product
²¹⁰ Bi	2.4x10 ²	5.0 d	β^-	²¹⁰ Po
²¹⁰ Po	1.3x10 ⁻¹	138.4 d	α	²⁰⁶ Pb
²⁰⁹ Po	7.3x10 ⁰	125.2 y	α	²⁰⁵ Pb
²⁰⁸ Bi	2.5x10 ⁻³	3.7x10 ⁵ y	β^+	²⁰⁸ Pb
²⁰⁸ Po	4.0x10 ³	2.9 y	α	²⁰⁴ Pb
²⁰⁷ Po	2.0x10 ⁷	5.8 h	β^+	²⁰⁷ Bi
²⁰⁷ Bi	3.0x10 ¹	32.9 y	β^+	²⁰⁷ Pb
²⁰⁶ Po	5.5x10 ⁴	8.8 d	β^+	²⁰⁶ Bi
²⁰⁶ Bi	1.2x10 ²	6.2 d	β^+	²⁰⁶ Pb
²⁰⁶ Tl	1.5x10 ⁻³	4.2 min	β^-	²⁰⁶ Pb
²⁰⁵ Pb	3.2x10 ⁻⁷	1.5x10 ⁻⁷ y	EC	²⁰⁵ Tl
²⁰³ Pb	2.7x10 ¹	2.2 d	EC	²⁰³ Tl
²⁰² Pb	2.2x10 ⁻⁶	5.3x10 ⁻⁴ y	EC	²⁰² Tl
²⁰² Tl	1.8x10 ⁻⁹	12.2 d	β^+	²⁰² Hg

Another interesting material is the titanium. Radioisotope studies of titanium were performed for the first protective collimator because it has high strength and also good corrosion resistance. The results of this study are shown in Table 4.17. Irradiation of titanium also produces long half life isotopes and it has high a cooling time after the irradiation. Therefore, it is not an suitable as a first collimator material.

Table 4.17: Radioisotope studies of titanium considered for the first protective collimators. Emerged radioisotopes and their activities are seen.

Isotope	Activity (Bq/cm ³)	Half Life	Decay Mode	Decay Product
⁴⁹ V	2.0x10 ³	329.0 d	EC	⁴⁹ Ti
⁴⁸ V	2.8x10 ⁵	16.0 d	β^+	⁴⁸ Ti
⁴⁸ Sc	1.9x10 ⁴	1.8 d	β^-	⁴⁸ Ti
⁴⁷ V	3.1x10 ⁷	32.6 min	β^+	⁴⁷ Ti
⁴⁷ Sc	4.6x10 ⁴	3.3 d	β^-	⁴⁷ Ti
⁴⁶ V	9.1x10 ⁵	422.5 ms	β^+	⁴⁶ Ti
⁴⁶ Sc	1.6x10 ³	83.8 d	β^-	⁴⁶ Ti
⁴⁵ Ca	6.6x10 ¹	162.7 d	β^-	⁴⁵ Sc
⁴⁵ Ti	2.5x10 ⁶	3.1 h	β^+	⁴⁵ Sc
⁴⁴ Sc	1.2x10 ⁶	4.0 h	β^+	⁴⁴ Ca
⁴³ Sc	2.4x10 ⁵	4.0 h	β^+	⁴³ Ca
⁴² Sc	3.4x10 ⁴	681.3 ms	β^+	⁴² Ca
⁴⁰ K	5.8x10 ⁻⁸	1.2x10 ⁹ y	β^- , EC	⁴⁰ Ca, ⁴⁰ Ar
³ H	1.6x10 ⁰	12.0 y	β^-	³ He

The last material considered is tungsten due to its robustness and high melting point. In Table 4.18, radioisotope studies of tungsten considered for the first collimator are seen. Irradiation of tungsten mostly results in isotopes that have half life in the order of a day and have high activity. Therefore, it is not a good option as the first collimator material. As a result of these analyses, Al6082 was chosen as a material of first protective collimator for the final design because it has short half life isotopes mostly. In the case of long half life isotopes, their activities are low also the machinability of Al6082 is also convenient. Therefore, this material is suitable for the first protective collimator.

Table 4.18: Radioisotope studies of tungsten considered for the first protective collimators. Emerged radioisotopes and their activities are seen.

Isotope	Activity (Bq/cm ³)	Half Life	Decay Mode	Decay Product
¹⁸⁷ W	4.0x10 ⁵	2.7 h	β^-	¹⁸⁷ Re
¹⁸⁶ Re	8.8x10 ³	3.7 d	β^- , EC	¹⁸⁶ Os, ¹⁸⁶ W
¹⁸⁵ W	3.9x10 ³	75.0 d	β^-	¹⁸⁵ Re
¹⁸⁴ Re	2.0x10 ⁴	38.0 d	β^+	¹⁸⁴ W
¹⁸³ Re	2.7x10 ⁴	70.0 d	EC	¹⁸³ W
¹⁸² Re	4.1x10 ⁵	2.6 d	β^+	¹⁸² W
¹⁸² Ta	1.4x10 ¹	2.0 s	β^+ , α	¹⁸² Hg, ¹⁷⁸ Au
¹⁸¹ Re	2.7x10 ⁶	20.0 h	β^+	¹⁸¹ W
¹⁸¹ W	1.6x10 ³	121.0 d	EC	¹⁸¹ Ta
¹⁸⁰ Re	4.3x10 ⁷	2.4 min	β^+	¹⁸⁰ W
¹⁷⁹ Ta	1.5x10 ¹	270.0 ms	α	¹⁷⁵ Au
¹⁷⁹ Re	9.9x10 ⁵	19.5 min	β^+	¹⁷⁹ W
¹⁷⁹ W	5.0x10 ⁵	37.0 min	β^+	¹⁷⁹ Ta
¹⁷⁸ Re	1.2x10 ⁵	13.2 min	β^+	¹⁷⁸ W
¹⁷⁸ W	2.0x10 ²	21.6 d	EC	¹⁷⁸ Ta
¹⁷⁸ Ta	1.5x10 ²	255.0 ms	α	¹⁷⁴ Au
¹⁷⁷ Ta	3.1x10 ³	2.3 d	β^+	¹⁷⁷ Hf

In addition to analysis of candidate materials of the first protective collimator, radioactivation analysis was also performed for the window of the movable beam screen. Radioisotope studies for borosilicate and sapphire are given in Table 4.19 and Table 4.20 respectively. Irradiation of borosilicate and sapphire windows with a thickness of 4.0 mm and a radius of 10.0 cm were examined in this study. While borosilicate windows have large diameters, sapphire windows are limited in size 10.0 cm. Irradiation of borosilicate results in 4 long lifetime isotopes. The activity of ²²Na and ⁷Be are high, so they can require a long cooling time. Sapphire irradiation creates two long lifetime isotopes, but their activities are low. Therefore, this material is suitable for the window of the movable beam screen.

Table 4.19: Radioisotope studies of borosilicate considered for the window of the movable beam screen. Emerged radioisotopes and their activities are shown.

Isotope	Activity (Bq/cm ³)	Half Life	Decay Mode	Decay Product
³⁰ P	2.5x10 ⁴	2.5 min	β^+	³⁰ Si
²⁹ P	5.3x10 ³	4.1 s	β^+	²⁹ Si
²⁸ Al	1.2x10 ⁴	2.2 min	β^-	²⁸ Si
²⁸ P	2.4x10 ³	270.0 ms	β^+	²⁸ Si
²⁷ Si	9.5x10 ⁴	4.2 s	β^+	²⁷ Al
²⁶ Al	3.3x10 ⁻⁶	7.2x10 ⁻⁵ y	β^+	²⁶ Mg
²⁵ Al	1.7x10 ⁴	7.2 s	β^+	²⁵ Mg
²³ Mg	4.7x10 ⁴	11.3 s	β^+	²³ Na
²² Na	1.9x10 ⁰	2.6 y	β^+	²² Ne
¹⁸ F	3.9x10 ³	1.8 h	β^+	¹⁸ O
¹³ N	1.5x10 ⁵	10.0 min	β^+	¹³ C
¹¹ C	6.5x10 ⁻⁷	20.3 min	β^+	¹¹ B
¹⁰ C	6.0x10 ³	19.3 s	β^+	¹⁰ B
⁷ Be	5.1x10 ¹	53.2 d	EC	⁷ Li
³ H	3.6x10 ⁻¹	12.3 y	β^-	³ He

Table 4.20: Radioisotope studies of sapphire considered for the window of the movable beam screen. Emerged radioisotopes and their activities are shown.

Isotope	Activity (Bq/cm ³)	Half Life	Decay Mode	Decay Product
²⁷ Mg	6.2x10 ³	9.4 min	β^-	²⁷ Al
²⁷ Si	3.0x10 ⁵	4.2 s	β^+	²⁷ Al
²⁶ Al	5.6x10 ⁻⁵	7.2x10 ⁻⁵ y	β^+	²⁶ Mg
²⁵ Al	5.7x10 ³	7.2 s	β^+	²⁵ Mg
²³ Mg	5.9x10 ³	11.3 s	β^+	²³ Na
¹⁵ O	1.6x10 ⁵	2.0 min	β^+	¹⁵ N
¹³ N	1.2x10 ⁵	10.0 min	β^+	¹³ C
³ H	4.0x10 ⁻²	12.3 y	β^-	³ He

4.2.2 Cooling Time Studies for Activated Elements of METU-DBL

While care was taken to minimize radioactivation in the choice of materials used in METU-DBL, it is impossible to completely avoid it due to the nature of irradiating materials with 15-30 MeV protons. A certain amount of waiting time is necessary to reduce the dose in the room before a worker can be allowed in. Therefore, cooling times necessary for activated elements of METU-DBL were studied using FLUKA. A detector was modeled in order to calculate the radiation dose around the first protective collimator. The ICRU (International Commission on Radiation Units & Measurements) sphere [111] model has been standardized to model such a detector. This sphere has the same composition as human tissue. The properties of the ICRU sphere are;

- 15 cm radii
- Human tissue properties
 - Density: 1 g/cm³
 - Mass percentages
 - * 76.2 % Oxygen
 - * 11.1 % Carbon
 - * 10.1 % Hydrogen
 - * 2.6 % Nitrogen

4.2.2.1 Cooling Time For the First Protective Collimator

In FLUKA, an ICRU sphere representing the detector was placed next to the first protective collimator and the cooling time around the collimator was examined. In Figure 4.20, the place of the ICRU sphere is seen. It is 1 cm away from the SS316 first protective collimator. This study was conducted for the pretest design of the METU-DBL so, the material of the first protective collimator was SS316 in the pretests. In Table 4.21, cooling time and respective dose rates 1 cm away from the first protective collimator after a 1 hour irradiation with 0.1 μ A are seen. The results of the simulation show that the dose 1 cm away from the first protective collimator drops to safe levels

for radiation workers after 4 days. During the pretests, the cooling time of the first protective collimator was different from the results obtained in FLUKA. The reason for this is the repetitive irradiations at different currents and with different exposures during the pretests of METU-DBL. The results obtained from the FLUKA simulation program are the cooling times obtained after a single irradiation for 1 hour at $0.1 \mu\text{A}$ current. In the pretests, the cooling time of the collimator was higher than expected because of these serial irradiations. A list of all irradiations performed during the commissioning and the pretests of METU-DBL are listed in Table 4.22. After the last irradiation, the dose rate 1 cm away from the SS316 first protective collimator was $80 \mu\text{Sv/h}$ two days after irradiation. Given the detailed radioprotection study performed in Section 4.2.1, the cooling of the first protective collimator will be accelerated for the fixed setup with respect to the pretests.

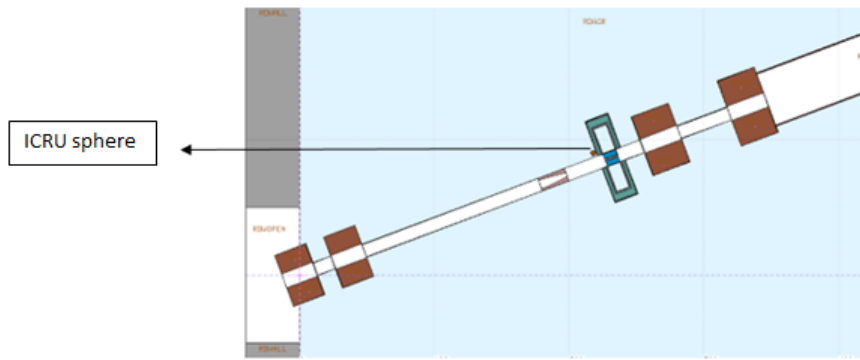


Figure 4.20: The place of ICRU sphere in FLUKA. Sphere is 1 cm away from the first protective collimator.

Table 4.21: Cooling time and respective dose rates 1 cm away from the first protective collimator after a 1 hour irradiation with $0.1 \mu\text{A}$ are seen.

Time	Dose Rate ($\mu\text{Sv/h}$)	Time	Dose Rate ($\mu\text{Sv/h}$)
Beam is on	6.5×10^6	After 1 day	3.0×10^1
After 1 second	6.6×10^4	After 2 days	9.3
After 5 minutes	8.4×10^2	After 3 days	4.2
After 4 hours	2.0×10^2	After 4 days	2.8

Table 4.22: List of all irradiations performed at METU-DBL during the commissioning and the pretests of METU-DBL are listed.

Time (min)	Current (μA)	Date
21	0.1	24.10.2017
23	0.1	24.10.2017
18	0.1	27.10.2017
13	0.1	03.11.2017
36	0.1	21.11.2017
60	0.1	24.11.2017
58	0.1	29.11.2017
60	0.1	01.12.2017
60	0.1	11.12.2017
102	0.1	21.12.2017
30	1	21.12.2017
60	0.1	08.01.2018
60	0.1	12.01.2018
120	0.1	22.01.2018
60	0.1	26.01.2018
30	0.1	19.02.2018
60	0.1	21.02.2018
30	0.1	21.02.2018

4.2.2.2 Dose in the TAEA PHT R&D room

For scenarios to be used extensively in METU-DBL, the dose in the R&D Room according to Scenario A, B, C, D states is simulated separately for each scenario using flux, current and test times determined by TURTLE simulation program. At the TAEA PAF, the workers can only enter the room according to the values read by the detectors in the R&D room and the door opens when the dose rate of the detectors is below $25.0 \mu\text{Sv/h}$. However, when the radiation workers enter the room when the dose rate fall below $2.5 \mu\text{Sv/h}$. In the FLUKA, the ICRU sphere was placed where the detectors were located and the doses were taken. The location of the ICRU sphere used for the studies in the R&D room is shown in Figure 4.21. According to the

ICRU sphere located in the R&D room, the prompt doses in the room and durations of the dose rate drop below $2.5 \mu\text{Sv/h}$ are shown in Table. The dose rate in the room fall below $2.5 \mu\text{Sv/h}$ after 1 second for Scenario A and Scenario B, after 16 hours for Scenario C, and after 2 days for Scenario D.

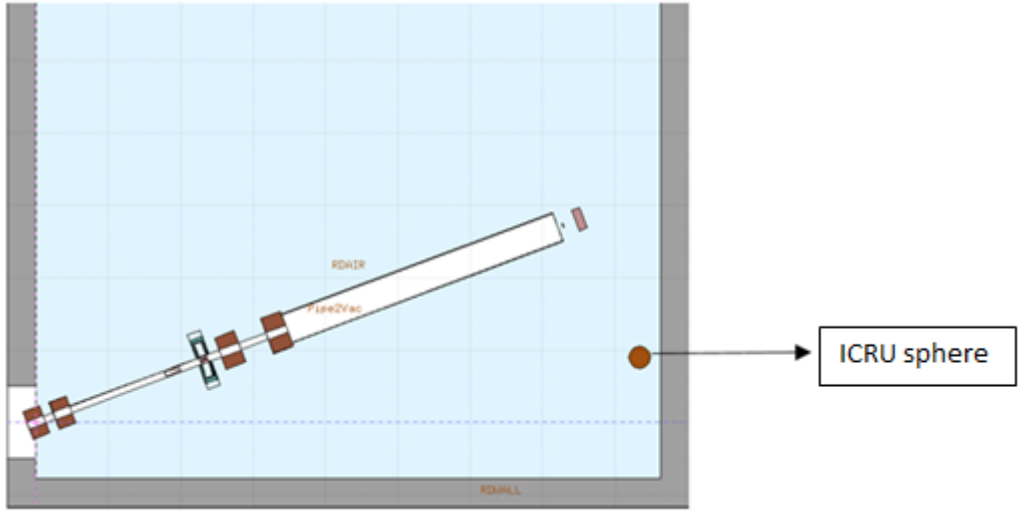


Figure 4.21: The location of an ICRU sphere in FLUKA. The pretest setup of the METU-DBL is seen. Brown sphere is representing the ICRU sphere and prompt dose studies for the room were performed according to this sphere.

Table 4.23: Time that dose rate drops below $2.5 \mu\text{SV/h}$ in the room when the beam is on according to Scenario A-B-C-D.

Scenarios in METU-DBL	Dose rates when beam is on ($\mu\text{Sv/h}$)	Time after which dose rates drop below $2.5 \mu\text{Sv/h}$ in the room
Scenario A	4.6×10^4	1 second
Scenario B	2.2×10^5	1 second
Scenario C	6.9×10^4	16 hours
Scenario D	9.7×10^6	2 days

4.2.2.3 Cooling Time Studies for the Beam Dump

The cooling time for the beam dump, which is located at the end of METU-DBL and is responsible for stopping the beam, has been studied. The calculation is performed for an irradiation of 1 hour at 0.1 μA current. The material of the dump is Al6082 and it has a 2 mm thick graphite film on the front surface. An ICRU sphere was placed 1 cm away from the surface of the dump and activation calculations were carried out. Table 4.24 shows the waiting period and dose rates on the ICRU sphere up to 4 days after the irradiation.

Table 4.24: Cooling time after an irradiation of 1 hour at 0.1 μA for the beam dump. Cooling times and received dose rates are given.

Time	Dose Rate ($\mu\text{Sv/h}$)
During irradiation	2.3×10^6
1 second after irradiation	3.0×10^4
5 minutes after irradiation	2.7×10^3
4 hours after irradiation	1.1×10^1
8 hours after irradiation	7.7
1 day after irradiation	3.8
2 days after irradiation	1.4
3 days after irradiation	6.2×10^{-1}
4 days after irradiation	3.6×10^{-1}

The dose rate of the beam dump lowers to approximately 2.5 $\mu\text{Sv/h}$ two days after the irradiation. In addition, only a few radioisotopes remain on the graphite surface 1 second after the irradiation and are shown in Table 4.25. The resulting radioisotopes are also short-lived.

Table 4.25: Radioisotopes that remain on the graphite surface 1 second after one hour irradiation. The resulting two isotopes are listed.

Isotope	Decay Mode	Half Life	Decay Product
^{11}C	β^+	20.3 min	^{11}B
^{10}C	β^+	19.2 s	^{10}B

In this section, the radioprotection studies discussed. Firstly, candidate materials for the first protective collimator were given and analyses were conducted for each material to choose the suitable material for the collimator. As a result, Al6082 was selected due to its low activity and also machinability. Secondly, sapphire and borosilicate were studied for the window of movable beam screen. Sapphire has lower activity than borosilicate so, sapphire was chosen as a material of the window of movable beam screen. Lastly, cooling time studies for activated elements of METU-DBL and their results discussed.

CHAPTER 5

CONCLUSION

Under radiation, crystalline materials can develop vacancy and interstitial defects while free volumes and anti-free volumes, which are vacancy-like and interstitial-like defects respectively, can be generated in amorphous materials. These materials do not have crystal defects like dislocation and their strength is higher than their crystalline counterparts. Therefore, they can be used in high radiation environments as an alternative to crystal materials.

In this thesis, radiation effects of proton radiation on BMG samples, cast specifically for this study, and commercially available SS were examined. The test environment of 30 MeV protons was provided by METU-DBL at TAEA. Radiation protection of METU-DBL, important to reduce secondary dose received by samples, was also performed as a part of this thesis study.

Numerous characterization techniques were used to analyze non-irradiated and irradiated samples and also SRIM simulation program was used for understanding energy deposition in materials and structural defects like vacancies. SRIM simulation provides the range of 30 MeV protons in SS and BMGs to be similar, 1.75 mm and 2 mm respectively. Vacancy formations close to the end of the proton's path in the material guides the interpretation of the analysis results. In SEM analyses, no surface damages such as blistering, cracking, delamination, exfoliation were observed in any of the samples. XRD analyses did not indicate any new phase formation. However, some change in the intensity of the XRD peaks of samples were observed after the irradiation, possibly due to structural defects that occur during irradiation. DSC anal-

ysis revealed small changes in the phase transformation temperatures. New vacancies in the irradiated samples might have induced these differences. Moreover, no visible change was observed in the microhardness test results. Finally, VSM analysis was carried out only for $\text{Fe}_{36}\text{Co}_{36}\text{B}_{19.2}\text{Si}_{4.8}\text{Nb}_4$ samples because this is the only material which has a soft magnetic property. The coercivity increased due to structural defects while the saturation magnetization did not change significantly.

In conclusion, small structural defects were observed in all samples under radiation. This test campaign was the first displacement damage test performed in Turkey, and demonstrated the effect of proton irradiation on metallic and metallic glass samples.

REFERENCES

- [1] “IMECE Satellite,” <http://uzay.tubitak.gov.tr/en/projeler/imece>, last access on 21.01.2019.
- [2] “Tubitak Space Technologies Research Institute,” <http://uzay.tubitak.gov.tr/en>, last access on 29.01.2019.
- [3] M. M. Trexler and N. N. Thadhani, “Mechanical Properties of Bulk Metallic Glasses,” *Progress in Materials Science*, vol. 55, no. 8, pp. 759–839, 2010.
- [4] Wikipedia contributors, “List of orbits — Wikipedia, the free encyclopedia,” 2018, [Online; accessed 18-November-2018]. [Online]. Available: https://en.wikipedia.org/w/index.php?title=List_of_orbits&oldid=859610703
- [5] “Geostationary Satellite,” <http://www.sciencedirect.com/topics/earth-and-planetary-sciences/geostationary-satellite>, last access on 30.01.2019.
- [6] M. P. Petkov, “The Effects of Space Environments on Electronic Components,” *NASA Technical Report*, pp. 1–36, 2003.
- [7] M. M. Rahman, D. Shankar, and S. Santra, “Analysis of Radiation Environment and Its Effect on Spacecraft in Different Orbits.” *Proceedings of the International Astronautical Congress, IAC*, vol. 12, pp.1–7, 2017
- [8] S. Bourdarie and M. Xapsos, “The Near-earth Space Radiation Environment,” *IEEE transactions on nuclear science*, vol. 55, no. 4, pp. 1810–1832, 2008.
- [9] E. Grossman and I. Gouzman, “Space Environment Effects on Polymers in Low Earth Orbit,” *Nucl. Instr. Meth. Phys. Res. B: Beam Interactions with Materials and Atoms*, vol. 208, pp. 48–57, 2003.
- [10] “Medium Earth Orbit,” <https://earthobservatory.nasa.gov/features/OrbitsCatalog>, last access on 28.03.2019.

- [11] M. Xapsos, “New Approach to Total Dose Specification for Spacecraft Electronics,” *Proceedings of the 2017 Applied Space Environment Conference (ASEC)*, pp. 1–7, 2017.
- [12] L. Maria Martinez, “Analysis of LEO Radiation Environment and Its Effects on Spacecraft’s Critical Electronic Devices,” Master’s thesis, Embry-Riddle Aeronautical University, December 2011.
- [13] E. Stassinopoulos and K. LaBel, “The Near-earth Space Radiation Environment for Electronics,” *IEEE Transactions on Nuclear Science*, vol. 55, pp. 1810–1832, 2008.
- [14] R. B. Horne, et al., “Wave Acceleration of Electrons in the Van Allen Radiation Belts,” *Nature*, vol. 437, no. 7056, p. 227, 2005.
- [15] “Earth Radii,” <http://sci.esa.int/cluster/52831-earth-plasmasphere-and-the-van-allen-belts/>, last access on 19.03.2019.
- [16] “Van Allen Belts,” <http://www.fp7-spacecast.eu/>, last access on 20.03.2019.
- [17] S. Deme, “Space Radiation Dosimetry,” 2003.
- [18] V. Ptuskin, V. Zirakashvili, and E.-S. Seo, “Spectrum of Galactic Cosmic Rays Accelerated in Supernova Remnants,” *The Astrophysical Journal*, vol. 718, no. 1, p. 31, 2010.
- [19] A. Holmes-Siedle and L. Adams, “Handbook of Radiation Effects,” *Oxford Press*, pp. 388, 1993.
- [20] L. W. Townsend, “Implications of the Space Radiation Environment for Human Exploration in Deep Space,” *Radiation protection dosimetry*, vol. 115, no. 1-4, pp. 44–50, 2005.
- [21] “NASA Captures Image of M1 Coronal Mass Ejection,” <http://scitechdaily.com/nasa-captures-image-of-m1-coronal-mass-ejection/>, last access on 01.02.2019.
- [22] “Radiation,” <http://scienceworld.wolfram.com/physics/Radiation.html>, last access on 01.02.2019.

- [23] K.-H. Ng, “Non-Ionizing Radiations—Sources, Biological Effects, Emissions and Exposures,” in *Proceedings of the International Conference on Non-Ionizing Radiation at UNITEN*, pp.1–16, 2003.
- [24] D. Vesley, “Ionizing and Nonionizing Radiation,” in *Human Health and the Environment*. Springer, 1999, pp. 65–74.
- [25] “Non-Ionizing Radiation,” https://en.wikipedia.org/wiki/Non-ionizing_radiation, last access on 24.05.2019.
- [26] B. Brennan and R. Lyons, “Ranges of Alpha Particles in Various Media,” *Ancient TL*, vol. 7, no. 2, pp. 32–37, 1989.
- [27] “Electron Scattering,” <http://www.ioffe.ru/ES/>, last access on 29.04.2019.
- [28] D. R. McAlister, “Gamma Ray Attenuation Properties of Common Shielding Materials,” *PG Research Foundation, University Lane Lisle, IL*, vol. 60532, 2012.
- [29] N. M. Zali, et al., “Neutron Shielding Behavior of Thermoplastic Natural Rubber/Boron Carbide Composites,” in *IOP Conference Series: Materials Science and Engineering*, vol. 298, no. 1. IOP Publishing, 2018, p. 012018.
- [30] “Radiotherapy and Bragg’s peak,” <https://www.samhs.org.au/Virtuallast> access on 14.04.2019.
- [31] W. Leo “Techniques for Nuclear and Particle Physics Experiments: A How-To Approach,” *Springer Science & Business Media*, pp. 24–25, 2012.
- [32] “Detector Physics,” <https://indico.mitp.uni-mainz.de/event/65/attachments/1698/1781/Kuehn.pdf>, last access on 09.05.2019.
- [33] S. Samwel, et al., “Studying the Total Ionizing Dose and Displacement Damage Dose Effects for Various Orbital Trajectories,” *First Middle East-Africa Regional IAU Meeting*. Citeseer, 2008, p. 12.
- [34] K. E. Holbert, “Radiation Effects Damage,” *Course EEE 598 Syllabus*,, 2012.
- [35] J. Srour, C. Marshall, and P. Marshall, “Review of Displacement Damage Effects in Silicon Devices,” *IEEE Transactions on Nuclear Science*, vol. 50, no. 3, pp. 653–670, 2003.

- [36] M. Boscherini, et al., “Radiation Damage of Electronic Components in Space Environment,” *Nucl. Instr. Meth. Phys. Res. A: Accelerators, Spectrometers, Detectors and Associated Equipment*, vol. 514, no. 1-3, pp. 112–116, 2003.
- [37] J. M. Maclaren and T. Majni, “Hard/Soft Error Detection,” Mar. 23 2004, *US Patent* 6,711,703.
- [38] “Linear Energy Transfer,” https://en.wikipedia.org/wiki/Linear_energy_transfer, last access on 24.05.2019.
- [39] E. Petersen, *Single Event Effects in Aerospace*. IEEE Press, 2011.
- [40] R. Gaillard, “Single Event Effects: Mechanisms and Classification,” *Soft Errors in Modern Electronic Systems*. Springer, 2011, pp. 27–54.
- [41] “Proton Hızlandırıcı Tesisi,” <http://kurumsalarsiv.taek.gov.tr/bitstream/1/612/1/10561.pdf>, last access on 07.05.2019.
- [42] “Nuclear Medicine,” <https://www.monrol.com.tr/en/62/page/nuclear-medicinpet>, last access on 07.05.2019.
- [43] TAEA SANAEM, “Proton Accelerator Facility Booklet,” 2012.
- [44] ECSS, “Single Event Effects Test Method and Guidelines - ESCC Basic Specification No . 25100,” *ECSS*, no. 25100, pp. 1–24, 2002.
- [45] “Beam Stopper,” <http://www.vatvalve.com/de/business/valves/product?id=79040-CE44>, last access on 09.05.2019.
- [46] “Insertable Gate Valve,” <http://www.vatvalve.com/business/valves/product?id=08140-FA44>, last access on 09.05.2019.
- [47] M. Yigitoglu, “Radiation Environment Predictions for the Imece Satellite and G4Beamline Simulations for the METU-DBL Project,” Master’s thesis, Middle East Technical University, February 2017.
- [48] M. Demirköz, et al., “Pretest Setup Installation of the METU-DBL Project to Perform Space Radiation Tests,” *2017 8th International Conference on Recent Advances in Space Technologies (RAST)*, pp. 311–316, 2017.
- [49] “Sonmez Trafo,” <http://www.sonmeztrafo.com.tr/>, last access on 21.05.2019.

- [50] A. Avaroglu, et al., “The First SEE Test Campaign in Turkey at the METU Defocusing Beamline Preliminary Setup,” no. December, pp. 1–4, 2017.
- [51] C. Saral, personal communication.
- [52] A. Avaroglu, personal communication.
- [53] “Fluka,” <http://www.fluka.org/fluka.php>, last access on 12.04.2019.
- [54] M. B. Demirköz, et al., “Installation of the METU-DBL Defocusing BeamLine to Perform Space Radiation Tests” (In press).
- [55] B. Demirköz, et al., “METU Defocusing BeamLine Project for the First SEE Tests in Turkey and the Test Results From the METU-DBL Preliminary Setup,” *Nucl Instr. Meth. Phys. Res. A: Accelerators, Spectrometers, Detectors and Associated Equipment*, pp.10–12, 2018.
- [56] M. M. Khan, et al., “Recent Advancements in Bulk Metallic Glasses and Their Applications: A review,” *Critical Reviews in Solid State and Materials Sciences*, vol. 43, no. 3, pp. 233–268, 2018.
- [57] J. Igel, et al., “A Practical Investigation of the Production of Zr-Cu-Al-Ni Bulk Metallic Glasses by Arc Melting and Suction Casting,” *Materials Transactions*, vol. 56, no. 11, pp. 1834–1841, 2015.
- [58] “Crystalline and Amorphous Solids,” <https://www.toppr.com/guides/chemistry/the-solid-state/crystalline-and-amorphous-solids/>, last access on 09.04.2019.
- [59] M. Telford, “The Case for Bulk Metallic Glass,” *Materials today*, vol. 7, no. 3, pp. 36–43, 2004.
- [60] W. Jiang, et al. “Comparison of Mechanical Behavior Between Bulk and Ribbon Cu-based Metallic Glasses,” *Materials Science and Engineering: A*, vol. 430, no. 1-2, pp. 350–354, 2006.
- [61] R. Nowosielski, A. Januszka, and R. Babilas, “Thermal Properties of Fe-based Bulk Metallic Glasses,” *Journal of Achievements in Materials and Manufacturing Engineering*, vol. 55, no. 2, pp. 349–354, 2012.

- [62] X. Du, et al., “New Criterion of Glass Forming Ability for Bulk Metallic Glasses,” *Journal of Applied Physics*, vol. 101, no. 8, pp. 99–102, 2007.
- [63] A. Salimon, et al., “Bulk Metallic Glasses: What Are They Good for?” *Materials Science and Engineering: A*, vol. 375, pp. 385–388, 2004.
- [64] A. Inoue, “Stabilization of Metallic Supercooled Liquid and Bulk Amorphous Alloys,” *Acta materialia*, vol. 48, no. 1, pp. 279–306, 2000.
- [65] T. Zhang, et al., “Fe-based Ferromagnetic Glassy Alloys with Wide Supercooled Liquid Region,” *The Japan Institute of Metals*, vol. 36, no. 9, pp. 1180–1183, 1995.
- [66] J. Hye-in and C.-Y. Haein, “Analysis of the Structural, Thermal, and Magnetic Properties in the Bulk Metallic Glass Alloy $\text{Co}_{36}\text{Fe}_{36}\text{B}_{19.2}\text{Si}_{4.8}\text{Nb}_4$ system,” *Journal of Korean Physical Society*, vol. 58, p. 116, 2011.
- [67] A. Inoue, “Bulk Amorphous Alloys with Soft and Hard Magnetic Properties,” *Materials Science and Engineering: A*, vol. 226, pp. 357–363, 1997.
- [68] T. Zhang, et al., “Ductile Fe-based Bulk Metallic Glass with Good Soft-Magnetic Properties,” *Materials transactions*, vol. 48, no. 5, pp. 1157–1160, 2007.
- [69] A. Inoue and A. Takeuchi, “Recent Development and Application Products of Bulk Glassy Alloys,” *Acta Materialia*, vol. 59, no. 6, pp. 2243–2267, 2011.
- [70] D. B. Miracle, et al., “Structural Aspects of Metallic Glasses,” *Mrs Bulletin*, vol. 32, no. 8, pp. 629–634, 2007.
- [71] J. Carter, et al., “Effects of Cu ion irradiation in $\text{Cu}_{50}\text{Zr}_{45}\text{Ti}_5$ metallic glass,” *Scripta Materialia*, vol. 61, no. 3, pp. 265–268, 2009.
- [72] T. Nagase and Y. Umakoshi, “Temperature Dependence in Density-Fluctuation-Induced Crystallization in Metallic Glass by MeV Electron Irradiation,” *Intermetallics*, vol. 18, no. 10, pp. 1803–1808, 2010.
- [73] H. Zhang, et al., “ H^+ -induced Irradiation Damage Resistance in Fe-and Ni-based Metallic Glass,” *Nucl. Instr. Meth. Phys. Res. B: Beam Interactions with Materials and Atoms*, vol. 375, pp. 79–86, 2016.

- [74] Z. Wang, *Transmission Electron Microscopy of Shape-Controlled Nanocrystals and Their Assemblies*. ACS Publications, 2000.
- [75] L. Reimer, *Scanning Electron Microscopy: Physics of Image Formation and Microanalysis*. Springer, 2013, vol. 45.
- [76] S. Rekha and V. B. Raja, “Review on Microstructure Analysis of Metals and Alloys Using Image Analysis Techniques,” in *IOP Conference Series: Materials Science and Engineering*, vol. 197, no. 1. IOP Publishing, 2017, p. 012010.
- [77] H. P. Klug and L. E. Alexander, “X-ray Diffraction Procedures: For Polycrystalline and Amorphous Materials,” *X-Ray Diffraction Procedures: For Polycrystalline and Amorphous Materials, 2nd Edition*, by Harold P. Klug, Leroy E. Alexander, pp. 992. ISBN 0-471-49369-4. Wiley-VCH, May 1974., p. 992, 1974.
- [78] M. Reading, “Modulated Differential Scanning Calorimetry—a New Way Forward in Materials Characterization,” *Trends Polym Sci*, vol. 1, no. 8, pp. 248–253, 1993.
- [79] S. Foner, “Vibrating Sample Magnetometer,” *Review of Scientific Instruments*, vol. 27, no. 7, pp. 548–548, 1956.
- [80] F. Fröhlich, P. Grau, and W. Grellmann, “Performance and Analysis of Recording Microhardness Tests,” *Physica status solidi (a)*, vol. 42, no. 1, pp. 79–89, 1977.
- [81] H. Zhang, et al., “Resistance to H⁺ Induced Irradiation Damage in Metallic Glass Fe₈₀Si_{7.43}B_{12.57},” *Journal of Nuclear Materials*, vol. 456, pp. 344–350, 2015.
- [82] W. Luo, B. Yang, and G. Chen, “Effect of Ar⁺ Ion Irradiation on the Microstructure and Properties of Zr–Cu–Fe–Al Bulk Metallic Glass,” *Scripta Materialia*, vol. 64, no. 7, pp. 625–628, 2011.
- [83] X. Zhang, et al., “Study of Irradiation Damage Induced by He⁺² Ion Irradiation in Ni₆₂Ta₃₈ Metallic Glass and W Metal,” *Nucl. Instr. Meth. Phys. Res. B Beam Interactions with Materials and Atoms*, vol. 406, pp. 548–554, 2017.

- [84] Z. Hu, et al., “Effect of Ion Irradiation on Mechanical Behaviors of $\text{Ti}_{40}\text{Zr}_{25}\text{Be}_{30}\text{Cr}_5$ Bulk Metallic Glass,” *Materials Research*, vol. 15, no. 5, pp. 713–717, 2012.
- [85] F. Tuomisto and I. Makkonen, “Defect Identification in Semiconductors with Positron Annihilation: Experiment and Theory,” *Reviews of Modern Physics*, vol. 85, no. 4, p. 1583, 2013.
- [86] K. Flores, et al., “Characterization of Free Volume in a Bulk Metallic Glass using Positron Annihilation Spectroscopy,” *Journal of materials research*, vol. 17, no. 5, pp. 1153–1161, 2002.
- [87] F. Hori, et al., “A Study of Defects In Electron-and Ion-Irradiated ZrCuAl Bulk Glassy Alloy Using Positron Annihilation Techniques,” *IOP Publishing*, vol. 262, no. 1, pp. 012025, 2011.
- [88] “Stainless Steel Family,” <http://www.worldstainless.org/Files/issf/non-image-files/PDF/TheStainlessSteelFamily.pdf>, last access on 06.04.2019.
- [89] D. E. Newbury* and N. W. Ritchie, “Is Scanning Electron Microscopy/Energy Dispersive X-ray Spectrometry (SEM/EDS) quantitative?” *Scanning*, vol. 35, no. 3, pp. 141–168, 2013.
- [90] “Positron Annihilation Lifetime Spectroscopy (pals),” <https://www.nist.gov/laboratories/tools-instruments/positron-annihilation-lifetime-spectrometer>, last access on 07.04.2019.
- [91] “Positron Annihilation Spectroscopy,” <https://www.picoquant.com/applications/category/metrology/positron-annihilation-lifetime-spectroscopy-pals>, last access on 06.04.2019.
- [92] “Positron Positronium Physics,” <http://fzk.fef.marmara.edu.tr/en/positron-positronium-physics/>, last access on 11.07.2019.
- [93] H. Jia, et al., “A study on the Surface Structures and Properties of Ni-free Zr-based Bulk Metallic Glasses After Ar and Ca Ion Implantation,” *Intermetallics*, vol. 41, pp. 35–43, 2013.

- [94] “Stainless Steel - grade 304,” <https://www.azom.com/article.aspx?ArticleID=965>, last access on 06.04.2019.
- [95] “Stainless Steel - grade 316,” <https://www.azom.com/article.aspx?ArticleID=863>, last access on 06.04.2019.
- [96] R. Machaka, “Ion Beam Modifications of Boron Nitride By Ion Implantation,” Master’s thesis, University of the Witwatersrand, 2006.
- [97] R. E. Stoller, et al., “On the use of SRIM for computing radiation damage exposure,” *Nuclear Energy and Technology*, vol. 310, no. 3, pp. 75–80, 2017.
- [98] A. Y. Konobeyev, et al., “Evaluation of Effective Threshold Displacement Energies and Other Data Required for the Calculation of Advanced Atomic Displacement Cross-Sections,” *Elsevier*, vol. 3, pp. 169–175, 2013.
- [99] “XRD Intensities,” <http://www.dxcicdd.com/01/pdf/D-033.pdf>, last access on 30.03.2019.
- [100] A. Mansouri Tehrani, et al., “Influencing the Martensitic Phase Transformation in NiTi Through Point Defects,” *Journal of Applied Physics*, vol. 118, no. 1, p. 014901, 2015.
- [101] W. D. Callister, D. G. Rethwisch *et al.*, *Materials Science and Engineering: An Introduction*. John Wiley & Sons New York, 2007, vol. 7.
- [102] G. G. Eichholz, “Radiation Protection and Radioactive Waste Management in the Operation of Nuclear Power Plants,” *Health Physics*, vol. 87, no. 6, p. 673, 2004.
- [103] “The Materials Used in Artificial Satellites and Space Structures,” <https://www.azom.com/article.aspx?ArticleID=12034>, last access on 08.05.2019.
- [104] “Aluminium Alloys - Aluminium 6082 Properties, Fabrication and Applications,” <https://www.azom.com/article.aspx?ArticleID=2813>, last access on 20.05.2019.
- [105] S. Uzun Duran, Personal Communication.

- [106] D. Forkel-Wirth, et al., “Radiation Protection at CERN,” *arXiv preprint arXiv:1303.6519*, 2013.
- [107] A. B. Poyrazoglu, Personal Communication.
- [108] U. Kilic, Personal Communication.
- [109] F. Tárkányi, et al., “Recommended Nuclear Data for Medical Radioisotope Production: Diagnostic Positron Emitters,” *Journal of Radioanalytical and Nuclear Chemistry*, vol. 319, pp. 533–666, 2019.
- [110] “Stopping Power and Range Tables for Protons,” https://physics.nist.gov/cgi_bin/Star/ptable.pl, last access on 28.05.2019.
- [111] E. Gargioni, L. Büermann Measurement of $H^*(10)$ and $H_p(10)$ in Mixed High-Energy Electron and Photon Fields. *Proc. 10th Int. Congress of The International Radiation Protection Association Hiroshima, Japan, 2000.*

APPENDIX A

A.1 SEM MICROGRAPHS

An example of penetration depth of 30 MeV protons inside the material is given for $\text{Fe}_{36}\text{Co}_{36}\text{B}_{19.2}\text{Si}_{4.8}\text{Nb}_4$ sample.

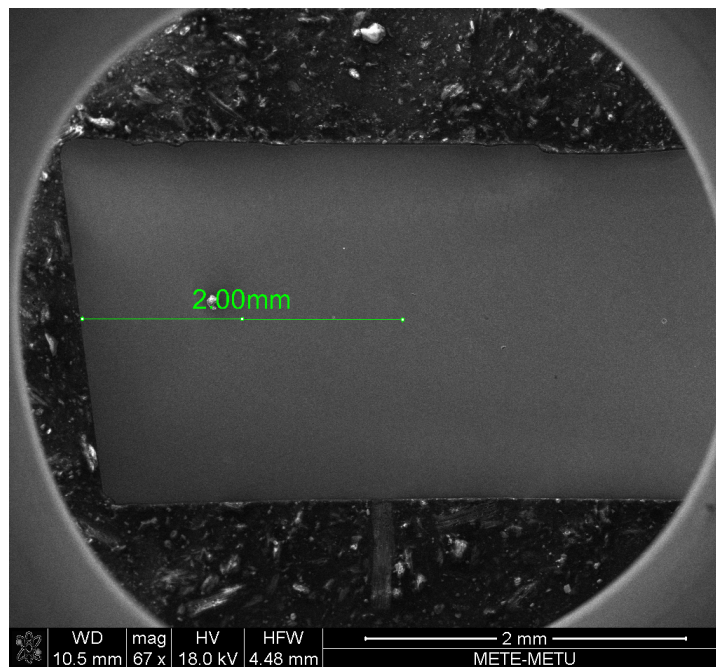


Figure A.1: Penetration depth of 30 MeV protons inside the $\text{Fe}_{36}\text{Co}_{36}\text{B}_{19.2}\text{Si}_{4.8}\text{Nb}_4$ sample. The penetration depth is roughly 2.00 mm.

A.2 LINE MAPPING

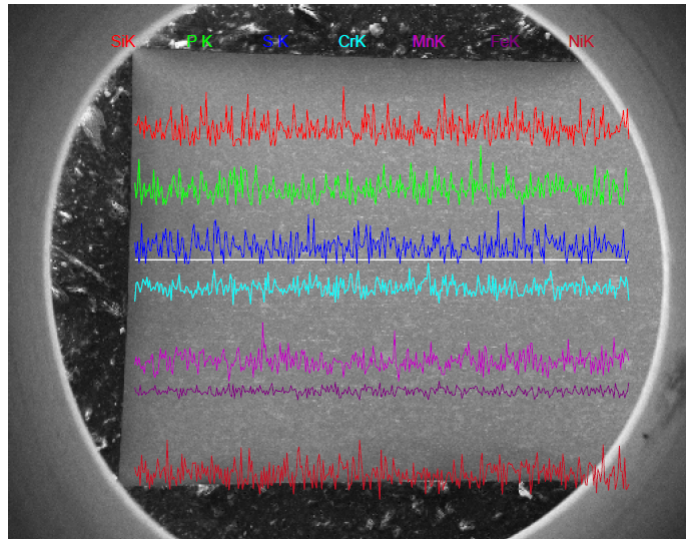


Figure A.2: Line mapping of horizontally embedded 304 SS sample. This sample received the highest fluence which is 1.0×10^{13} p/cm².

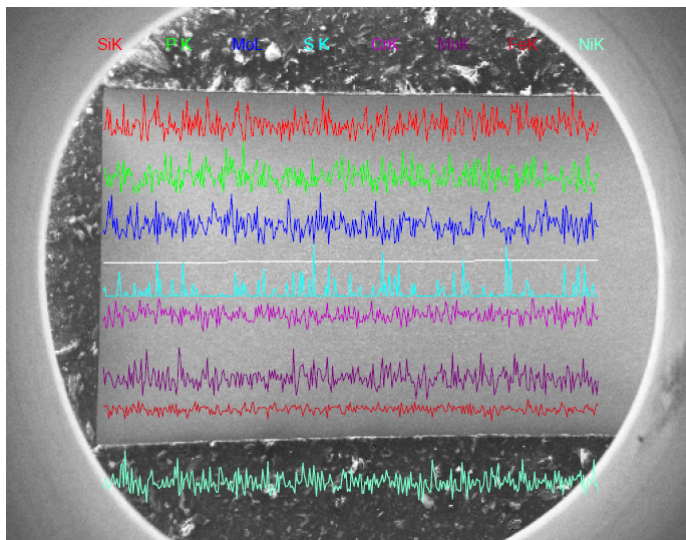


Figure A.3: Line mapping of horizontally embedded 316 SS sample. This sample received the highest fluence which is 1.0×10^{13} p/cm².

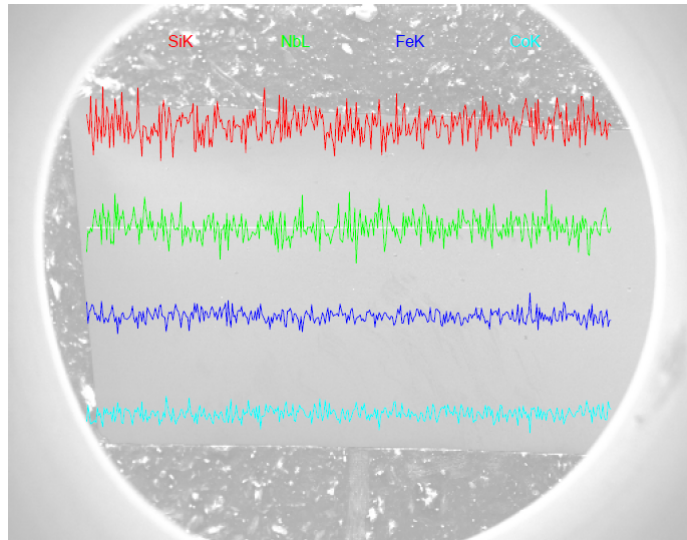


Figure A.4: Line mapping of horizontally embedded $\text{Fe}_{36}\text{Co}_{36}\text{B}_{19.2}\text{Si}_{4.8}\text{Nb}_4$ sample. This sample received the highest fluence which is 1.3×10^{13} p/cm².

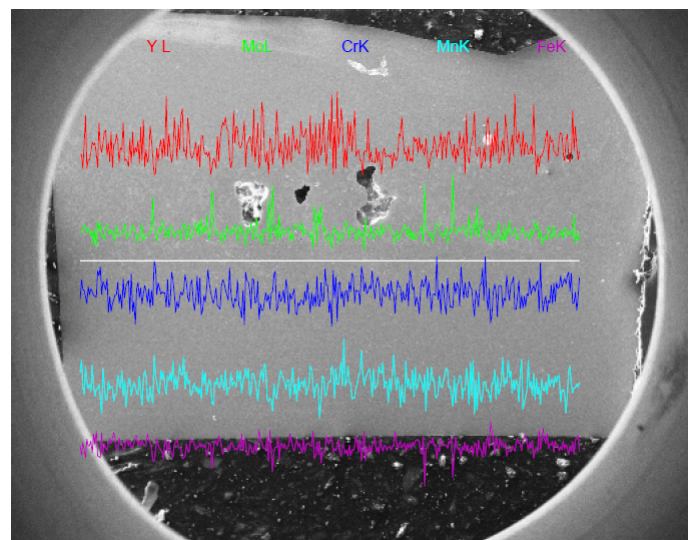


Figure A.5: Line mapping of horizontally embedded $\text{M}_{60}\text{Cr}_{13}\text{Mo}_{10}\text{B}_8\text{Y}_2\text{Mn}_7$ sample. This sample received the highest fluence which is 1.3×10^{13} p/cm².

A.3 EDS RESULTS

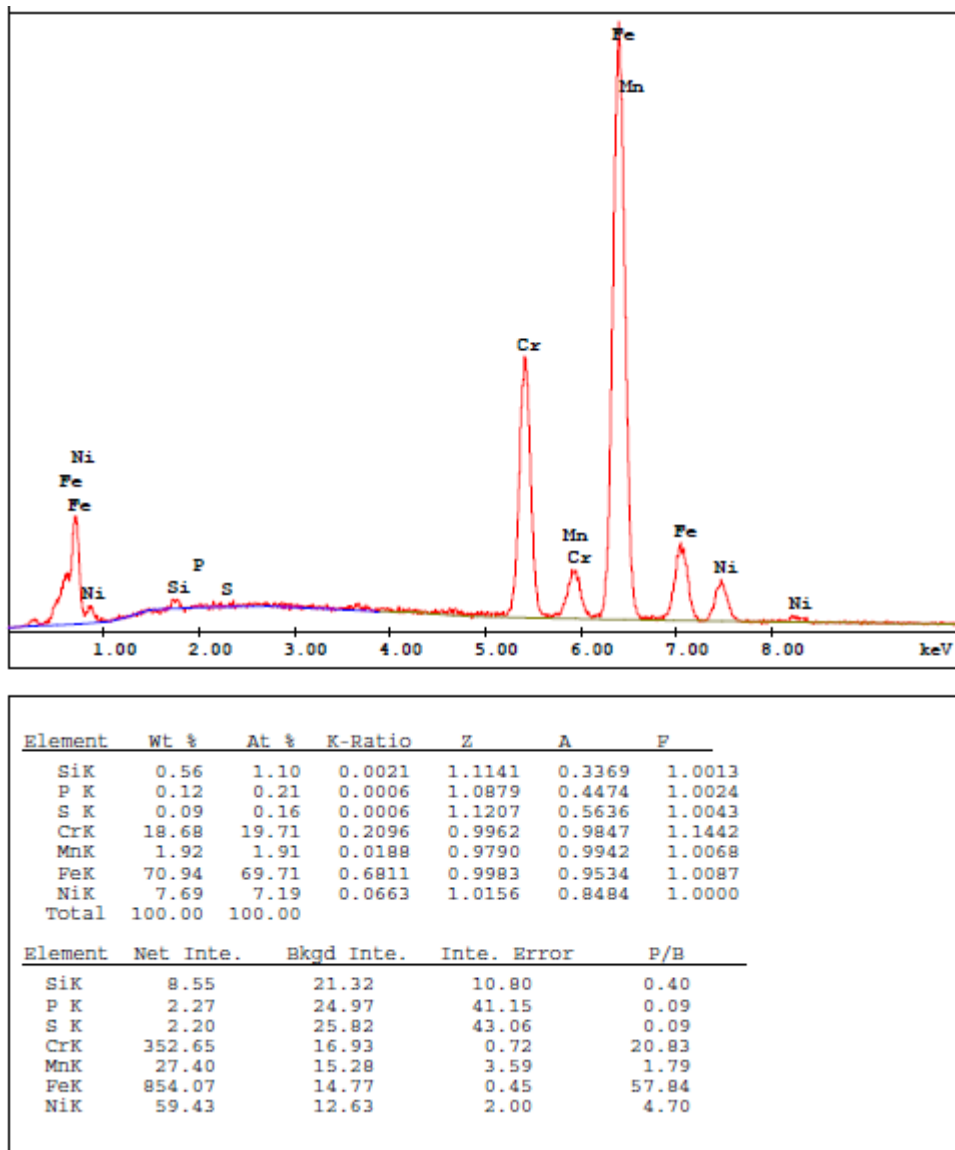
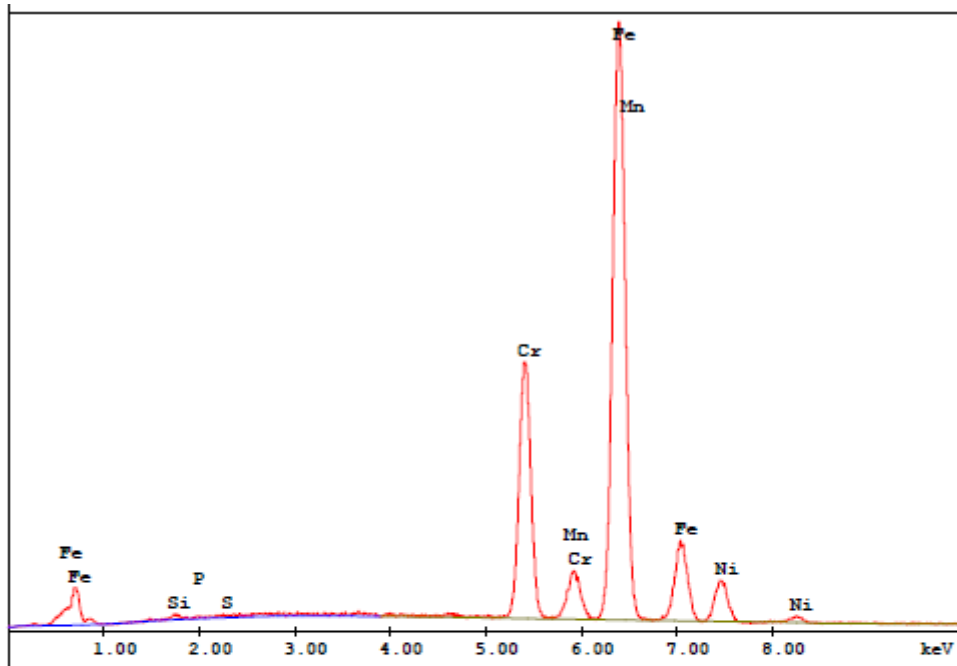


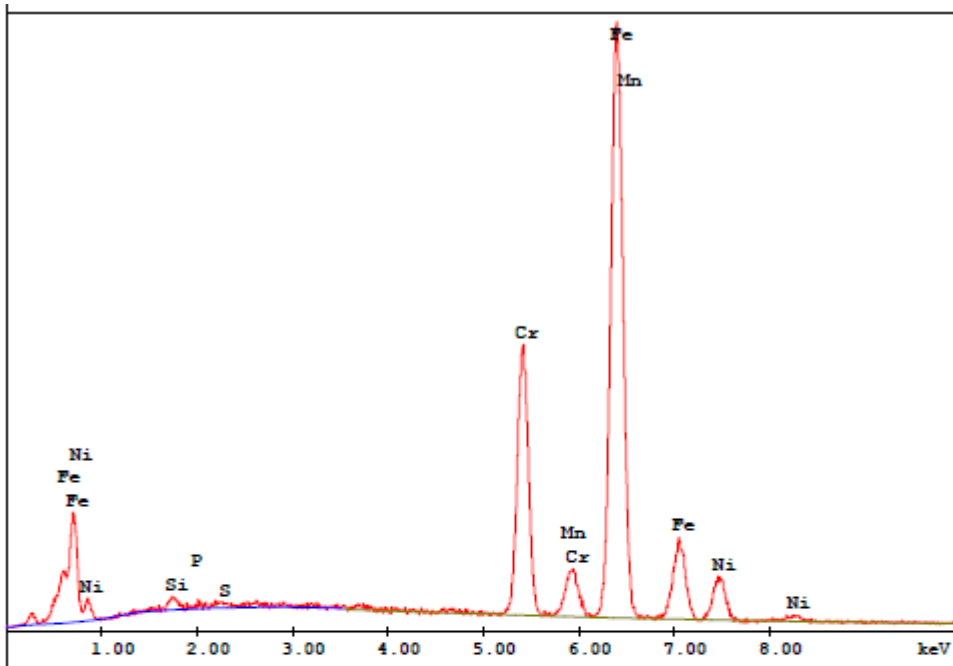
Figure A.6: EDS results of the highest fluence 304 SS sample from point 3 which is unirradiated part.



Element	Wt %	At %	K-Ratio	Z	A	F
SiK	0.61	1.19	0.0017	1.1024	0.2512	1.0023
P K	0.21	0.37	0.0008	1.0666	0.3387	1.0040
S K	0.20	0.33	0.0010	1.0948	0.4438	1.0070
CrK	18.62	19.62	0.2138	0.9942	0.9746	1.1849
MnK	1.98	1.98	0.0194	0.9780	0.9901	1.0089
FeK	70.67	69.32	0.6583	0.9985	0.9225	1.0113
NiK	7.71	7.19	0.0593	1.0188	0.7554	1.0000
Total	100.00	100.00				

Element	Net Inte.	Bkgd Inte.	Inte. Error	P/B
SiK	11.22	18.92	8.06	0.59
P K	4.97	24.38	19.05	0.20
S K	6.23	27.48	16.20	0.23
CrK	828.60	34.45	0.47	24.05
MnK	67.73	31.20	2.17	2.17
FeK	2063.05	30.10	0.29	68.54
NiK	146.50	25.70	1.24	5.70

Figure A.7: EDS results of the highest fluence 304 SS sample from point 1 which is irradiated part.



Element	Wt %	At %	K-Ratio	Z	A	F
SiK	0.69	1.35	0.0029	1.1135	0.3686	1.0014
P K	0.23	0.40	0.0012	1.0874	0.4826	1.0025
S K	0.19	0.32	0.0012	1.1201	0.5974	1.0044
CrK	18.77	19.76	0.2116	0.9957	0.9862	1.1481
MnK	1.79	1.79	0.0176	0.9785	0.9947	1.0075
FeK	70.12	68.73	0.6772	0.9978	0.9587	1.0096
NiK	8.21	7.65	0.0722	1.0151	0.8668	1.0000
Total	100.00	100.00				

Element	Net Inte.	Bkgd Inte.	Inte. Error	P/B
SiK	11.15	17.50	7.87	0.64
P K	4.43	20.80	19.76	0.21
S K	4.42	21.83	20.27	0.20
CrK	334.97	18.60	0.74	18.01
MnK	24.12	16.43	4.04	1.47
FeK	797.65	15.47	0.47	51.57
NiK	60.75	12.45	1.97	4.88

Figure A.8: EDS results of the highest fluence 304 SS sample from point 2 which is irradiated part.

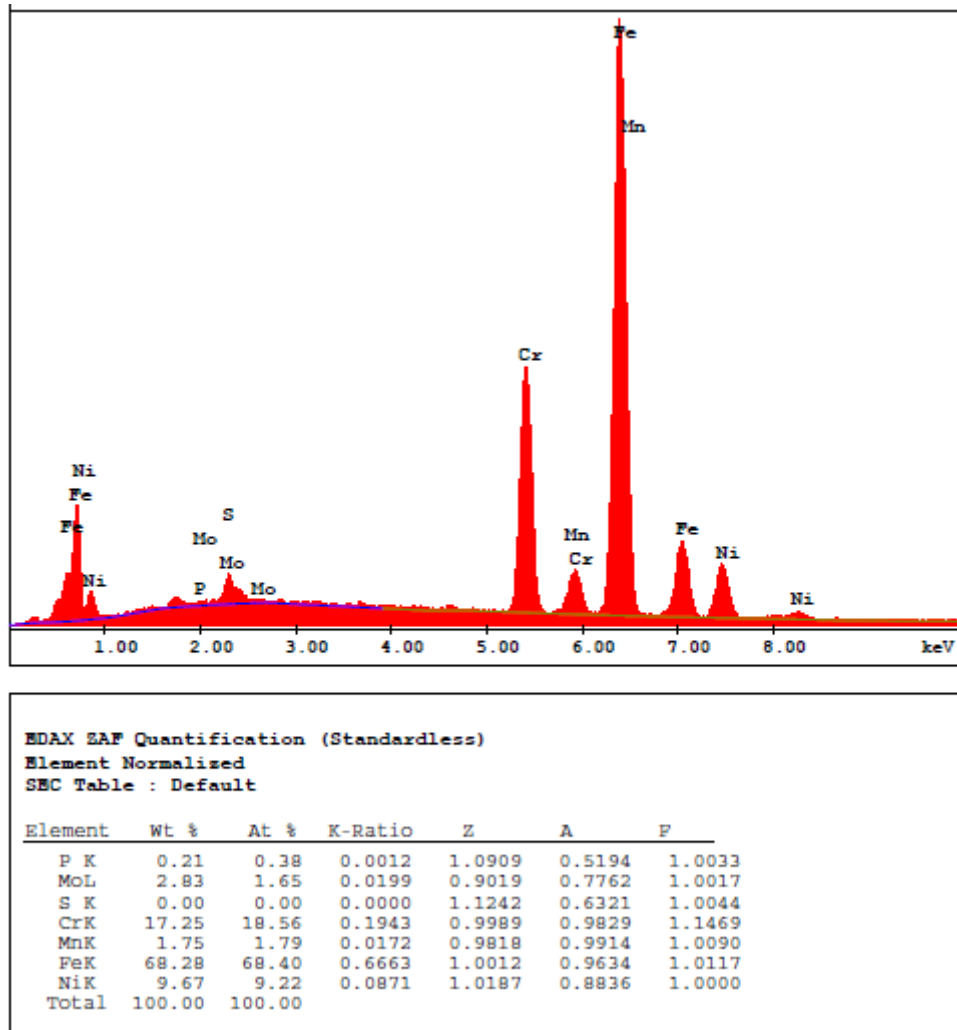


Figure A.9: EDS results of the highest fluence 316 SS sample from point 3 which is unirradiated part.

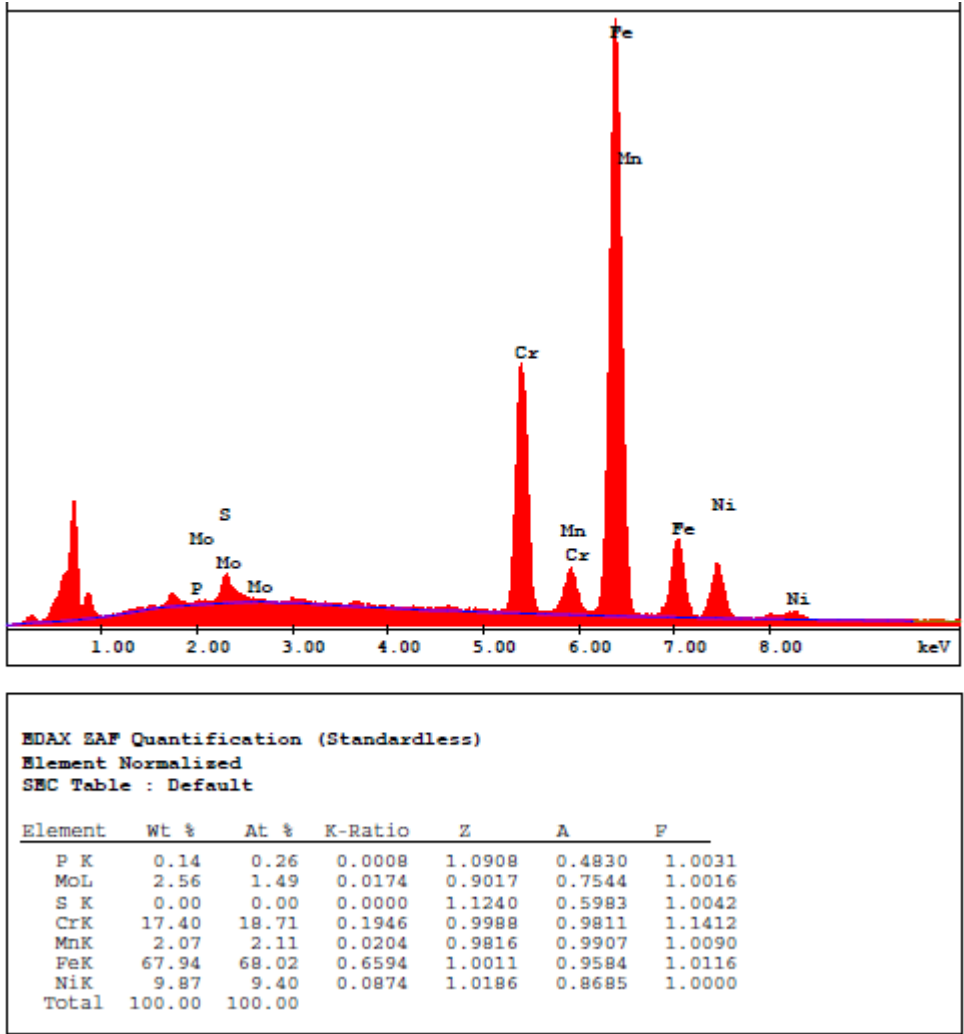
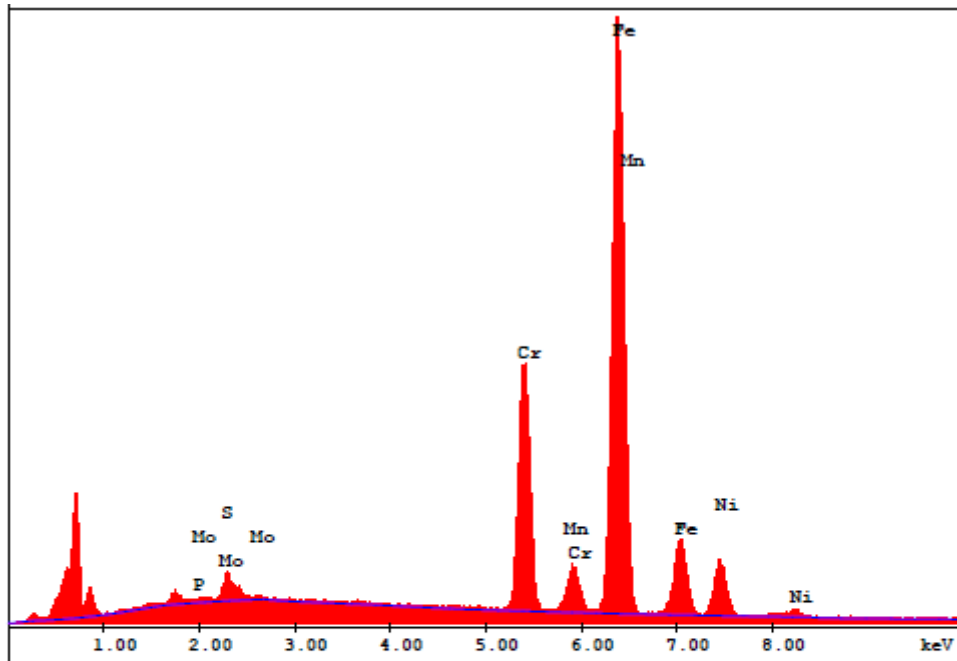


Figure A.10: EDS results of the highest fluence 316 SS sample from point 1 which is irradiated part.



EDAX EAF Quantification (Standardless)
 Element Normalized
 SEC Table : Default

Element	Wt %	At %	K-Ratio	Z	A	F
P K	0.21	0.38	0.0012	1.0910	0.5059	1.0033
MoL	2.93	1.71	0.0203	0.9020	0.7682	1.0017
S K	0.00	0.00	0.0000	1.1243	0.6196	1.0043
CrK	17.26	18.58	0.1936	0.9990	0.9819	1.1435
MnK	2.03	2.07	0.0199	0.9818	0.9908	1.0092
FeK	67.67	67.82	0.6592	1.0013	0.9614	1.0119
NiK	9.90	9.44	0.0886	1.0188	0.8785	1.0000
Total	100.00	100.00				

Figure A.11: EDS results of the highest fluence 316 SS sample from point 2 which is irradiated part.